BEAMFORMING USING QUASI OPTICAL APPROACH FOR 5G BACKHAUL.

by

PRATIK GHATE

Presented to the Faculty of the Graduate School of

The University of Texas at Arlington in Partial Fulfillment

of the Requirements

for the Degree of

DOCTOR OF PHILOSOPHY

THE UNIVERSITY OF TEXAS AT ARLINGTON

May 2021

This thesis is dedicated to my parents Mr. Bakul Ghate, Mrs. Shyamla Ghate and my brother Mr. Mohit Ghate who have helped and guided me at every moment in my life.

ACKNOWLEDGEMENTS

A lot of people have contributed to the success and completion of my dissertation, from whom I have learnt a lot of lessons which will be invaluable to me in my future pursuits.

I would like to start by thanking my supervising professor Dr. Jonathan Bredow for constantly motivating and encouraging me and for his invaluable advice during my doctoral studies. I would also like to thank him for giving me the opportunity to conduct this research work under him and for the financial assistance that he provided me with.

I am very thankful to Dr. Saibun Tjuatja, Dr. Kambiz Alavi, Dr. Weidong Zhou and Dr. Alan Davis for taking out time out of their busy schedules to serve on my Ph.D. defense committee.

I would also like to thank the faculty of the University of Texas at Arlington for all their guidance throughout my time in college. The knowledge I gained from classes with Dr. Frank Lewis, Dr. Saibun Tjuatja, and Dr. Michael Vasilyev, gave me the ability to accomplish the work I have performed here.

I would like to extend my appreciation to the staff in EE department that I worked with over the years – Todd Kelley, Cheryl Bailey and Gail Paniuski. They have always been there to guide help me when I needed.

I am thankful to all my friends in particular to Carlos Rodriguez, Akshay Malhotra, Satyen Awale, Alejandra Melendez, Ilse Mijares, Somya Paliwal, Nakul Karle, Kazi Shahid, Disha Sharad, Shrikant Ambade, Upasana Chaudhari, Neharika Raut, Raviraj Channappa, Vidhya Ramaraj, Chintan Mehta, Vatsal Salla, Omkar Murty, Shalaka Shinde, Afshin Shamshooli, Ajay Yadav and Vishal Raikwar. They all played a big role in my Ph.D. by encouraging and motivating me.

I am very lucky to have had such supportive family and friends who were always there for me and helped at every step of this program. Without the help of my parents and friends, I don't think it would have been possible.

-April 1, 2021

ABSTRACT

BEAMFORMING USING QUASI OPTICAL APPROACH FOR 5G BACKHAUL

Pratik Ghate, Ph.D.

The University of Texas at Arlington, 2021

Supervising Professor: Jonathan Bredow, Ph.D.

A new method is proposed for quasi optical beamforming that will enhance performance of emerging systems such as broad deployment of 5G backhaul communications, Internet of Things (IOT), vehicular networking systems, and unmanned aerial navigation systems. It is a promising approach at higher frequencies to reduce the size, cost and improve efficiency of the beamforming operation.

In this investigation candidate lens type structures are designed, studied, and analyzed using different configurations of dielectric wedges, plano-concave lens and dielectric slabs. These structures have cost, power consumption, size, weight, and bandwidth advantages, and are expected to be able to operate to higher frequencies than other beamformers in current use. The proposed structures give sufficient degrees of freedom to control the beamsteering by varying the dielectric constants and geometries of these structures and can form multiple minimally overlapping. This technique is valid for E and H principal planes.

Beamforming control with these and other electrically similar types of structures is expected to be achievable with vertical broadside coupled split ring resonators to control the beamsteering angles and beamwidth control. This approach gives sufficient degrees of freedom for steering the beam in

E and H principal planes by adjusting the placement of vertical broadside coupled split ring resonators and their arrays. This approach increases the gain of the radiating source resulting in highly directive beams with sufficient degrees of freedom to electronically tune beam properties.

Four different geometries are proposed, and performance is demonstrated for quasi- optical beamforming approach. These structures are designed for 1x3 patch antenna to demonstrate the formation of three minimally overlapping beams. Bandwidth enhancement and scanning angle of 180° has been achieved by using vertically oriented dielectric wedge. 6 dB gain enhancement and the capability to scale to somewhat larger arrays has also been demonstrated. Full wave simulations in Ansys HFSS are provided to support the proposed techniques of beamforming using quasi-optical (lens type) structures and validations are done in CST MWS.

TABLE OF CONTENTS

LIST OF FIGURES

LIST OF TABLES

LIST OF ABBREVIATIONS

AMC	Artificial Magnetic Conductor
NRI	Negative Refractive Index
MPA	Microstrip Patch Antenna
MM	Metamaterials
SRR	Split Ring Resonator
BC-SRR	Broadside Coupled Split Ring Resonator
DSRR	Double Sided Split Ring Resonator
EC-SRR	Edge Coupled Split Ring Resonator
ANT	Antenna
AoC	Antenna-on-Chip
CMOS	Complementary Metal-Oxide-Semiconductor
CPW	Co-planar Waveguide
EBG	Electromagnetic Bandgap
FCC	Federal Communications Commission
FDTD	Finite Difference Time Domain
FDFD	Finite Difference Frequency Domain
RCWA	Rigorous Coupled Wave Analysis
PWEM	Plane Wave Expansion Method
FEM	Finite Element Method
TMM	Transfer Matrix Method
PML	Perfectly Matched Layer
GND	Ground

HFSS	High Frequency Structure Simulator
HPC	High Performance Computing
IC	Integrated Circuit
IoE	Internet of Everything
IoT	Internet of Things
MIMO	Multiple Input Multiple Output
PAA	Phased Array Antenna
DUT	Device Under Test
PCB	Printed Circuit Board
PEC	Perfect Electric Boundary
PMC	Perfect Magnetic Boundary
VNA	Vector Network Analyzer
UWB	Ultra-Wide Band

CHAPTER 1

INTRODUCTION

Millimeter waves covers a large frequency spectrum from 30 GHz to 300 GHz. They are a portion of the spectrum between microwave frequencies (1 GHz to 30 GHz) and infrared (IR) wavelengths, which are also known as extremely high frequency (EHF). The wavelength (λ) of these waves lies in 1mm to 10mm range hence known as millimeter waves. Just a few decades ago these frequencies were essentially unused simply because very few electronic components could generate or receive millimeter waves. A lot of progress has been made since and so millimeter wave components and systems are now practical and affordable, and they're finding all sorts of new uses.

Current cellular networks (till 4G) face many challenges due to spectrum availability. Continuously increasing demands for mobile high internet speed and good connectivity bring these networks closer to their practical limits. 5G networks has been proposed as the solution to many of these drawbacks to ease the burden on the current infrastructure. This is possible by increasing the bandwidth (~24 GHz) so that a large spectrum will be available to a variety of uses. Increasing the bandwidth will ensure access to significantly high data rates, with mm-waves serving to provide suitable alternatives to provide the larger bandwidths and high data rates 5G demands. However, in the cellular phone structure operating with these mm-wave bands is far more complex because of high absorption and scattering losses.

Beamforming is a technique of forming single or multiple simultaneous beams that can be directed and shaped in the specified direction. Adaptive beamforming controls the directionality of the desired transmitted and received signals and mitigates their interference. Beamforming uses single or multiple antennas to control the directionality of transmission and reception of waves by carefully adjusting of phase and magnitude of antenna elements in a phased array array. By focusing a signal on a specific direction, beamforming reduces interference losses and delivers higher amplitude signals to a receiver

which in practice means faster information transfer.

1.1 Analog Beamforming

1.1.1 Blass Matrix

The Blass Matrix is a circuit type beamformer and it generates multiple minimally overlapping beams for antenna systems. It consists of several travelling wave feed lines connected to a linear antenna array through another set of element lines as shown in figure 1.1. These lines are interconnected by directional couplers at their crossover points, and they are terminated with matched load at each line end. A signal travelling from the input will travel along the feed line to the termination end. At each crossover, the signal gets coupled into other elements along line which excites the corresponding radiating element. The phase difference is caused at each input terminal because of the directional coupler and phase shift due to propagation delays between the antenna element resulting in beam steering. The amplitude distribution of the beam generated can be controlled by having different coupling coefficients form the directional couplers. A Blass Matrix design can get complicated with increasing numbers of elements and is a lossy network because of the resistive terminations, but it provides wide bandwidth performance.

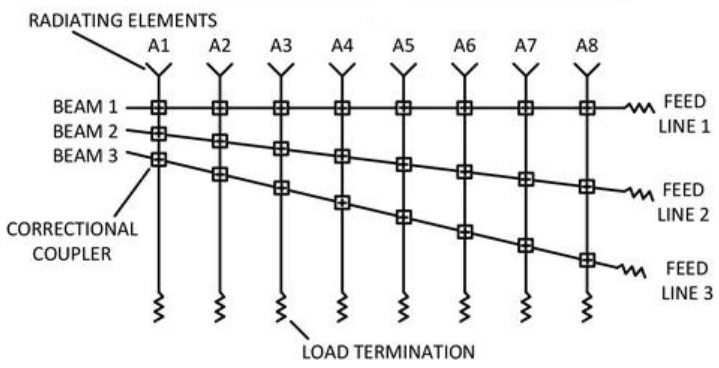

Figure 1.1 Blass Matrix [45]

1.1.2 Butler Matrix

The Butler matrix is another analog/ circuit type beamformer which was developed in the 1960's by Butler and Lowe [46]. The Butler Network is circuit type beamformer which produces minimally overlapping beams. It is a $M \times M$ structure which has M inputs and M outputs, for these networks, the number of inputs and outputs "M" are flexible. M must be an integer power of 2 (i.e., $M = 2^m$ where m is a positive integer) to form the network and for an $M \times M$ matrix, M possible beam directions can be formed. The Butler matrix consists of directional couplers, crossovers, phase shifters and antennas. A total of $(M/2)\log_2 M$ hybrid couplers and $(M/2)\log_2(M-1)$ fixed phase shifters are required to form the network. Figure. 1.2 shows a 2 X 2 butler matrix which will form 4 minimally overlapping beams. Analog beamformers are not ideal at mm-wave frequencies due to signals traveling through the circuit components like hybrid couplers, fixed phase shifters, and cross overs which causes insertion losses. Operation of a Butler matrix is narrow band as the phase shifts in the matrix are fixed (dependent of frequency).

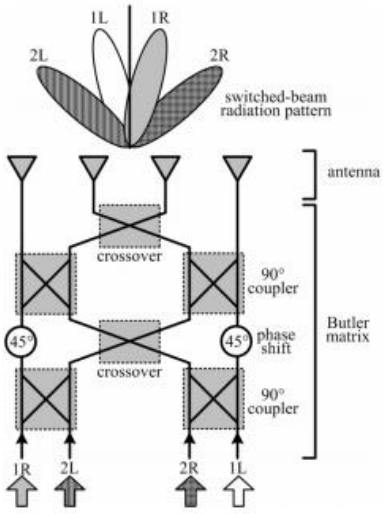

Figure 1.2 Butler Matrix [47]

1.2 Digital Beamforming

Digital beamforming is the most preferred beamforming approach as it makes the use of digital processors to control electronic components forming amplitude and phase for different channels of array elements. This allows for more complex beamforming than it is practical with Butler and Blass matrices and it facilitates adaptive beamforming. Digital beamformers consist of different analog to digital and digital to analog converters, delays, along with analog circuit components and an array of antennas. When a signal is received from the array of antennas, they are sampled by analog to digital converter (ADCs). These signals are usually down converted to low frequencies and mixed with complex sinusoidal signals which then creates a baseband signal. A channelizer is used to split these baseband signals into different channels. The resulting channel signals are then fed into a beamformer. This beamformer applies different phase delays and correction coefficients to each channel signals before summing all the channel to produce a radiated beam [48] as seen from figure 1.3.

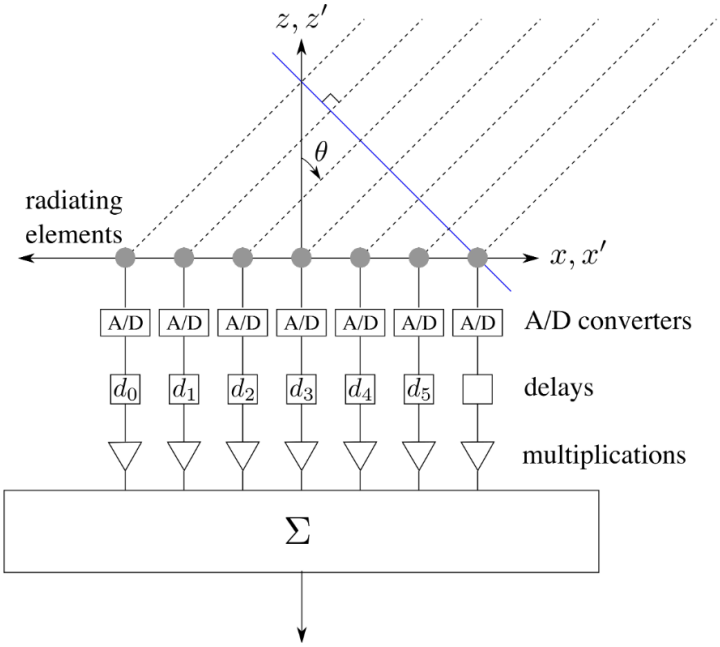

Figure 1.3 Digital Beamformer [49]

Spatial filtering is provided to the array of antennas as the beamformer acts as a signal processing device. Time domain and frequency domain processing are used for wideband beamforming. Frequency domain processing uses a FFT for frequency domain conversion and filter, and digital delay lines are used for time domain processing. Digital beamforming gives good flexibility in beamforming. However, it has certain disadvantages since it is limited to low-microwave frequencies due to low bandwidth of current analog to digital converters and requires fast processors, also implying substantial power consumption.

1.3 Lens Based Beamformers

With a lens-based beamforming networks (BFN) the beam angles are fixed, while beamwidths change accordingly with frequency, causing crossover levels to change with frequency. The examples of the lens based BFNs are the Luneburg lens, Ruze lens and Rotman lenses. These type of beamformers are known as true time delay structures since their working does not depend on the frequency of operation.

1.3.1 Luneburg Lens

Luneburg lens was the first lens based beamformer. This lens has gradient index, and the structure of this lens is spherically symmetric. In this lens refractive index decreases radially from center to the outer surface. Because of this property there are two conjugate foci outside of the lens as shown in figure 1.4. Because of this type of structure this lens is also known as shell lens. These lenses are usually used for radar calibrations and to develop highly efficient microwave antennas.

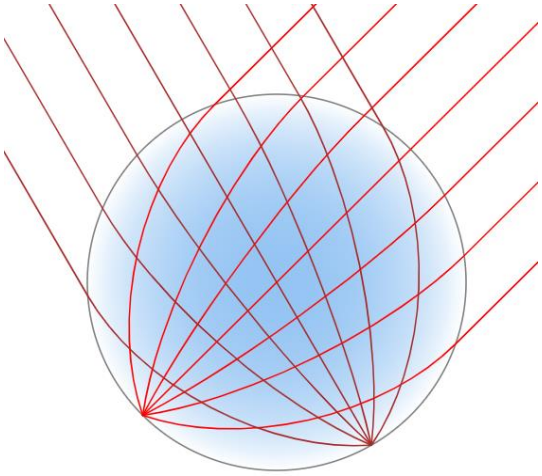

Figure 1.4 Luneburg Lens [50]

1.3.2 Ruze Lens

The Ruze lens beamforming technique is shown in Figure 1.5. A Ruze lens consists of metal parallel plates that are capable of constraining energy to travel parallel to the axis of the lens and rays within the lens travel parallel to path P–Q. The electrical path within the lens can be formed in a variety of ways such as waveguide, coaxial line, stripline, or microstrip [51]. Using ray tracing through points P–Q and the lens origin, two focal points F1 and F2 are assumed along the focal arc [52]. Various types of Ruze lenses can be designed by changing the shape of the inner contour and the thickness of the lens.

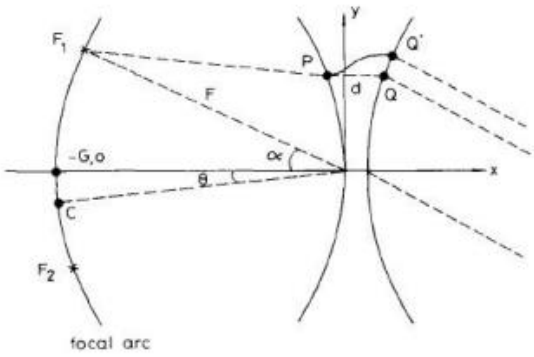

Figure 1.5 Ruze Lens [51]

1.3.3 Rotman Lens

In microwave frequency microwave lenses are another class of multiple beamforming network. Rotman Lens got very popular as a beamforming network because it is cost effective, reliable, easier to implement and it can be used for wide bandwidths. Unlike analog beamforming, it avoids the use of delay lines, phase shifters, directional coupler, and cross overs. Rotman lens is known as a true time–delay device since its operation is independent of frequency and it is capable to steer the beam at any frequency. This is the reason why it can be used for wide–band operation. Just like Ruze lens, Rotman Lens is also a parallel plate device used to feed an antenna array. Rotman lens design can be calculated using the foci method, it has dummy ports for absorbing the evanescent fields, it has beam ports as inputs and array ports used as output which are connected to the array of antennas. Different path lengths are created in a Rotman Lens which is essential to produce time delay between the adjacent elements which helps achieve beamsteering [39].

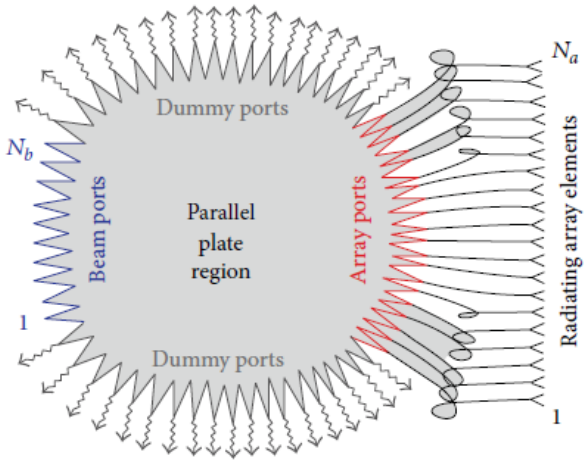

Figure 1.6 Rotman Lens [39]

1.4 More Generalized Quasi Optical Approach

Beams interacting with lens type structures with few wavelength dimensions hence Quasi- optical.

Quasi optics involves beams of radiation propagating in free space; operations on these beams can be implemented directly using spatially distributed approaches such as amplifier and filtering arrays; these systems have been built for mmWave radar, plasma diagnostics, astronomy etc. for many years and have been proven to be a very important technology for multi-frequency antenna and beamforming systems. Because of the above-mentioned limitations of currently available beamforming techniques, designing a more generalized quasi-optical approach which will work for higher frequency ranges will be groundbreaking.

As the operating frequency increases and since all the communication industry is moving towards mmWave frequencies, many conventional beamforming techniques will be unable to meet needed specifications because of losses and frequency limitations. To realize this technique partially reflective surfaces, shaped dielectrics and metamaterials are potential candidates for inhomogeneous lens type structures to perform the beamforming operation. Simulations to date have demonstrated beamshaping and beamsteering using metamaterials in partially reflective surfaces. Ansys HFSS (High Frequency Structure Simulator) is used to simulate these structures with absorbing boundary conditions (radiating boundary) for few element arrays structures. The use of partially reflective structures with different shapes have shown increase of 67% in antenna directivity. Incorporating nonplanar metamaterial structures has demonstrated beamsteering capability of ±30 degrees. Optimization techniques are used to determine proper shape and orientation of these structures to get multiple non-overlapping highly directional pencil beams.

This quasi-optical approach will enhance performance of emerging systems such as broad deployment of 5G backhaul communications, Internet of Things (IOT), vehicular networking systems, and unmanned aerial navigation systems. It is showing promise as a new beamforming methodology that will extend frequency realization, reduce power consumption, and reduce cost and weight.

1.5 Comparison Table

TYPE	FEATURES	ADVANTAGES	DISADVANTAGES
Analog Beamforming Networks	• Butler matrix, Blass Matrix, Wullenweber array. • Consists of alternate rows of fixed phase shifters and hybrid junctions.	• Small arrays are easier to construct. • Using Butler matrix reduces the number of components. • Blass matrix can be used for wide bandwidth.	• Finite insertion losses. • Practically limited complexity. • Butler Matrix is frequency dependent.
Digital Beamforming Networks	• Uses digital processors to control electronic components to form amplitude and phase for different channels of array elements.	• Low phase error, flexible amplitude tapering, and large number of scanning steps. • It's easy to make the process adaptive.	• Limited to low microwave frequencies without extensive up and down conversion. • Requires fast processors and high-power consumption.

Microwave lens Beamforming network	• Rotman Lens, Ruze Lens, Luneburg lens.	• Frequency independent • Wide bandwidth	• Lack of flexibility in beamforming • Challenging to implement for larger number of ports.
Quasi Optical Approach	• Lens type structure is used to form multiple minimally overlapping beams.	• Reduces size, cost and improves the efficiency of beamforming. • Used at low as well as high microwave frequencies. • Frequency tuning and bandwidth adjustment is relatively easier.	• Matching layers can make the design bulky.

Table 1.1: Comparison of different types of beamformers

1.6 Contribution to this work

As a part of this work a unique method of quasi-optical beamforming for high millimeter wave frequencies has been proposed to form multiple minimally overlapping beams and get a proper control on beamsteering angles. The contributions of the current work are as follows,

1. Demonstration of beamsteering using horizontal wedges.
2. Beamsteering using partially reflective surfaces which are designed using broadside coupled split ring resonators has been demonstrated.
3. Beamsteering using vertical broadside coupled split ring resonators has been demonstrated.
4. A complete control on E and H principal plane radiation patterns by carefully orienting these structures in 1-3 has been studied and demonstrated.
5. A complete analysis of horizontally oriented dielectric wedges along with the matching layers has been studied and demonstrated along with their usage in the beamforming approach.
6. A complete analysis of convex lens shaped dielectric slabs has been studied and demonstrated to produce minimally overlapping beams.
7. A complete analysis of plano-concave lens type structures is studied and its application in beamsteering angle control by changing the radius of curvature is demonstrated.
8. A complete analysis of vertical dielectric wedges type structures is studied and its application in beamsteering angle control by changing the tilt angles of wedges is demonstrated.
9. The results have been validated by comparing simulation results using Ansys HFSS and CST MWS.
10. The highest performing beamforming approach was also evaluated for bandwidth and scalability.

The rest of the dissertation is organized as follows. Chapter 2 evaluates different types of materials

along with their properties. In chapter 3, patch antenna and applications of partially reflecting surfaces is introduced, including the design procedure and explaining their impact on directivity, beamwidth and gain enhancement. Chapter 4 explores different beamsteering approaches with dielectric wedges, partially reflective surfaces and vertical split ring resonators. In chapter 5 the quasi-optical beamforming is explained along with the complete demonstrations of various structures and their applications for beamsteering angle control. Chapter 6 explores effects of quasi-optical structures on bandwidth and scalability. The last section provides the concluding remarks and the scope of future work.

1.6 Numerical Techniques to Solve Electromagnetic Problems

Many computational electromagnetics numerical techniques are being used to study the electromagnetic behaviors of different periodic/ aperiodic structures. There are many numerical techniques which have been investigated, but the most popular numerical methods are based on Time Domain-Differential equations such as Finite Difference Time Domain (FDTD), Finite Element Method (FEM) or Finite Element Analysis (FEA) and Frequency Domain-Integral Equations methods such as Method of Moments (MoM), and Finite Difference Frequency Domain (FDFD). These numerical techniques are implemented by commercial simulation software packages. In this dissertation Ansys HFSS (High Frequency Structure Simulator) has been used which is based on FEM method.

Ansys HFSS is used for high frequency devices, antennas designing, arrays of antenna, microwave and RF components and circuit design. It is an electromagnetic software with 3D user interface. For such high resonant structures finite element solver is considered accurate. This software gives enough degrees of freedom to simulate the finite array structures by applying proper boundary conditions.

All the simulations have been carried out using Intel Precision Tower 5810, with 80 GB RAM, 8 GB Nvidia Graphics card and 3 TB SSD.

CHAPTER 2:

MATERIALS EVALUATION

Considerable study was performed to search the suitable material for beamforming application which will be light weight, low loss, low cost, and high electric tunability. A low loss dielectric material with reasonably high dielectric constant is quite expensive. In this chapter an extensive study of different types of materials and their properties has been carried out.

2.1 Lens

At millimeter wavelengths lens antennas become of more reasonable size, offering good directivity, low insertional loss and easier fabrication. Figure 2.1 shows the spherical lens being placed in front of the antenna. The lens is made of glass materials and the dielectric constant is $\varepsilon_r = 5.5$. Its working principle is based on the fact that electromagnetic waves interacting with lens will be refracted based on the angles at which the waves hit the lens. In principles the operation is similar to that of the optical lens. The focal length of the lens can be calculated using,

$$\frac{1}{f} = (\eta - 1)\left(\frac{1}{R_2} - \frac{1}{R_1} + \frac{(\eta - 1)d}{\eta R_1 R_2}\right)$$

Where f is the focal length, η is the refractive index, $R_1 R_2$ are the radius of curvature and d is the thickness of the lens.

The height h is calculated using the principles of phase center. Figure 2.2 shows the gain plots for different angles which are varied along E principal plane i.e., y axis. As seen from figure 2.2 the radiation plots steer from -30 degrees to 30 degrees as the angle of the lens varies from -y axis to +y axis.

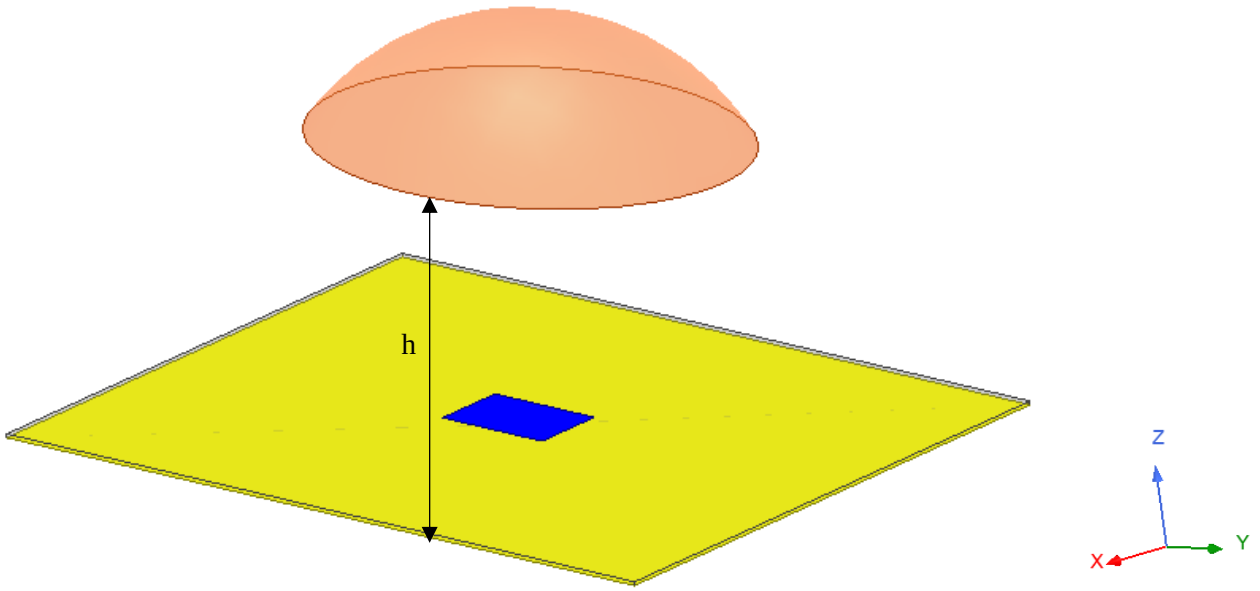

Figure 2.1 Spherical Lens placed on top of Antenna.

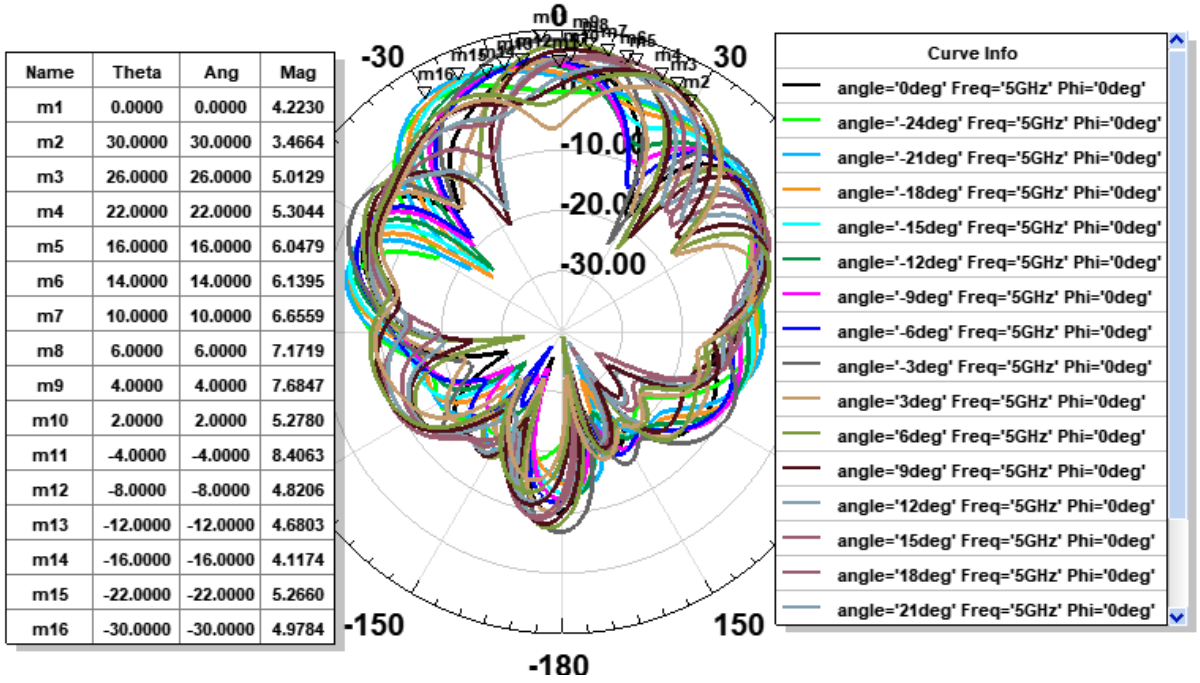

Name	Theta	Ang	Mag
m1	0.0000	0.0000	4.2230
m2	30.0000	30.0000	3.4664
m3	26.0000	26.0000	5.0129
m4	22.0000	22.0000	5.3044
m5	16.0000	16.0000	6.0479
m6	14.0000	14.0000	6.1395
m7	10.0000	10.0000	6.6559
m8	6.0000	6.0000	7.1719
m9	4.0000	4.0000	7.6847
m10	2.0000	2.0000	5.2780
m11	-4.0000	-4.0000	8.4063
m12	-8.0000	-8.0000	4.8206
m13	-12.0000	-12.0000	4.6803
m14	-16.0000	-16.0000	4.1174
m15	-22.0000	-22.0000	5.2660
m16	-30.0000	-30.0000	4.9784

Figure 2.2 Gain Plot for E principal plane for spherical lens placed on top of antenna.

This scheme of lens works well when the refractive index is low, if the refractive index of the lens is too high then the problem of impedance matching occurs. If this lens is placed in near field of antenna,

then the reflections will be high resulting in inefficiency and possible pattern distortion. Matching layer/ layers provide a possible solution to resolve the impedance matching problems. By introducing these layers reflections can be reduced considerably. This is discussed in great details in chapter 5.

2.2 Dielectric Wedges

This is the one of the simplest techniques to produce the required amount of beam steering. Because of finite size wedges there can be an issue of beam spillover, to avoid this spillover the wedges are placed in the reactive near field of antenna since the beams are undistorted. Fig (2.3a) and (2.3b) show two possible ways to place the horizontal wedges above the antenna to achieve beamsteering. Using the concept of Risley prism the wedges are placed in such a way that they can be rotated individually around the axis**.**

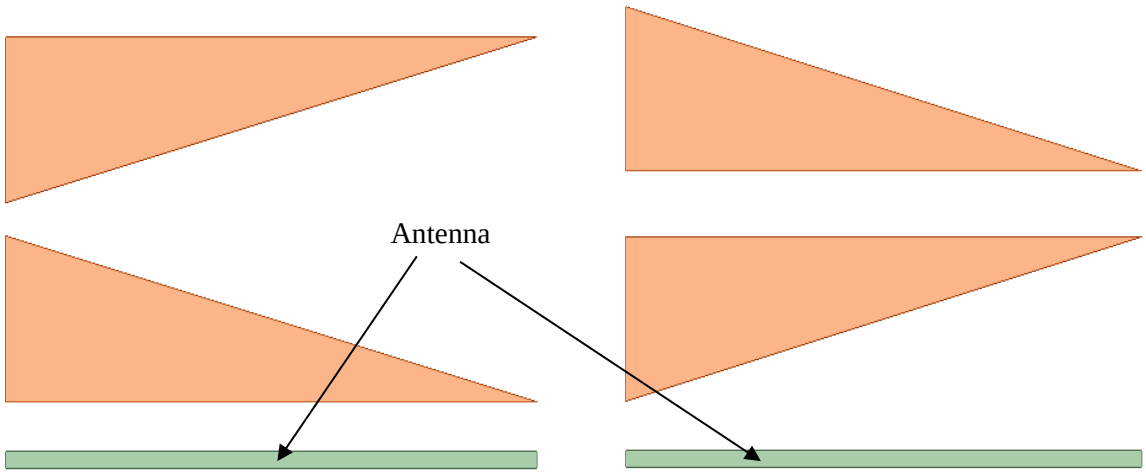

Figure 2.3 Dielectric Wedges placed on top of Antenna.

The flaring angle and the dielectric constant of the wedge are responsible for the level of beamsteering that can be achieved. With proper matching layer and high dielectric constant wedges the beam can be steered at much wider angles. Assuming planar wavefront beam steering angle can be estimated using Snell's law. This law can be applied at microwave frequencies when the material size is much larger than the wavelength. But as the size of the material used gets smaller in size the propagation

inside the material cannot be assumed to be plane wave since the diffraction effect in the transmitted wave is more. A detailed explanation is given in chapter 4.

2.3 Overview of Metamaterials

The lens and wedges can be implemented using sheets and volumes of metamaterials. The concept of negative refraction was introduced in the 1960's by Russian physicist Victor Veselago. Metamaterials are artificial materials which cannot be found in nature. These structures tend to exhibit negative refractive index, and produce extraordinary electromagnetic responses, because of their subwavelength structure. In the microwave region naturally occurring magnetization is not possible due to high inertia and materials cannot track the electromagnetic fields. Therefore, it is important to designing materials where naturally occurring magnetization is not possible [65]. This section gives a detailed explanation of different types of metamaterials and their properties.

2.3.1 Metasurfaces

Metasurfaces are the 2-dimensional metamaterials that can be designed; hence they are also known as a class of 2D metamaterials. Figure 2.4 shows a simple metasurfaces. Metasurfaces are planar and can be fabricated using precision milling and nano-printing techniques [57, 58]. The working principle of metasurfaces depends on the laws of diffraction, hence these materials are also known as subwavelength structures. The diffraction of rays depends on the lattice constant, wavelength, angle of incidence and type of dielectric used. Since these are planar structures, they occupy less space, and the design complexity is low so does the simulation time and they are cost effective. These structures are considered as a homogeneous material with an effective permittivity and permeability. Metasurfaces are passive devices and can be used for increasing the directivities of antennas, they are also used in filter design, designing cloaking devices and superlens. Metasurfaces have been used for beamsteering control of antennas by introducing the necessary phase gradient. By adding multiple

layers of these structures to introduce phase delay, the computational time and power required increases considerably.

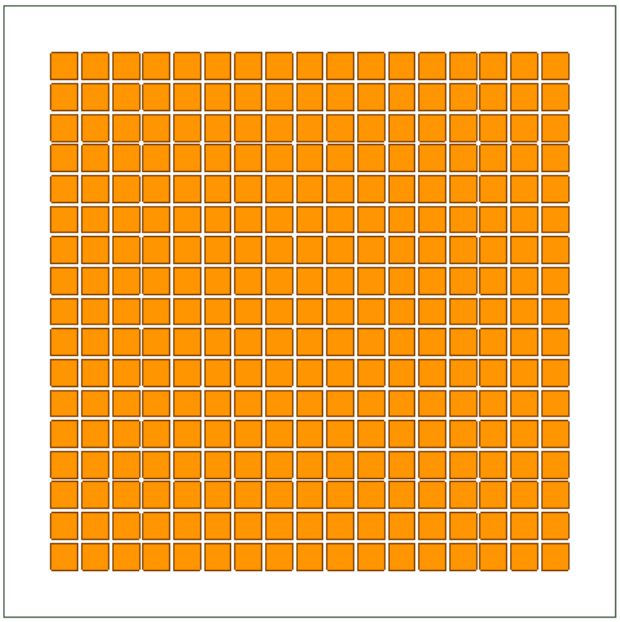

Figure 2.4 Simple Metasurfaces.

2.3.2 Frequency selective surfaces

Frequency selective surface (FSS) have been a center of research in the electromagnetics community. Many techniques have been investigated to properly design and to make these structures realizable. FSS are two-dimensional periodic structures which are printed on a dielectric substrate capable of total transmission or reflection at a designed resonant frequency. Conformal FSSs have several applications in the field of antenna design such as radomes, reflectors, and sub reflectors for large aperture antennas. reflector antennas, quasi optical microwave devices like resonant beam splitters and lens antennas. There are certain disadvantages associated with these structures, as the electrical length of the unit cell increases there is angular instability in an array of FSS. Figure 2.5 shows a simple inductive FSS grid.

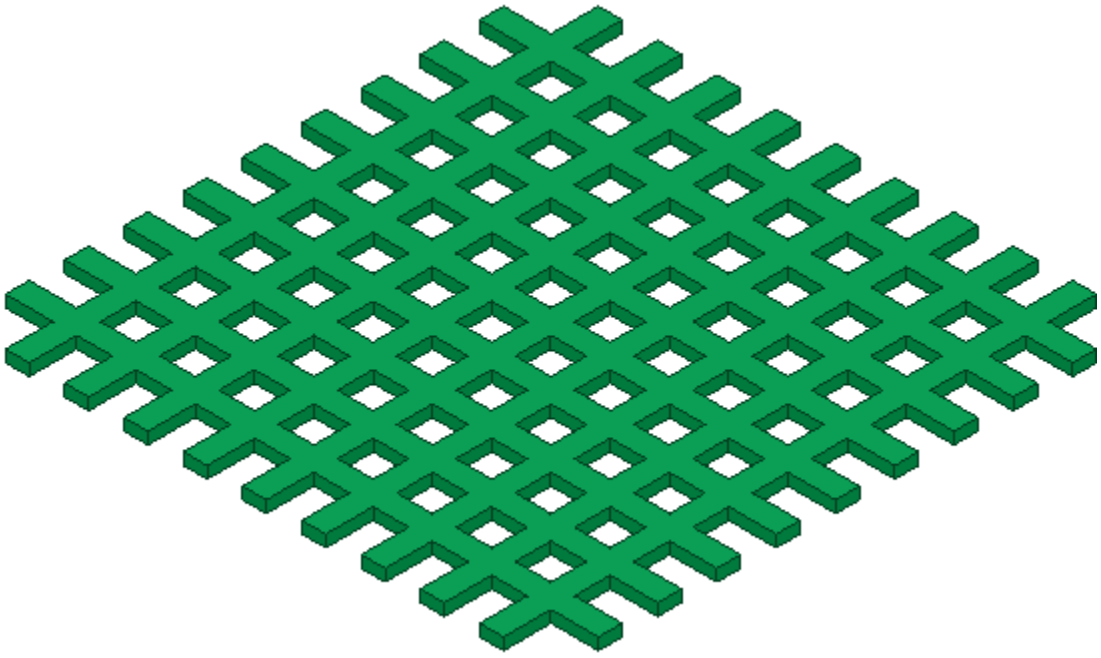

Figure 2.5 Inductive FSS grid.

2.3.3 Artificial Magnetic Conductors

If the incident waves are to be reflected by 180 degrees, then a perfect electric conductor (PEC) is used and if 0-degree phase shift is required then perfect magnetic conductors (PMC) are used. But PMC does not exist in nature. Therefore, artificial magnetic conductors are designed which will work as an equivalent alternative to a perfect magnetic conductor. This type of structure was first designed by Sievenpiper [54]. A 2D periodic arrays of square metallic patch-type elements on a grounded dielectric substrate, can introduce a zero degrees reflection phase shift to incident waves. These structures are used in designing quasi-TEM waveguide where speed of light in free space is equal to the phase velocity so that the distribution of field is uniform at the center of waveguide. The drawback of these structures includes zero-degree reflection just at one frequency point (only for one resonant mode). Figure 2.6 shows the basic working of an artificial magnetic conductor.

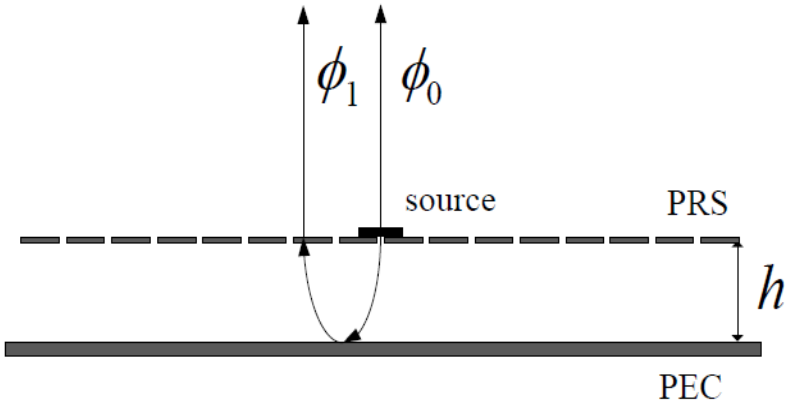

Figure 2.6 Artificial Magnetic Conductor.

2.3.4 Split Ring Resonator

Sir John Pendry first realized the concept of metamaterials by introducing split ring resonators. These structures possess negative permittivity and negative permeability simultaneously. The figure 2.7 shows the split ring resonator, a single cell SRR has a pair of enclosed loops with splits in them at opposite ends to provide negative permeability and the wire is included on the other side of substrate which provides negative permittivity. The loops are made of nonmagnetic metal like copper and have a small gap between them. The loops can be concentric circles, hexagons or squares [8]. The Split Ring Resonator (SRR) is the first introduced structure that forms the basic unit cell of a metamaterial. Because of their subwavelength dimensions the incident waves will be diffracted rather than refracted. They are critical when a response is required at near infrared and optical wavelengths. When an external magnetic field H_{ext} is incident (see Figure 2.7) normal to the plane of these resonating cells (inclusions), the change in the magnetic flux enclosed by these rings induces an electromotive force (emf) in the rings. Because of this emf current is generated. This circulating current generates a magnetic moment normal to the inclusion plane and this magnetic moment is the metamaterial equivalent to the atomic magnetic dipole moment of naturally permeable materials. Table 2.1 shows

the dimensions for split ring resonator unit cell.

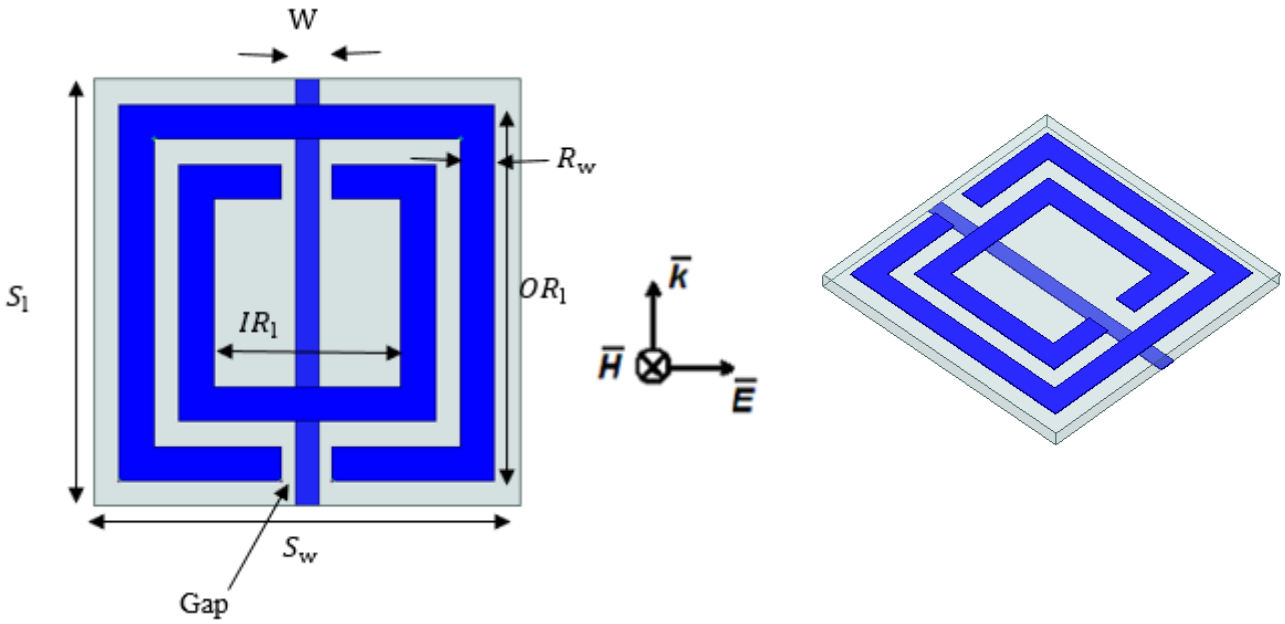

Figure 2.7 Split Ring resonator unit cell

Symbol	***Parameter***	***Value (mm)***
S_l	Substrate Length	5
S_w	Substrate Width	5
OR_l	Outer Ring Length	4.4
IR_l	Inner Ring Width	3
R_w	Ring Width	0.4
Gap	Slit width	0.6
W	Wire Width	0.28

Table 2.1: SRR Dimensions

The working principle of SRR can be better understood by comparing them with an LC oscillating circuit containing a coil of inductance L and capacitor of capacitance C. An inductor L is effectively realized with the loops in SRR and the gaps between the rings and splits in the rings effectively realizes the capacitance. Figure 2.8 shows the corresponding equivalent circuit, where *L*, *R* are the equivalent inductance and resistance, respectively; C_0 is mutual capacitances between the two rings; C_s is the capacitance of the split [30].

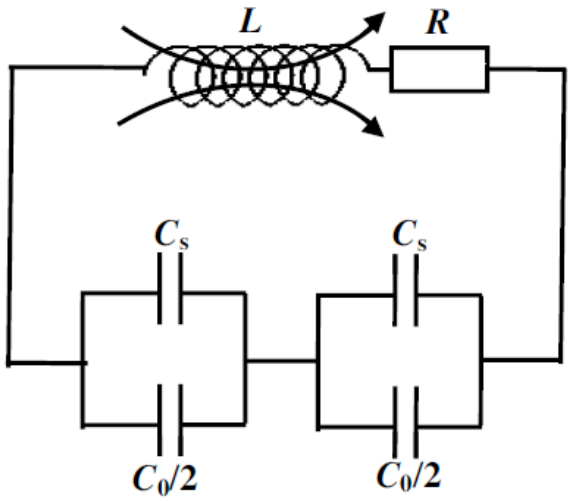

Figure 2.8 Circuit equivalent of the SRR [30]

Certain procedure is to be followed to get the S parameters of the split ring resonators. The procedure described is realized in Ansys HFSS. An infinite array of SRR is assumed to successfully realize the design. This can be achieved by imposing boundary conditions, in HFSS there are two types of boundary conditions to realize the infinite array; first is master slave boundary condition along with floquet port excitation and other is PEC and PMC boundary condition with wave ports. Figure 2.9 shows the PEC (red), PMC (turquoise) and wave ports (green). These cells are simulated on FR4 substrate with $\epsilon_r = 4.4$ and loss tangent $\tan\delta = 0.02$. The substrate thickness is 1.6 mm, and these structures are designed for 5GHz resonant frequency. Figure 2.10 (a), 2.10 (b) shows the S parameter

plots for S11 and S21 in phase and magnitude of the SRR unit cell, it can be seen the resonance is happening at 5 GHz. The resonance in the phase of S_{21} confirms the presence of negative index band which will be confirmed by using parameter retrieval technique.

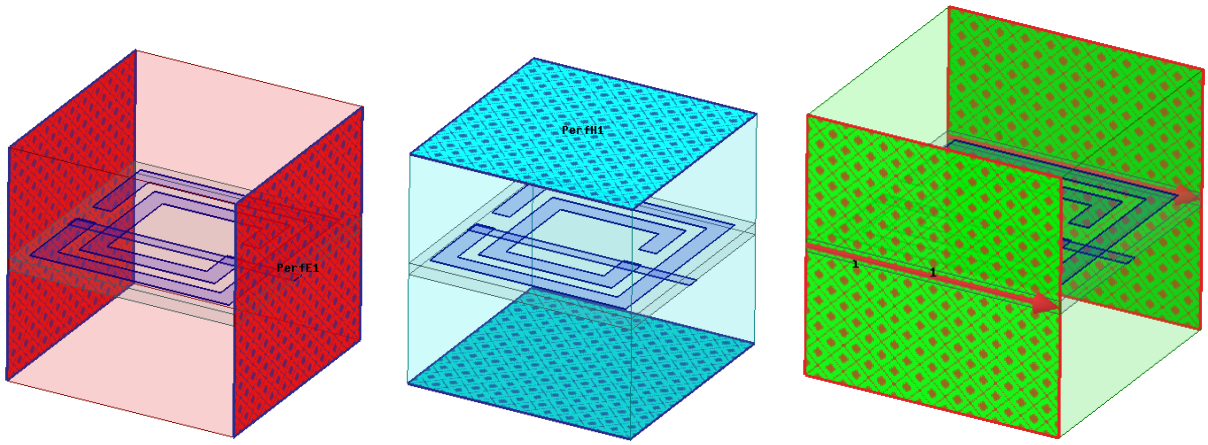

Figure 2.9 SRR Unit cell simulation setup in HFSS

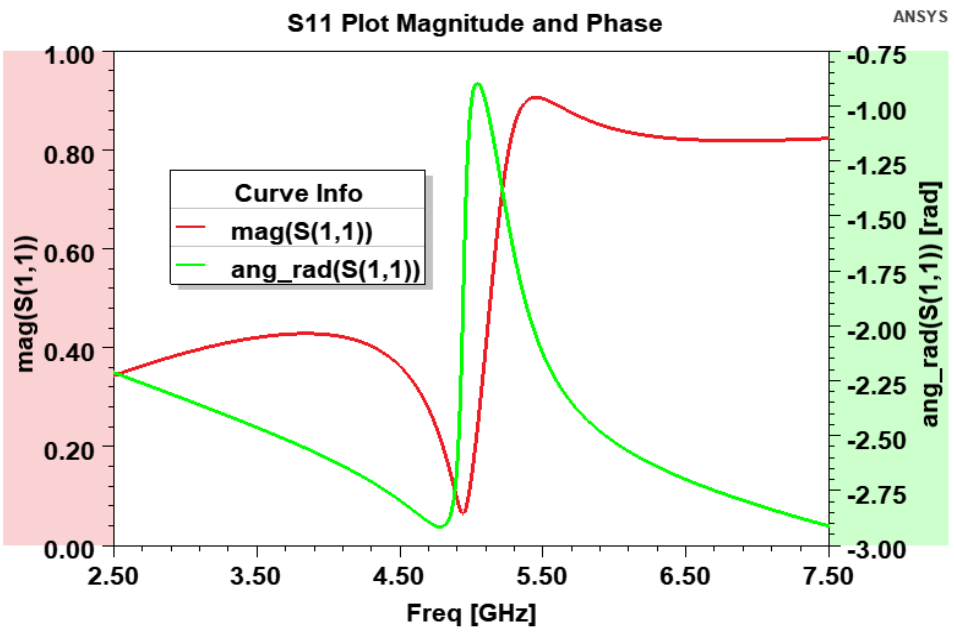

(a)

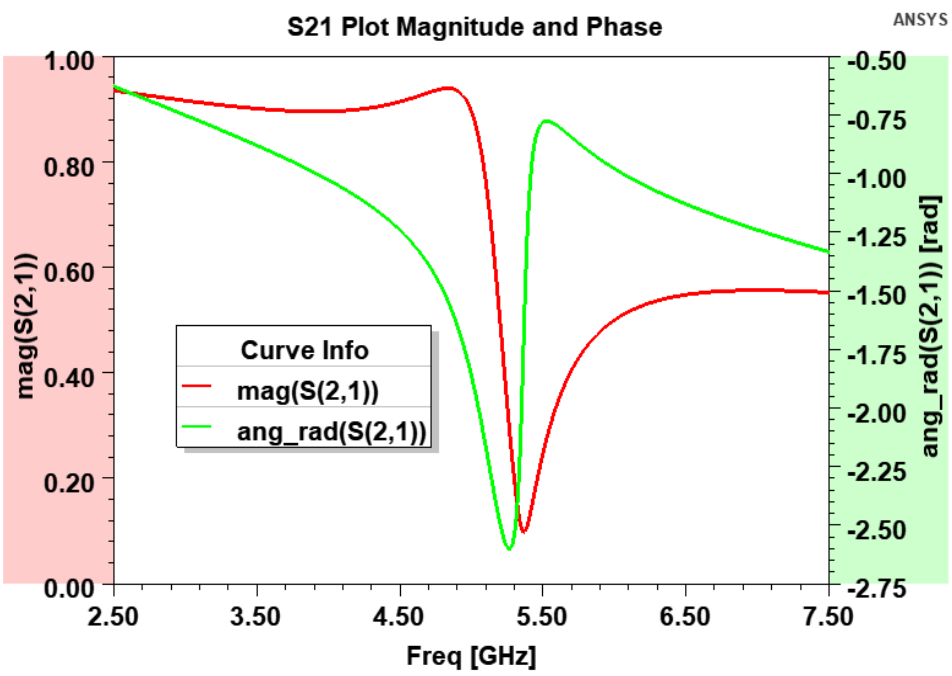

(b)

Figure 2.10 S Parameter plots for SRR (a) Magnitude and Phase plot of S11 (b) Magnitude and Phase plot of S21

2.3.4.1. Mathematical Formulation of Split Ring Resonator

This section is helpful in understanding the interaction of wave with the SRR surface. SRR behave as an LC resonator that can be excited by external magnetic flux. SRR exhibit cross-polarization so that the excitation by properly polarized time varying external electric field is also possible [31].

Angular frequency is calculated as

$$\omega_0 = \sqrt{\frac{1}{L_T C_{eq}}}$$

SRR can be of different shapes, the most used SRR's are circular, hexagonal, square etc. The resonant frequencies of each type are calculated using the following formulas.

Resonant frequency of circular SRR

$$f_0 = \frac{1}{2\pi\sqrt{L_T C_{eq}}} = \frac{1}{2\pi\sqrt{L_T\left[\frac{(\pi r - g)C_{pul}}{2} + \frac{\epsilon_0 wt}{2g}\right]}}$$

Resonant frequency of hexagonal SRR

$$f_0 = \frac{1}{2\pi\sqrt{L_T C_{eq}}} = \frac{1}{2\pi\sqrt{L_T\left[\frac{(3a_{avg} - g)C_{pul}}{2} + \frac{\epsilon_0 wh}{2g}\right]}}$$

Resonant frequency of square SRR

$$f_0 = \frac{1}{2\pi\sqrt{L_T C_{eq}}} = \frac{1}{2\pi\sqrt{L_T\left[\left(2a_{avg} - \frac{g}{2}\right)C_{pul} + \frac{\epsilon_0 wt}{2g}\right]}}$$

Where,

$$C_{pul} = \frac{\sqrt{\epsilon_e}}{cZ_0} \; and \; L_T = 0.00508l\left(2.303\log\frac{4l}{d} - \Theta)\right)$$

d = distance of wire

l = length of wire

Θ = varies with wire geometry

2.3.4.2 Parameter Retrieval Method

Effective permittivity and permeability are the properties which metamaterials possess, and they can be defined from such properties. Extensive research has been carried out to retrieve the effective parameters of metamaterials efficiently. A very commonly used technique to retrieve $\mu \; and \; \epsilon$ is based on the S-parameters. This technique is most effective when it comes to calculate the effective

parameters from simulated as well as measurement results as this method uses S parameters results from electromagnetic simulators and measured results from vector network analyzer (VNA) [15]. Figure 2.11 shows S parameter on homogeneous 1D slab of thickness d.

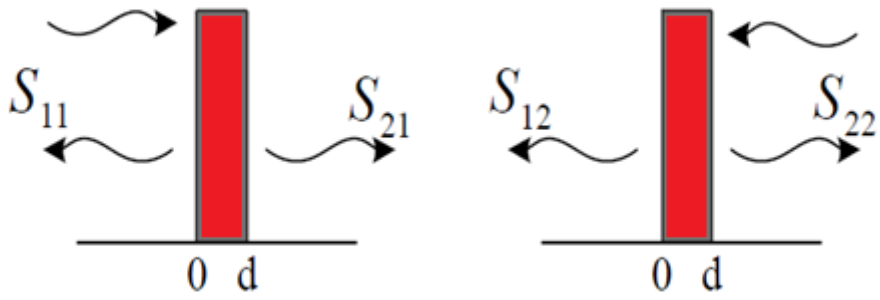

Figure 2.11 S parameter on homogeneous 1D slab of thickness d [15]

One dimensional transfer matrix is defined as

$$F' = TF$$

Where,

$$F = \begin{pmatrix} E \\ H_{red} \end{pmatrix}$$

Where E and H_{red} are complex electric and magnetic field amplitudes $H_{red} = (+i\omega\mu_0)H$

$$T = \begin{pmatrix} cos(nkd) & -\frac{z}{k}\sin(nkd) \\ \frac{k}{z}\sin(nkd) & \cos(nkd) \end{pmatrix}$$

Where k is the wavenumber, d is the slab thickness, n is the refractive index and z is the wave impedance of the slab, z and n are related to ε and μ by the relations.

$$\varepsilon = \frac{n}{z} \; and \; \mu = nz$$

For homogeneous slab $T_{22} = T_{11} = T_s$ and det(T) = 1

$$\therefore\ S_{11} = S_{22} = \frac{\frac{1}{2}\left(\frac{T_{21}}{ik} - ikT_{12}\right)}{T_s + \frac{1}{2}\left(ikT_{12} + \frac{T_{21}}{ik}\right)}$$

$$\therefore\ S_{21} = S_{12} = \frac{1}{T_s + \frac{1}{2}\left(ikT_{12} + \frac{T_{21}}{ik}\right)}$$

By using analytical expression

$$\therefore\ S_{11} = S_{22} = \frac{i}{2}\left(\frac{i}{z} - z\right)\sin(nkd)$$

$$S_{21} = S_{12} = \frac{1}{\cos(nkd) - \frac{i}{2}\left(z + \frac{1}{z}\right)\sin(nkd)}$$

$$n = \frac{1}{kd}\cos^{-1}\left[\frac{1}{2S_{21}}(1 + S_{11}^2 + S_{21}^2\right]$$

$$z = \sqrt{\frac{(1 + S_{11})^2 - S_{21}^2}{(1 - S_{11})^2 - S_{21}^2}}$$

The above relations bring multiple solutions due to inverse cosine and square roots. These can be solved by choosing $Re(z) \geq 0\ and\ Im(n) \geq 0$. Figure 2.12 (a), (b), (c), (d) shows the results for effective permittivity, effective permeability, negative refractive index, and impedance. The real part of refractive index is less than zero which indicates the presence of negative refractive index. The *S* parameters for the unit cell of Fig. 2.7 are computed using Ansys HFSS. These S parameters are then imported in MATLAB and parameter retrieval formulations are used.

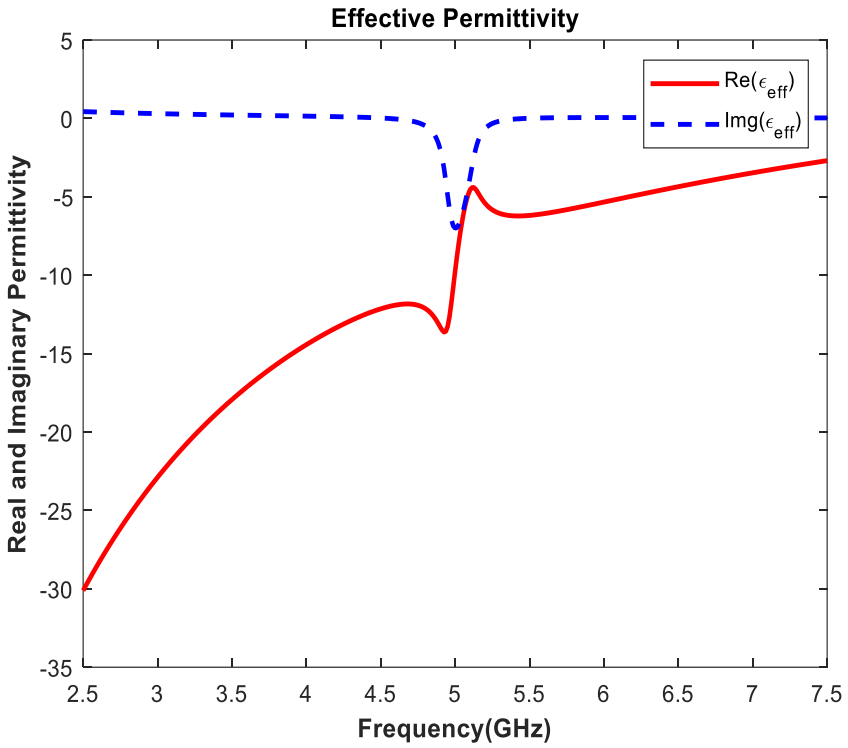
Effective Permittivity
Re(ϵ_{eff})
Img(ϵ_{eff})
Real and Imaginary Permittivity
Frequency(GHz)
5
0
-5
-10
-15
-20
-25
-30
-35
2.5
3
3.5
4
4.5
5
5.5
6
6.5
7
7.5

(a)

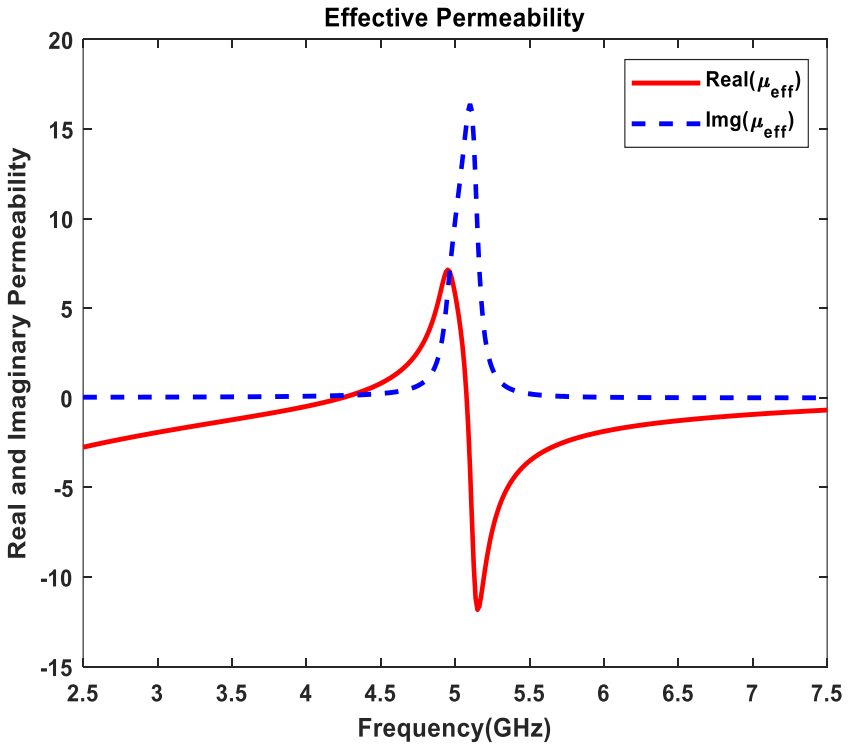
Effective Permeability
Real(μ_{eff})
Img(μ_{eff})
Real and Imaginary Permeability
Frequency(GHz)
20
15
10
5
0
-5
-10
-15
2.5
3
3.5
4
4.5
5
5.5
6
6.5
7
7.5

(b)

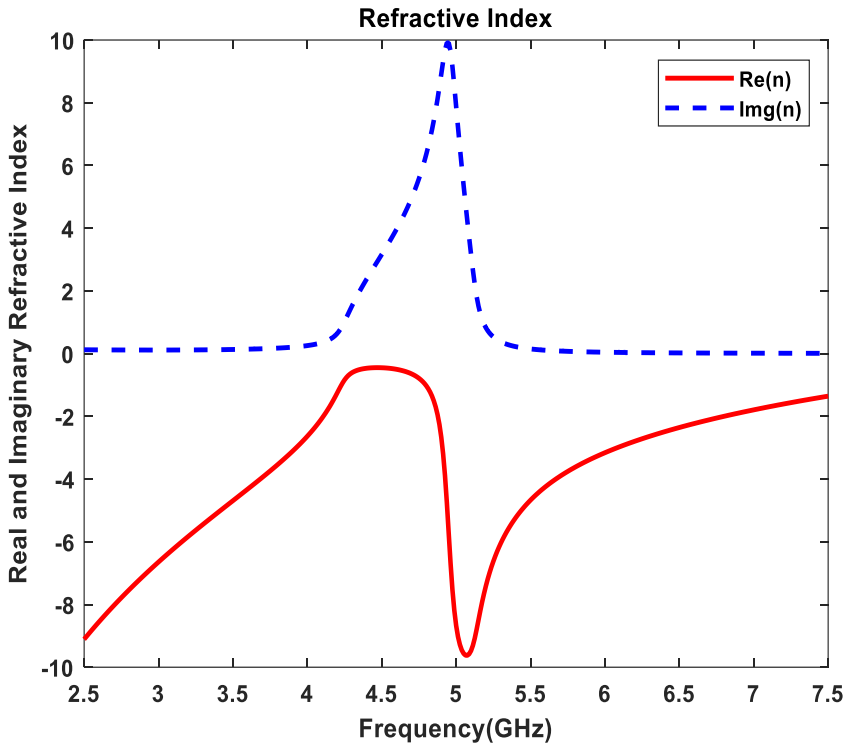
Refractive Index
Re(n)
Img(n)
Real and Imaginary Refractive Index
Frequency(GHz)
10
8
6
4
2
0
-2
-4
-6
-8
-10
2.5
3
3.5
4
4.5
5
5.5
6
6.5
7
7.5

(c)

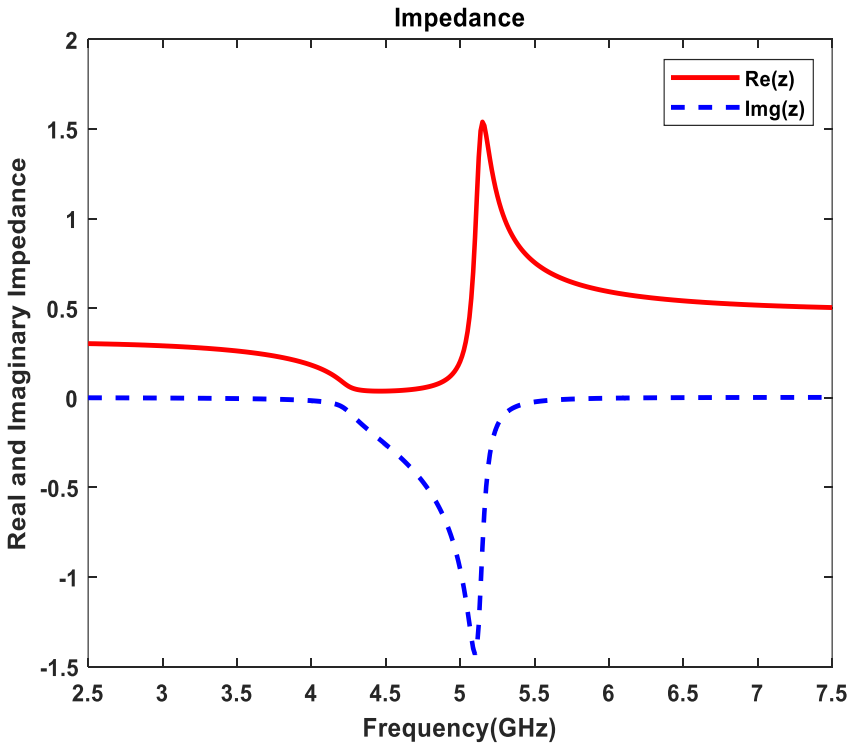
Impedance
Re(z)
Img(z)
Real and Imaginary Impedance
Frequency(GHz)
2
1.5
1
0.5
0
-0.5
-1
-1.5
2.5
3
3.5
4
4.5
5
5.5
6
6.5
7
7.5

(d)

Figure 2.12 Parameter Retrieval plots for SRR showing real and imaginary values of (a) permittivity (b) permeability (c) refractive index (d) Impedance

2.3.4.4 Broadside Coupled Split Ring Resonator

The unit cell of BCSRR compose of two rings printed on both sides of the substrates with the split in the opposite locations. The splits in the rings make support layer resonant wavelength. Figure 2.13 shows the unit cell of broadside coupled split ring resonator. Capacitance is induced in between splits and in between two rings. The dimensions of these rings are small as compared to the wavelength. These structures have wide transmission frequencies than edge coupled split ring resonators (EC-SRR) and double-sided split ring resonators DS-SRR. The size of BCSRR is small as compared to the other types and it provides highest resonance bandwidth. BCSRR does not possess cross polarization.

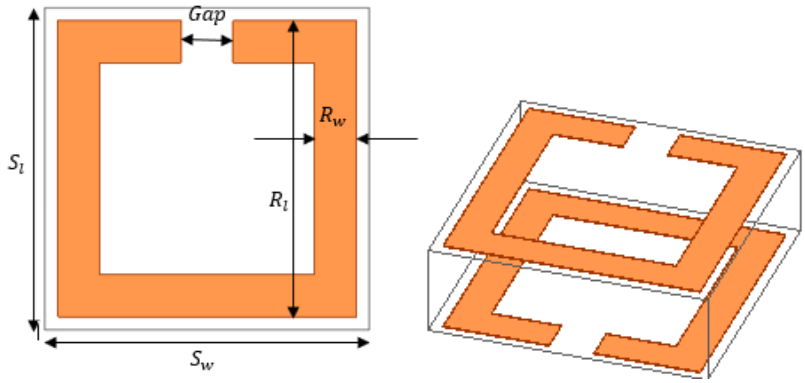

Figure 2.13 Broadside coupled split ring resonator [77].

Table 2.2 shows the BCSRR unit cell dimensions. Figure 2.14 (a) and 2.14 (b) shows the S parameter plots of the above unit cells. These cells are simulated on FR4 substrate with $\epsilon_r = 4.4$ and loss tangent

$\tan\delta = 0.02$. The substrate thickness is 1.6mm and these structures are designed for 5GHz resonant frequency.

Symbol	*Parameter*	*Value (mm)*
S_l	Substrate Length	5
S_w	Substrate Width	5
R_l	Ring Length	4.6
R_w	Ring Width	0.65
Gap	Slit width	0.8

Table 2.2 BCSRR Dimensions

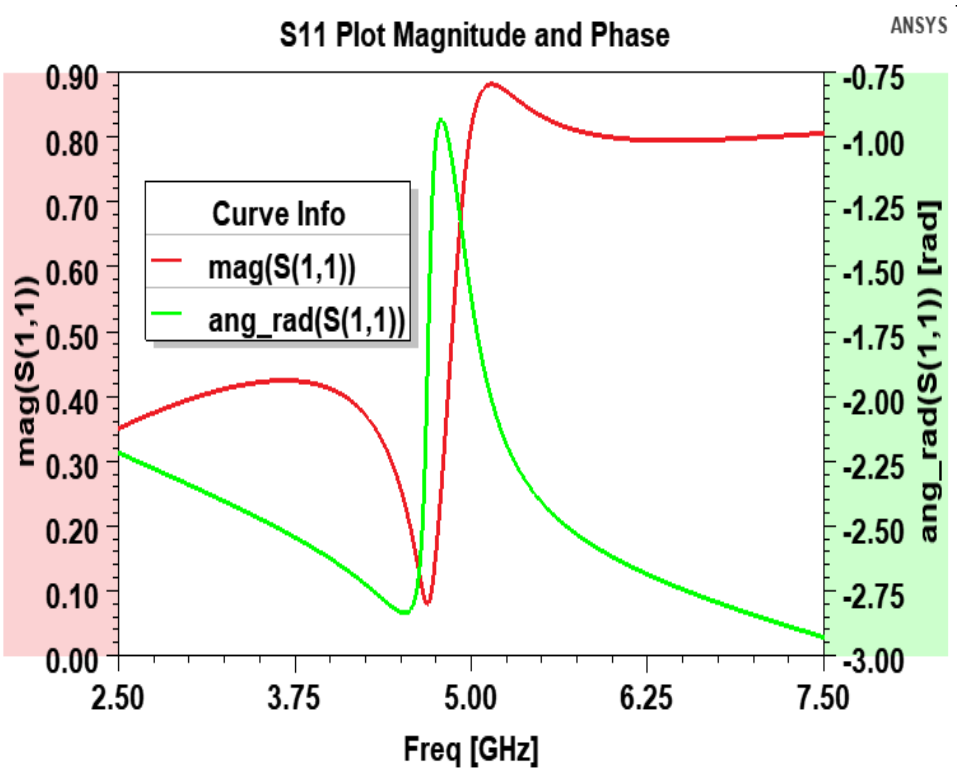

(a)

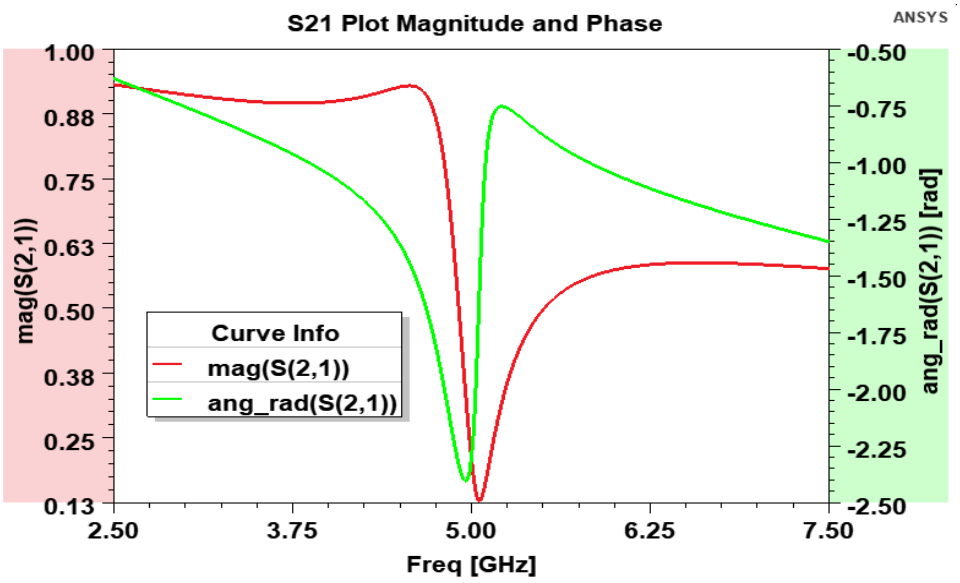

(b)

Figure 2.14 S parameter plots for BCSRR (a) Magnitude and Phase plot of S11 (b) Magnitude and Phase plot of S21

2.3.4.5 Tunable BCSRR

In the above section the BCSRR will have the resonance at one particular frequency. BCSRR can be made tunable by designing two rings on different layers of two substrates, by doing this the position of the two substrates can be varied which will change the sheet impedance of the structure which will in turn change the resonant frequency. This type of structure is also known as frequency tunable BCSRR. Researchers have used such structures to control the beamwidth of the wave by tuning the properties of BCSRR. Frequency tuning arises from changes in the near field coupling. This can be done by shifting the geometry in vertical and horizontal position to vary to impedance. Figure 2.15 shows the frequency tunable BCSRR.

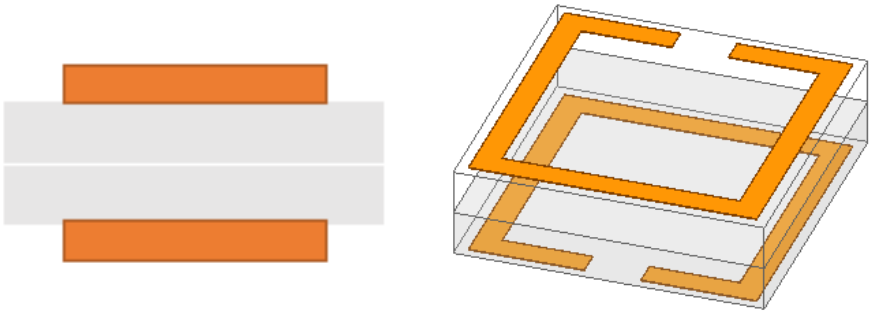

Figure 2.15 Frequency tunable BCSRR

When there are relative slips in the X and Y directions with respect to magnetic and electrical excitations i.e., H perpendicular to BCSRR and k (direction of propagation) perpendicular to BCSRR, respectively. In this section a detailed analysis is discussed [20, 21]. In magnetic excitation the surface currents in both top and bottom layers are in the same direction resulting in the mutual inductance to yield positive sign.

$$L_{total} = L_{self} + L_{mutual}$$

Similarly, the surface charge distribution for magnetic excitation can be seen as positive and negative between both layers when overlapping resulting in significant mutual capacitance. So, the lateral shift (vertical or horizontal) decreases the inductance and capacitance.

For electrical excitation, the surface currents in both top and bottom layers are in the opposite direction resulting in the mutual inductance to yield negative sign.

$$L_{total} = L_{self} - L_{mutual}$$

The surface charge distribution for electrical excitation can be seen. Negative charge overlaps with negative and positive charge overlaps with positive yielding much weaker mutual capacitance. Unlike magnetic excitation shifting is an important factor for electrical excitation. If the shift is horizontal, SRR arrays slide over the arms which charges of the same sign yielding small change in mutual capacitance. However, if the shift is vertical, opposite charges overlap giving more shifts in resonance

frequencies since more change in mutual capacitance.

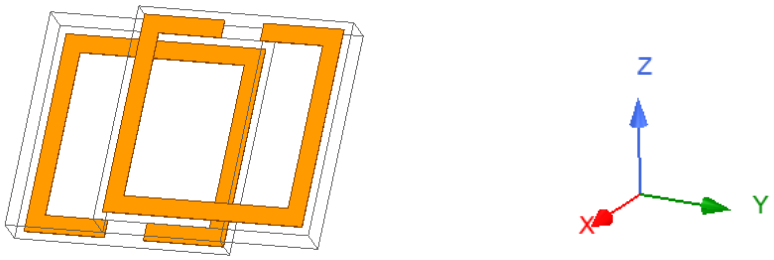

(a)

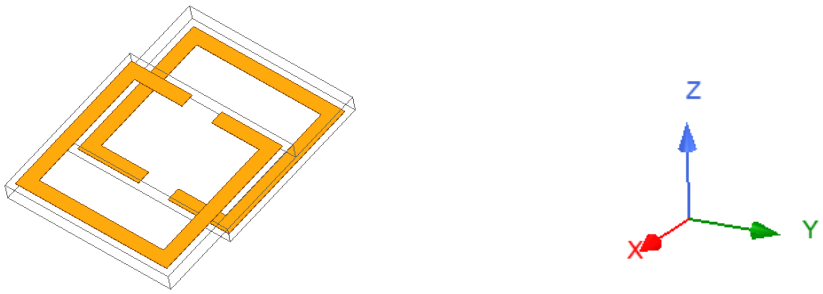

(b)

Figure 2.16 Frequency tunable BCSRR (a) X-direction shift (b) Y direction shift

Figure 2.16 (a) and (b) show the in-plane shift in Y and X directions, respectively. To evaluate the effects of the shifts, the variations were done from 0 mm till 3.5 mm with 0.5 mm step size. The coordinate system is added for the ease of interpretation of the results.

The following equations are related to shift in X- direction [30].

$$C_0'/2 = \epsilon \frac{R_w(R_l - 2x' - gap/2)}{h} + \epsilon \frac{R_w R_l}{\sqrt{h^2 + x'^2}}$$

$$\omega_x = \frac{1}{\sqrt{LC_0/4}} = \frac{1}{\sqrt{L\epsilon R_w\left(\frac{(R_l - 2x' - gap/2)}{h} + \frac{R_l}{\sqrt{h^2 + x'^2}}\right)}}$$

The following equations are related to shift in Y- direction.

$$C_0^{''}/2 = \epsilon\frac{R_w(R_l - 2y')}{h}$$

$$\omega_y = \frac{1}{\sqrt{LC_0/4}} = \frac{1}{\sqrt{\frac{L\epsilon R_w}{2(2R_l - gap/2)}\left(\frac{(R_l - 2y')}{h} + \frac{R_l - gap/2}{\sqrt{h^2 + y'^2}}\right)}}$$

Figure 2.17 (a) and figure 2.18 (b) shows the S paramters from magnetic excitation for Y shift (horizontal displacement).

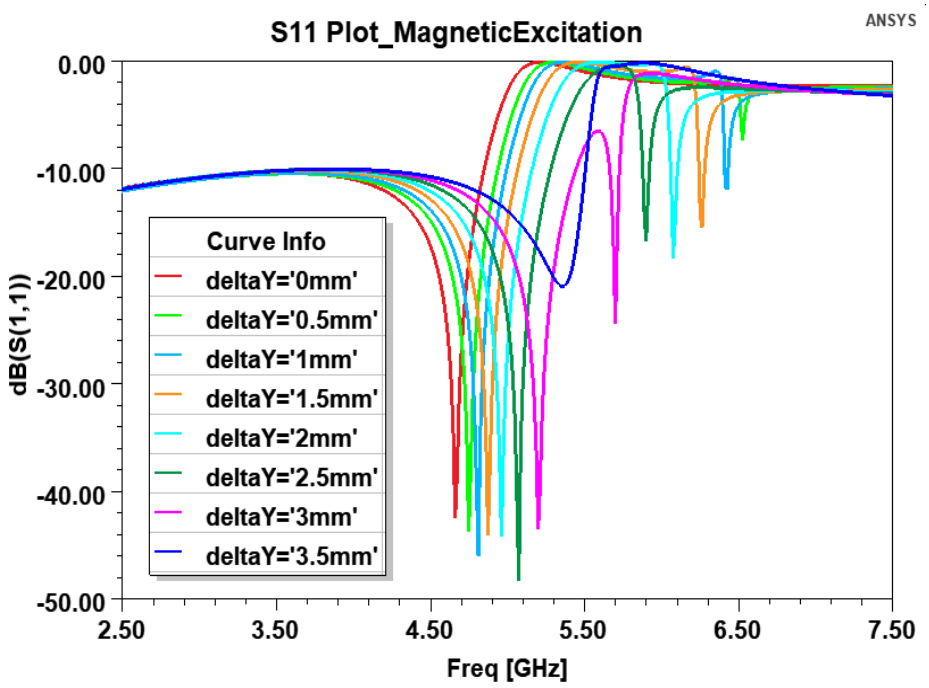

(a)

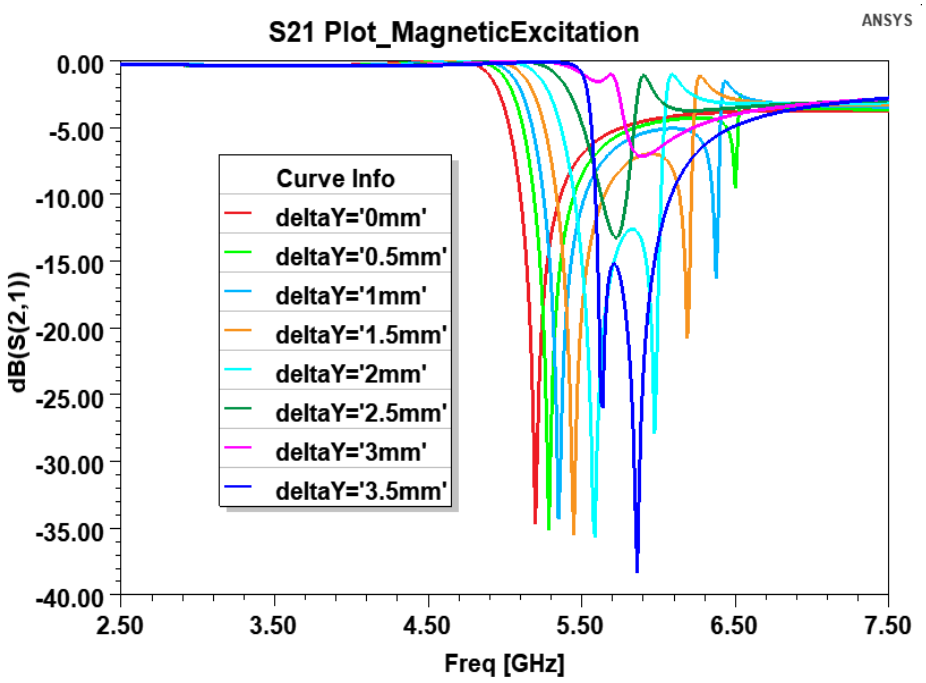

(b)

Figure 2.17 S Parameter plots for tunable BCSRR with magnetic excitation along Y- direction (a) S11 (b) S21

The shift of 600 MHz is seen when the displacement is 0.3 mm i.e. half a unit cell. This happens because of change in the mutual capacitance. Here the mutual inductance effects are too small as compared to the self inductance, so mutual inductance effects are neglected. Similarly the effects capacitance generated from the splits can be neglected because the thickness of copper metallization is very small. Therefore the mutual capacitance and self inductance is responsible for frequency shifts. These structures are used in beamwidth control with partially reflective surfaces which is discussed in chapter 3.

CHAPTER 3

ANTENNA CONSIDERATIONS AND USE WITH PARTIALLY REFLECTIVE SURFACES

Many techniques have been used for enhancement of the gain, bandwidth, efficiency, and directivity of the antennas. The addition of a superstrate layer above the antenna has been observed to improve the gain and directivity of the antenna. Furthermore, superstrate layers are often used to protect the antenna from environmental hazards especially when used in aircrafts and missiles. This chapter discuss the design and formulation of patch antenna and superstrates made using BCSRR also known as partially reflective surfaces.

3.1 Patch Antenna

Patch antennas were first discussed in 1950's. A microstrip patch antenna is a piece of conducting material such as copper milled on top side of the substrate and the bottom layer is the ground plane like a microstrip. The wavelength of radiation is determined by the length of the patch. The figure 3.1 shows the inset fed microstrip rectangular patch antenna, which is excited by using microstrip transmission line.

Patch antennas are very cost effective and are easier to fabricate. Usually, the patch antennas are narrow band antennas. The figure 3.1 shows the patch antenna along with the fringing fields which helps explain how an antenna radiates. The current and voltage distribution along the patch can be explained by comparing the patch antenna with open circuited transmission line. With a reflection coefficient of an open circuit is calculated as -1, this indicated that the voltage is maximum at the end of the antenna and current is minimum. Whereas the voltage is minimum at the center and current is

maximum. Typically, the length of the antenna is designed to be half a wavelength, approximately, the voltage is maximum at the front and back end of the antenna (the y side in this diagram) and the current is minimum, this results in creation of fringing fields as shown in the figure 3.1 [32]. The patch antenna radiates through two slots which are located on the y axis, so electric fields is on the y axis and the magnitude of the field is same in front end or the rear end of the patch. Since the fields are similar in magnitude, they reinforce each other. Ground plane is usually added to suppress the back radiations from the patch, and it cancels out the current distribution in the patch by producing opposite current distribution. This result in producing no back radiation.

For designing the microstrip patch antenna certain design equations are to be considered. Here the antenna is designed for 5GHz resonant frequency. Rogers Duroid 5880 is used as the substrate with $\epsilon_r = 2.2$ and $\tan\delta = 0.0004$.

Wavelength is calculated as $\lambda = \frac{c}{f}$

where c is the velocity of light and f is the resonant frequency

Guided Wavelength $\lambda_g = \frac{\lambda}{\sqrt{\epsilon_{eff}}}$

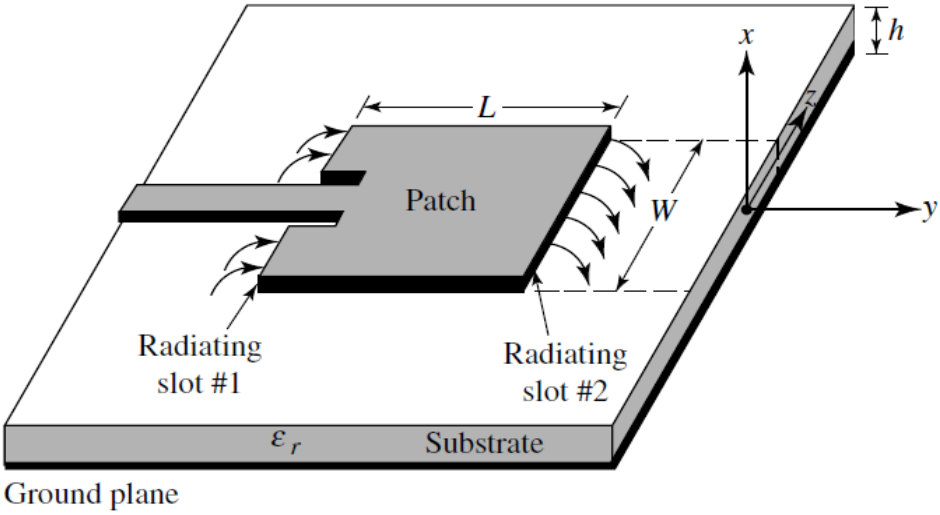

Fig. 3.1. Rectangular microstrip antenna [32]

As discussed in the previous section fringing field has lot of influence on the performance of the patch antenna. Since the voltage is minimum at the center of patch, the electric field is approximately zero. Width of the patch is responsible for radiation; it also controls the input impedance and bandwidth of the patch. Variation of width results in impedance matching as width and input impedance have an inverse relationship, it is also responsible for bandwidth control. Substrate thickness and dimensions of the patch controls the amount of the fringing field generated. Greater the thickness of the substrate, the more fringing fields are produced. Fringing fields are responsible for the antenna to radiate and it makes the antenna look electrically larger as compared to its physical dimensions. These fringing fields travel both in substrate and in the air. This phenomenon introduces an effective dielectric constant, denoted by ϵ_{eff}. The effective dielectric constant ϵ_{eff} takes in account both the fringing and the wave propagation in the transmission line [32].

Effective permittivity

$$\epsilon_{eff} = \frac{\epsilon_r + 1}{2} + \frac{\epsilon_r - 1}{2}\left[1 + 12\frac{h}{W}\right]^{-\frac{1}{2}}$$

Width of the patch is calculated as follows.

$$W = \frac{c}{2f\sqrt{\frac{\epsilon_r + 1}{2}}}$$

Length of the patch is given by,

$$L = L_{eff} - 2\Delta L$$

$$L_{eff} = \frac{c}{2f\sqrt{\epsilon_{eff}}}$$

ΔL is the amount of size increased of the patch antenna because of the fringing fields. This length can be calculated as follows.

$$\Delta L = 0.412h\frac{\left(\epsilon_{eff}+0.3\right)\left(\frac{W}{h}+0.264\right)}{\left(\epsilon_{eff}+0.258\right)\left(\frac{W}{h}+0.8\right)}$$

Microstrip feed line dimensions for 50Ω impedance matching can be calculated as follows.

$$L_{feed} = \frac{\lambda_g}{4}$$

$$W_{feed} = \frac{L_{feed}}{2}$$

Inset width is usually taken to be 1mm.

Inset height:

$$I_h = \frac{6h}{2}$$

Symbol	***Parameter***	***Value (mm)***
S_l	Substrate Length	60
S_w	Substrate Width	99
P_l	Patch Length	19.8282
P_w	Patch Width	23.7171
F_l	Feed Length	30
F_w	Feed Width	5.4233
I_l	Inset Length	7.1461
I_w	Inset Width	0.5

Table 3.1: Patch antenna dimensions

The normalized radiation patter is given by.

$$E_\theta = \frac{sin\left(\frac{kW\ sin\theta sin\phi}{2}\right)}{\frac{kW\sin\theta sin\phi}{2}} cos\left(\frac{kL}{2} sin\theta cos\phi\right) cos\phi$$

$$E_\theta = -\frac{sin\left(\frac{kW\ sin\theta sin\phi}{2}\right)}{\frac{kW\sin\theta sin\phi}{2}} cos\left(\frac{kL}{2} sin\theta cos\phi\right) cos\theta sin\phi$$

Where $k = \frac{2\pi}{\lambda}$

And magnitude of field

$$f(\theta, \phi) = \sqrt{E_\theta^2 + E_\phi^2}$$

Figure 3.2 shows the designed microstrip patch antenna designed on rogers 5880 substrate. Figure 3.3 shows the S parameters plot, as seen impedance matching is pretty good for the designed structure. Figure 3.4 show the radiation pattern plots for the patch. The blue curve is for the H principal plane and the red curve is for the E principal plane. It can be observed that the gain is 9.0622 dB.

Note, although the focus of this dissertation is on millimeter wave beamforming, all the simulations performed are for 5 GHz frequency. This was done with the hope to build structures at 5GHz to experimentally evaluate the beamforming capability with actual devices before moving into experiments at millimeter-wave frequencies. These simulation results obtained at 5 GHz are expected to scale to higher frequencies with appropriate considerations for material electrical behavior effects.

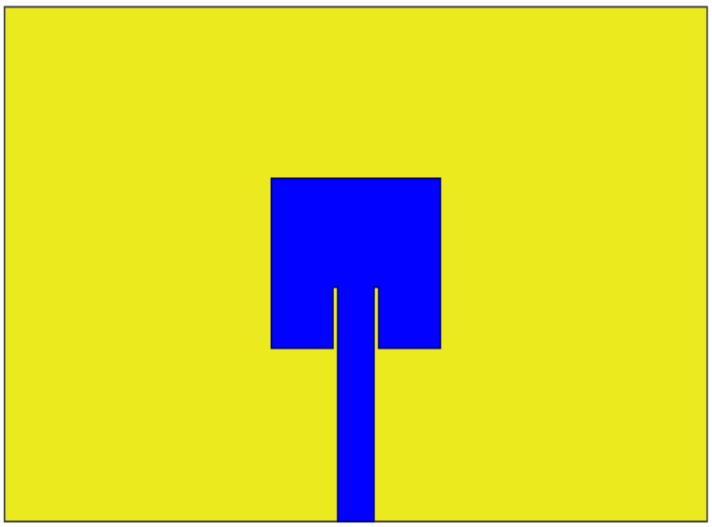

Figure 3.2 Microstip patch antenna

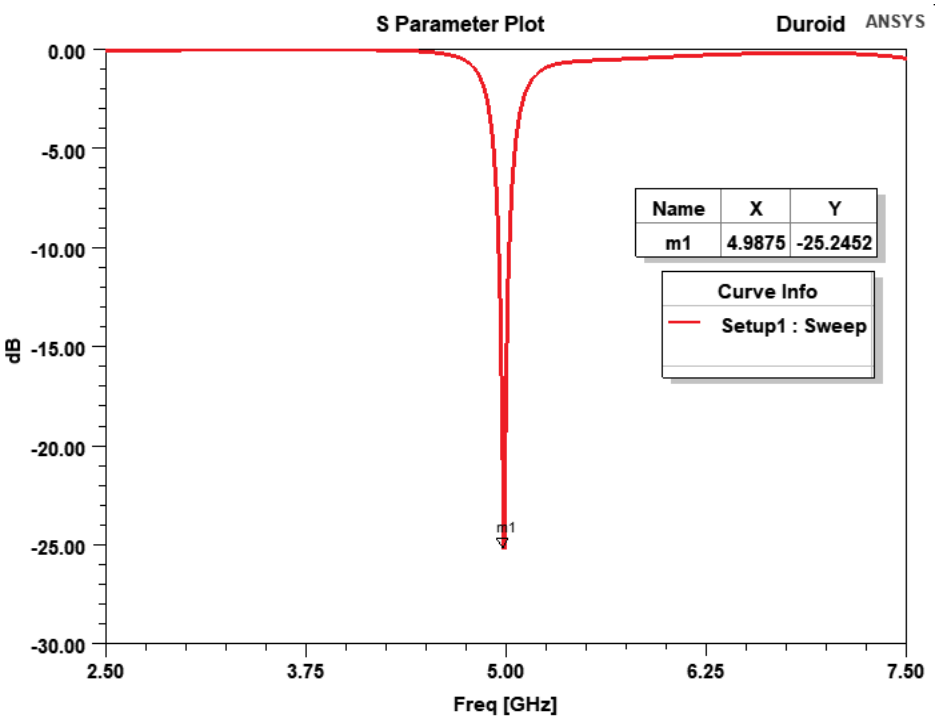

Figure 3.3 S parameters of microstip patch antenna

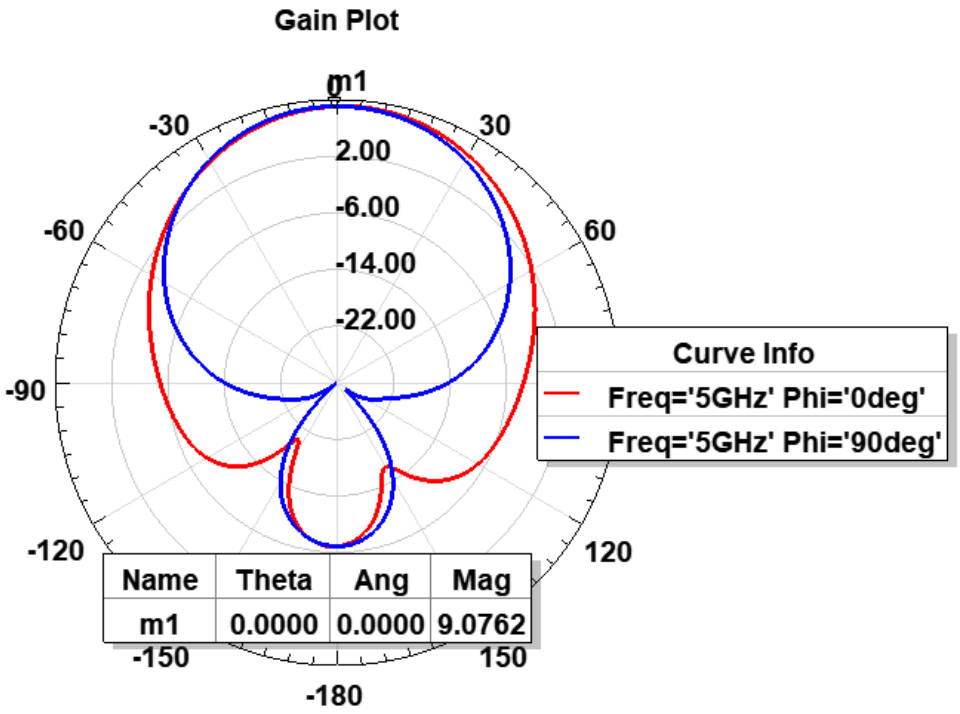

Figure 3.4 Gain plot of microstip patch antenna

3.2 Partially Reflective Surface

In this section, the intuitive theory, and concepts of PRS antennas is presented. Various properties of partially reflective surface antennas are discussed. This concept was introduced for the first time in 1955 by Giswalt Von Trentini [76]. A typical structure of partially reflective surface is shown in figure 3.5. It consists of a PRS set at a distance d above the PEC (perfect electric conductor) ground plane and a source antenna. Microstrip patch antenna is selected to be the radiating source. The electromagnetic waves radiated from the patch are incident on the partially reflective surface, some of the waves are reflected to the ground plane and some of them are transmitted to the aperture. As the PRS and ground plane are assumed to be of infinite sizes this process is assumed to repeat endlessly in theory. Because of this process, infinite number transmitted, and reflected wave interfere, which contributes to form a highly directive pencil beam [67].

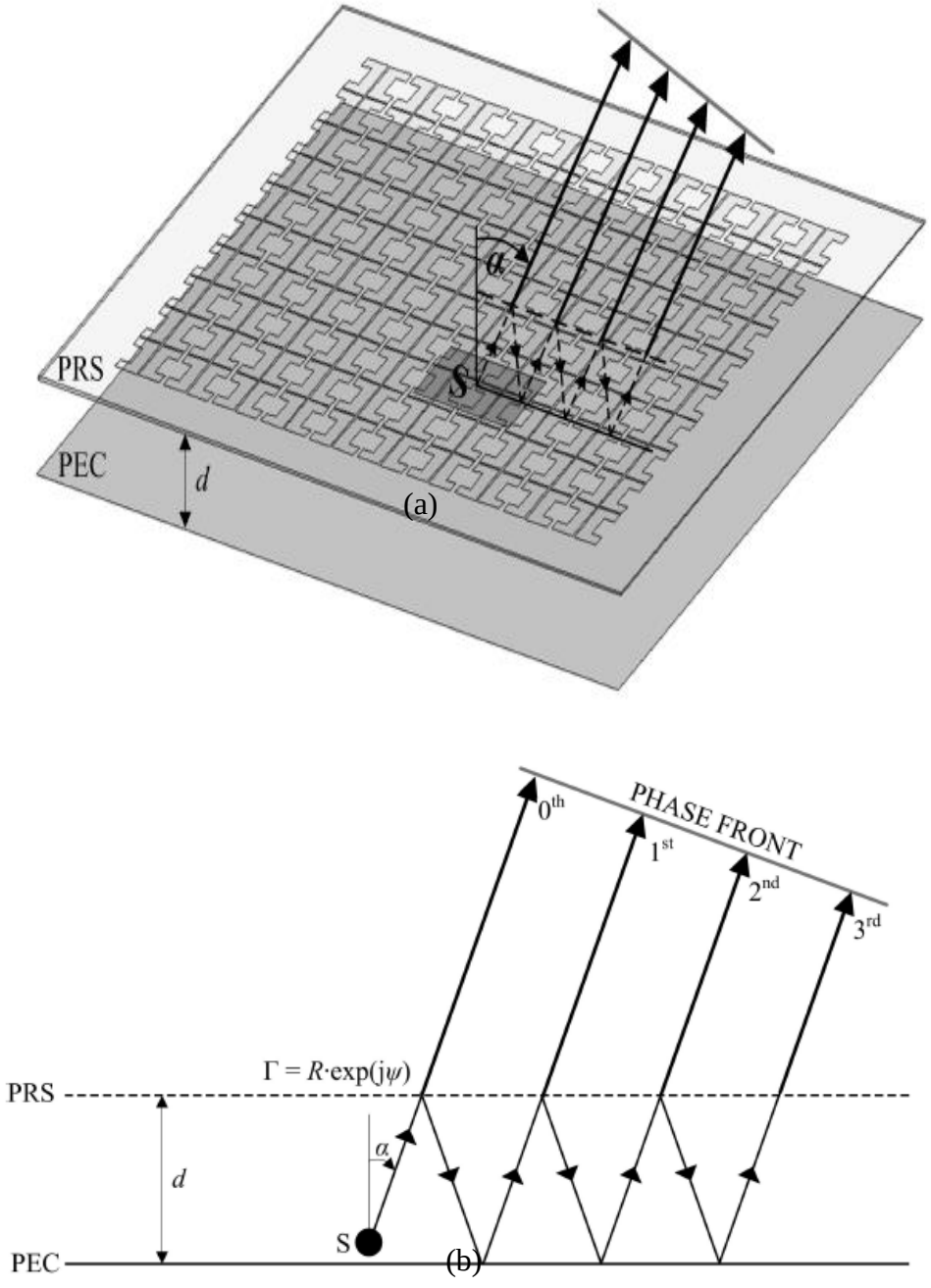

Figure 3.5 Typical PRS Antenna (1) 3D- view, (b) Lateral view [67]

The radiation pattern of the source is given by,

$$E_0 \cdot F(\alpha)$$

And the PRS reflection coefficient written for a plane wave,

$$\Gamma = Re^{j\psi}$$

R is the magnitude and ψ is phase are usually dependent on the frequency, polarization of the wave and incidence angle.

$$R = R(f, \alpha, pol)$$

$$\psi = \psi(f, \alpha, pol)$$

In this analysis it is assumed that when the electromagnetic wave is radiated from the source it will be a plane wave. PRS is assumed to be lossless. The relative amplitude transmission of nth referent wave through PRS is given by.

$$R^n\sqrt{1-R^2}$$

Phase shift δ of each adjacent wave, due to reflections from the PRS and PEC is given by

$$\delta = -\frac{4\pi d}{\lambda} \cdot \cos(\alpha) - \pi + \psi$$

Where λ is the wavelength of free space. The first part is the difference between path lengths and $-\pi$ is due to the reflections from ground plane, and ψ is the reflections from PRS. Similarly, nth phase shift is given by,

$$\delta_n = n \cdot \delta = n \cdot \left(-\frac{4\pi d}{\lambda} . \cos(\alpha) - \pi + \psi\right)$$

Therefore, the radiation pattern of the source becomes,

$$E(\alpha) = E_0 \cdot F(\alpha) \cdot \sum_{n=0}^{\infty} R^n \cdot \sqrt{1-R^2} e^{jn\delta}$$

The part $\sum_{n=0}^{\infty} R^n e^{jn\delta}$ forms a geometric series. Because PRS is a passive device, R<1 and above equation can be written as

$$E(\alpha) = E_0 \cdot F(\alpha) \cdot \frac{\sqrt{1-R^2}}{1-Re^{j\delta}}$$

The power pattern is given by

$$S(\alpha) = \frac{|E(\alpha)|^2}{2\eta}$$

By combining,

$$S(\alpha) = \frac{|E_0 \cdot F(\alpha)|^2}{2\eta} \cdot \frac{1 - R^2}{1 + R^2 - 2R \cdot \cos\left(\psi - \pi - \frac{4\pi d}{\lambda} . \cos(\alpha)\right)}$$

where $\eta = 120\pi\ \Omega$ is the intrinsic impedance of free space. The power pattern of the antenna with PRS is given by the above equation, that is similar to the power pattern of the source antenna and the multiplying factor called the extra directivity D_e.

Extra directivity is given by,

$$D_e(\alpha) = \frac{1 - R^2}{1 + R^2 - 2R \cdot \cos\left(\psi - \pi - \frac{4\pi d}{\lambda} . \cos(\alpha)\right)}$$

To achieve the phase condition at $\alpha = 0$, PRS is placed at a carefully formulated distance d

$$\psi(\alpha = 0) - \pi - \frac{4\pi d}{\lambda} = 2N\pi$$

$$D_e(\alpha = 0) = \frac{1 + R}{1 - R}$$

Usually, $d \approx \frac{\lambda}{2}$ is chosen to get the high directivity.

Figure 3.6 shows the arrangement of partially reflective surface using broadside coupled split ring resonator with the gain plots. The blue curve is for the H principal plane and the red curve is for the E principal plane. It can be observed that the gain is 12.3733 dB. Comparing figures 3.4 and 3.7 it can be observed that the gain has been increased 25%.

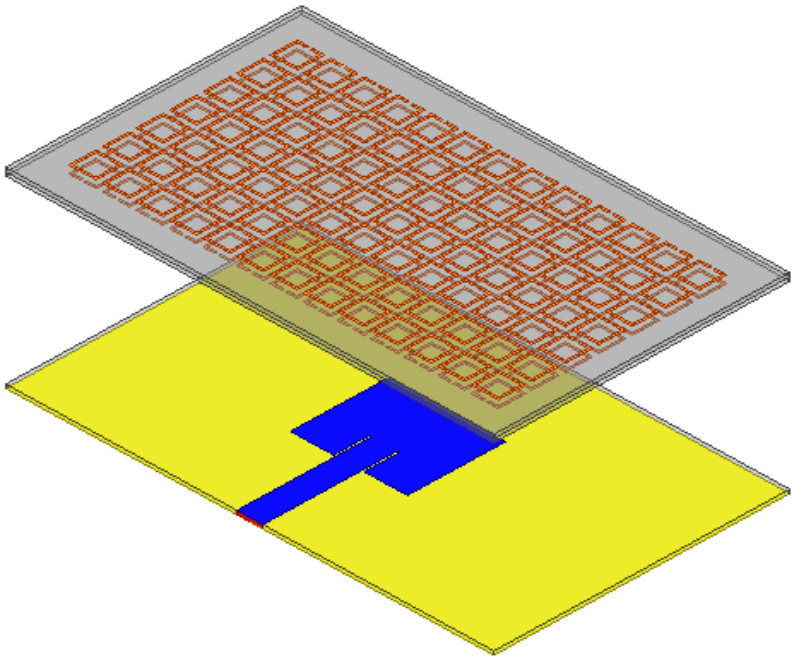

Figure 3.6 Patch antenna with partially reflective surface using BCSRR.

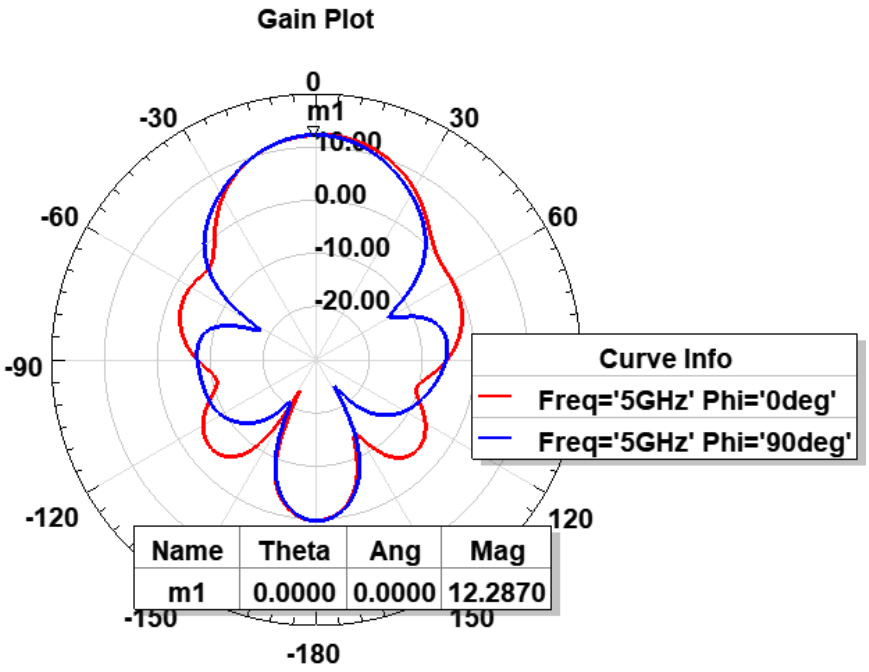

Figure 3.7 Gain Plot for Patch antenna with partially reflective surface using BCSRR for E and H principal plane

If the PRS reflectivity is high, the repeatedly reflected waves shown in Figure 3.7, decay quite slowly. This means that many rays with high amplitudes interfere in some direction α, which implies the low frequency bandwidth, as the relative phase of the waves is dependent on the frequency. On the contrary, when the PRS reflectivity is low, only a few starting successive waves matter. The amplitudes of the rest of the waves are negligible due to the low reflectivity. Thus, the interference is less intense and the extra directivity changes slower with respect to the frequency.

Figure 3.8 shows the arrangement of sparsely spaced PRS along with patch antenna. It is clearly observed from figure 3.9 that the gain has decreased for sparsely spaced PRS when compared to highly reflective PRS. The blue curve is for the H principal plane and the red curve is for the E principal plane. It can be observed that the gain is 10.4998 dB. The beamwidth obtained with the higher reflectivity PRS is narrower and changes more in the given frequency bandwidth, compared to the pattern obtained with the lower reflectivity PRS.

Figure 3.10 shows the S parameter plot of patch antenna with no PRS, sparsely spaced PRS and highly reflective PRS. It can be seen that the impedance matching is pretty good for patch antenna with no PRS and sparsely spaced PRS, whereas there is impedance mismatch for high reflective PRS. This happens because of high reflections from the PRS which reduces the reflection coefficient.

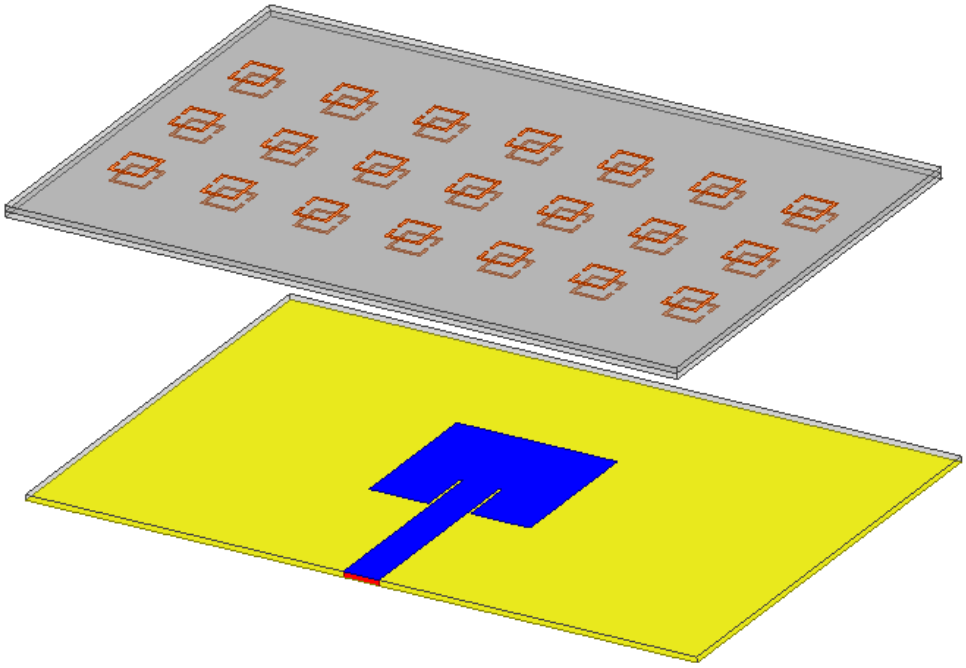

Figure 3.8 Patch antenna with sparsely spaced PRS using BCSRR.

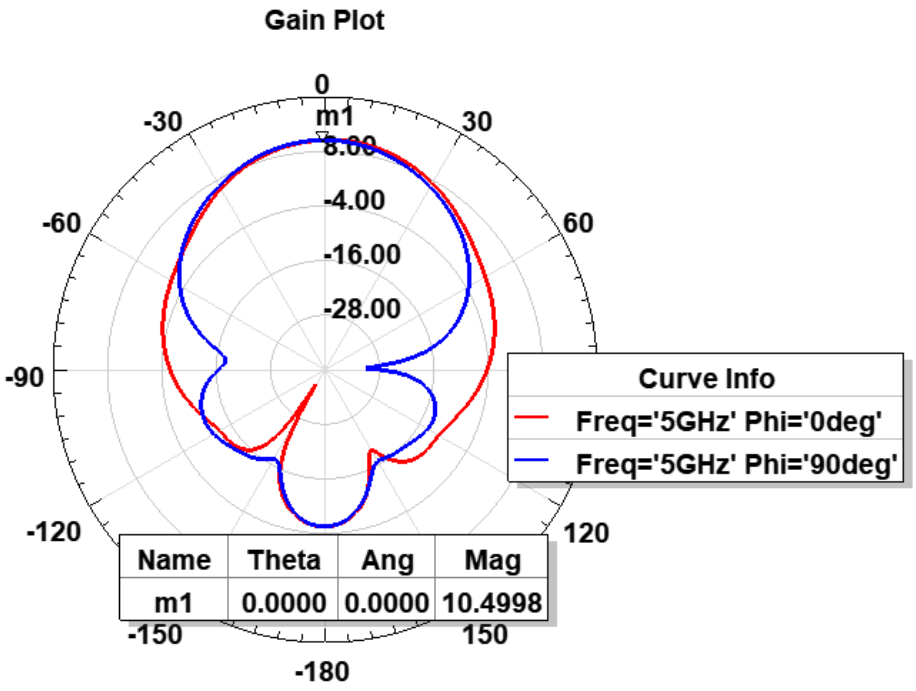

Figure 3.9 Gain Plot for patch antenna with sparsely spaced PRS using BCSRR E and H principal plane

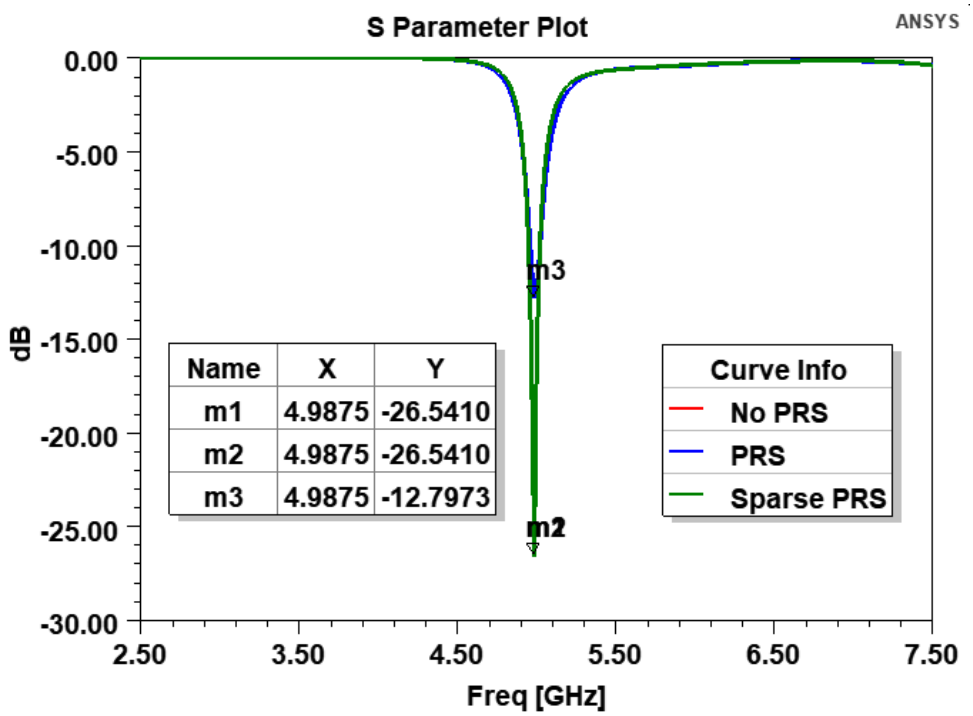

Figure 3.10 S Parameter plot comparing plots for No PRS, with PRS and with sparsely spaced PRS

CHAPTER 4

WAVE PROPAGATION MECHANISMS AND CONSIDERATIONS IN BEAMSTEERING

4.1 Beamsteering

Beamsteering is defined as changing the direction of the main beam in a radiation pattern. Beamsteering usually happens whenever there is some phase shift between the radiating beams of individual elements in an array. Before the concept of general beamforming was introduced, researchers used phased array antennas to steer the beam by adding appropriate amount of phase shifts among different elements. Researchers have explored many techniques in the field of beam steerable antennas. For many types of applications, producing multiple highly directive multiple beams is critical. Highly directive beams can result in low interference, and low transmit power requirement resulting in improved systems performance. In this work, different structures are evaluated using patch antennas, since it has linear polarization and is straightforward to construct and compactly integrated with other system components. In this chapter some of the beamsteering techniques using a scheme of dielectric wedges, and partially reflective surfaces has been evaluated and the scheme of vertical split ring resonators have been proposed.

4.2 Wave Propagation Mechanisms

Beamsteering and beamforming can be achieved by a combination of reflection, refraction and diffraction. For initial assumptions in deciding on geometries to investigate geometrical optics approximations (GO) are used. However, GO assumes object dimensions larger than a few wavelengths. Snell's law gives a crude approximation of the beamsteering angles, but it does not give

any approximation about the radiation pattern and power levels. In this section a simulation is provided to demonstrate the effect of deviation from GO behavior for objects smaller than a wavelength.

The simulations for all the finite size structures are carried out by implementing absorbing boundary conditions. From figure 4.1 it can be seen that when the dielectric wedge of dimension 10 times the wavelength is illuminated by an incident plane wave; a clear refraction effect can be observed. The wave bends and beamsteering takes place. Whereas when the wavefront dimension of the wave incident on the wedge is around a wavelength structure as seen in figure 4.2; i.e., the wave bending (refraction) as well as spreading out (diffraction) effects are both observed.

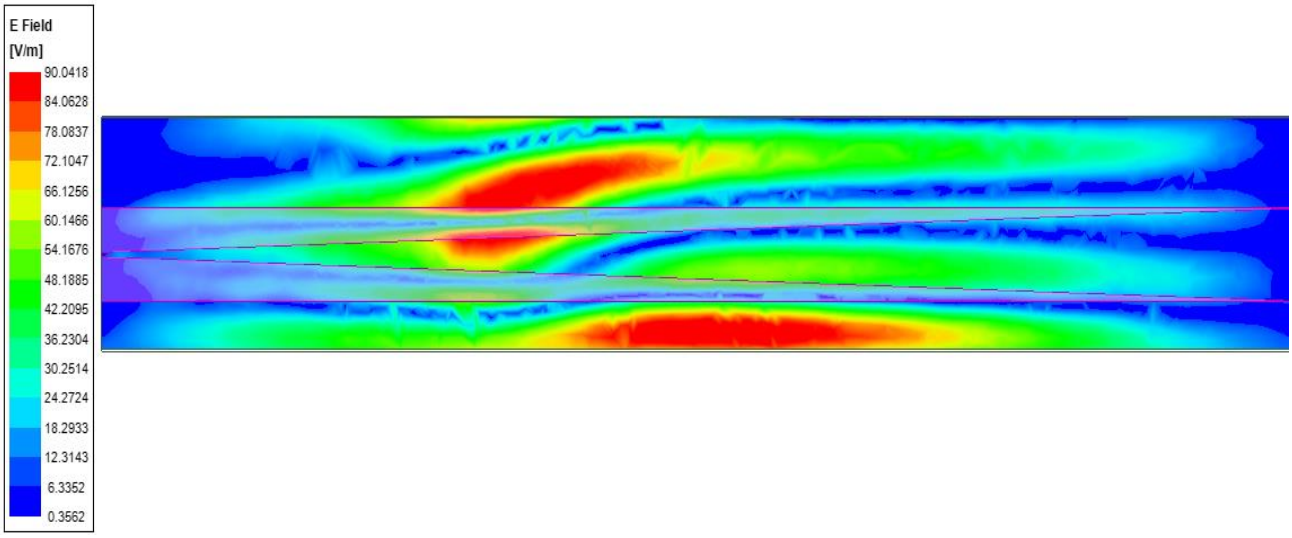

Figure 4.1 Wedge Dimensions 10 x wavelength (wave bending clearly seen in and around the red regions of the incident and outgoing/ refracted waves)

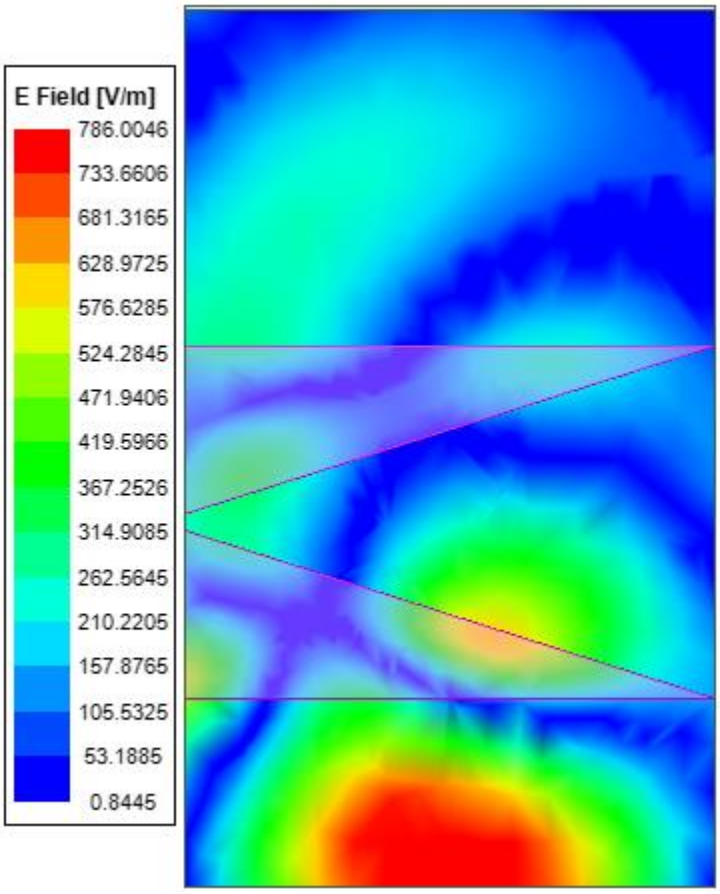

Figure 4.2 Wedge Dimensions 1 x wavelength

4.3 Beamsteering using Dielectric Wedges.

To achieve the phase shift using a conventional array of patches each element in the array is excited individually using the probe feeding. The phase delay for such antennas is calculated using the formulations from array theory. The array theory states that to steer a beam by an angle θ_0, the center-to-center spacing d in an antenna array can be kept approximately $\lambda_0/2$ depending upon the performance and design of the antenna, where $\lambda_0$is the free space wavelength and the progressive increase in phase delay or δ is given by,

$$\delta = \frac{2\pi}{\lambda_0} d \sin(\theta_0)$$

Studies have been done to understand the behavior of wave propagation through dielectric materials.

[78]. From basic electromagnetics theory it is well known that a wave propagates inside a dielectric slower in time than in free space because of the material interactions(dielectric constant) such that the wavelength of the wave is less than that in the free space, which is expressed as $\lambda_g = \frac{\lambda_0}{\sqrt{\epsilon_r}}$, where λ_0 is the wavelength of free space, $\lambda_g$is the guided wavelength and ϵ_r is the relative permittivity of the dielectric. For steady state cases this can be interpreted as an increase in electrical length, or phase delay. This phase-delay can be varied according to the needs either by changing the lengths and widths of the structure or by using different dielectric constants of fixed length or both.

The use of dielectric wedges has been studied to understand and demonstrate the beamsteering concept. As seen from figure 4.3 a single wedge can cause some differential phase delay across the wavefront whenever the wave propagates through the wedge which causes some beam deflection. To obtain dynamic beamsteering the concept of Risley Prism can be realized with this structure. The Risley Prism working principle states that the prisms are to be placed in the reactive near field of antennas so that the beam incident on the lens is undistorted and there are no spillovers. Two wedges are placed at top of the source where each wedge accounts for beam tilts away from the broadside direction [78].

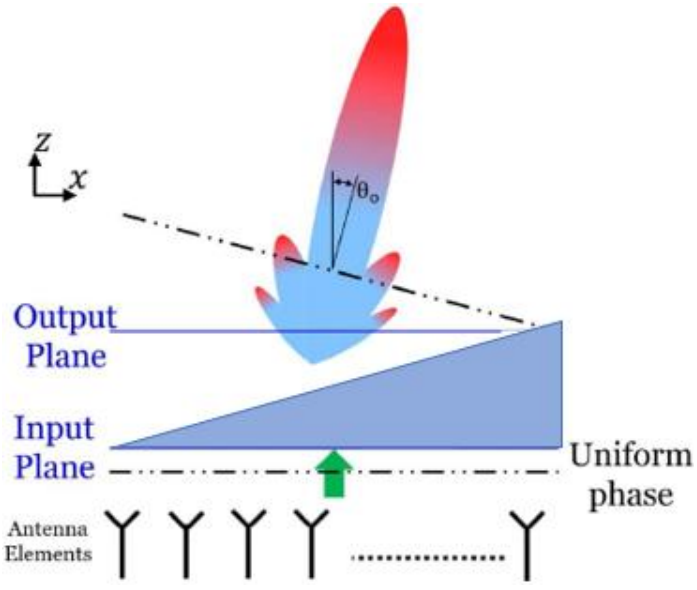

Figure 4.3 Placement of wedge for linear phase progression [78]

These two wedges can be rotated in clockwise or anticlockwise direction independently or simultaneously to achieve beamsteering. The orientation of the two wedges define the broadside or endfire radiation patterns of the antenna.

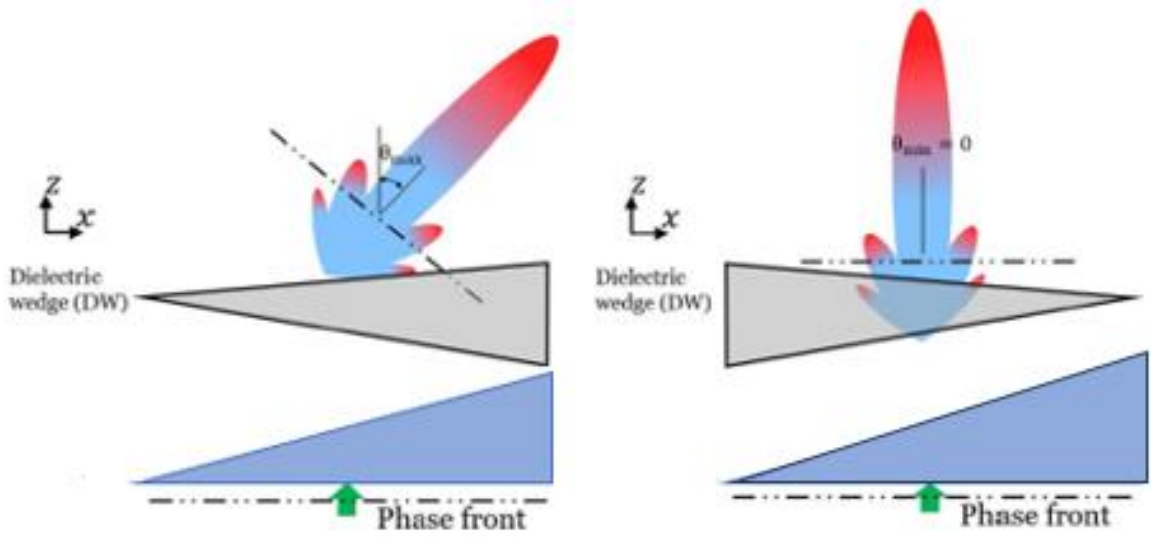

Figure 4.4 Wedge placement for different beamsteering [78]

To dynamically obtain the beamsteering, the beam angles $\theta_{min}\ and\ \theta_{max}$ are studied (figure 4.5). Two opening angles $\theta_1 and\ \theta_2$ of the dielectric wedges are optimized for the desired system performance. Here to demonstrate beamsteering we took angle θ_2 as 0 degrees. The ray tracing diagram of the two dielectric wedges for two different orientations is shown in figure 4.3.

$$\theta_{min} = \sin^{-1}\left(\sqrt{\epsilon_r}\sin\ (\sin^{-1}\left(\left(\frac{1}{\sqrt{\epsilon_r}}\sin\ (\theta_1 + \theta_p)\right) - \theta_1 - \theta_2\right)\right)$$

$$\theta_{max} = \sin^{1}\left(\sqrt{\epsilon_r}\sin\left(\theta_2 - \theta_p\right)\right)$$

where the propagation angle θ_p is of the phase front with reference to the normal of the antenna system.

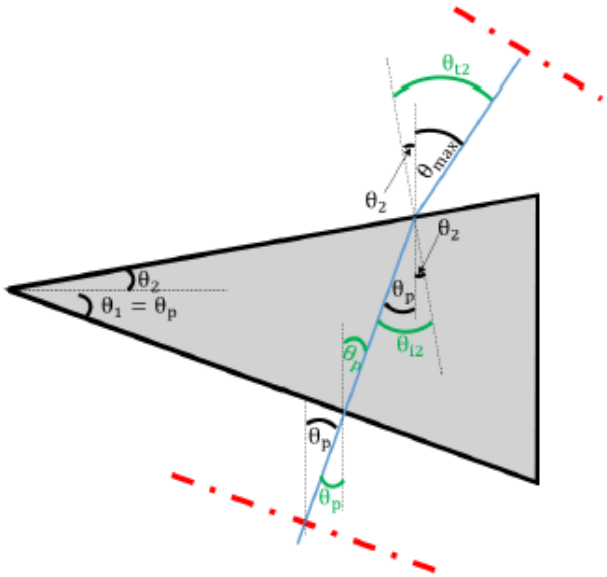

(a)

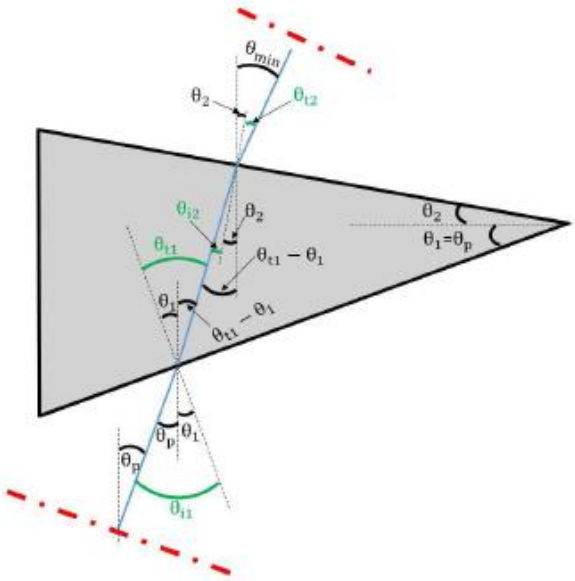

(b)

Figure 4.5 Dielectric wedge flaring angles for (a) Maximum, and (b) Minimum beam tilt angles [78]

Figure 4.5 shows the directional of incoming and outgoing waves with blue line. To simplify the

design, the first opening angle of the wedge or θ_1 is set equal to the beam tilt angle introduced by $\theta_1 = \theta_p = 8.3151°$. These calculations are done to make sure that the waves propagating out of the first dielectric is perfectly aligned to the input surface of the second wedge.

This method is the easiest and affordable way to achieve beamsteering. The pair of dielectric wedges are placed in the near field of the patch antenna. The arrangement of wedges can be done in two ways as shown in figure 2.3. When the face of the wedge is parallel to the antenna aperture the reflection from the first surface is incident normal to the antenna aperture and is mainly absorbed by the system whereas when the slanting face is facing the antenna aperture the reflections from the wedge are scattered which results in more sidelobes and impedance mismatch [75]. Figure 4.6 shows the arrangement of wedges selected for this investigation and the vector fields representation for beam steering. Here the wedges are placed on top of the antenna, 5 mm away.

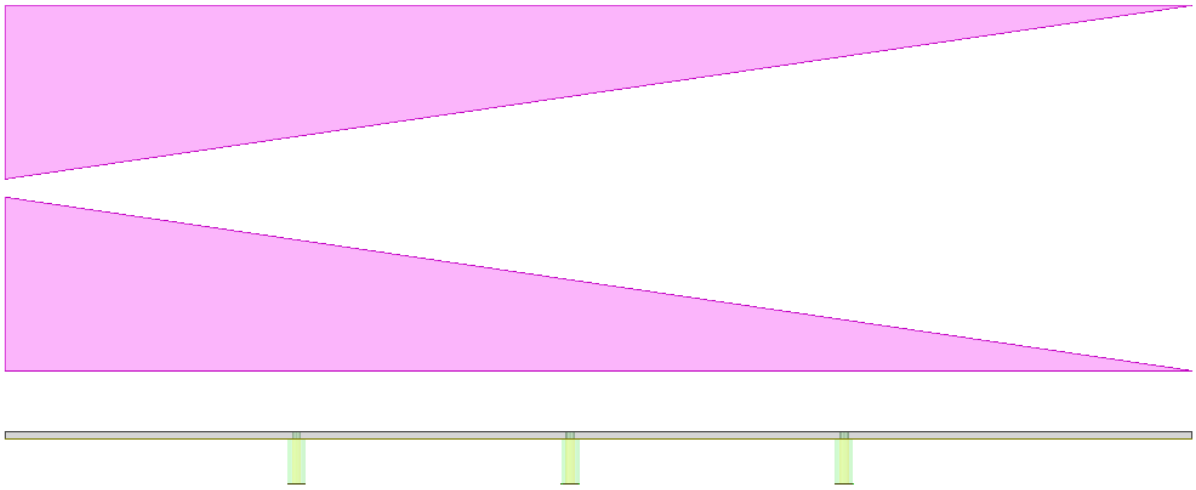

Figure 4.6 Placement of horizontal wedge

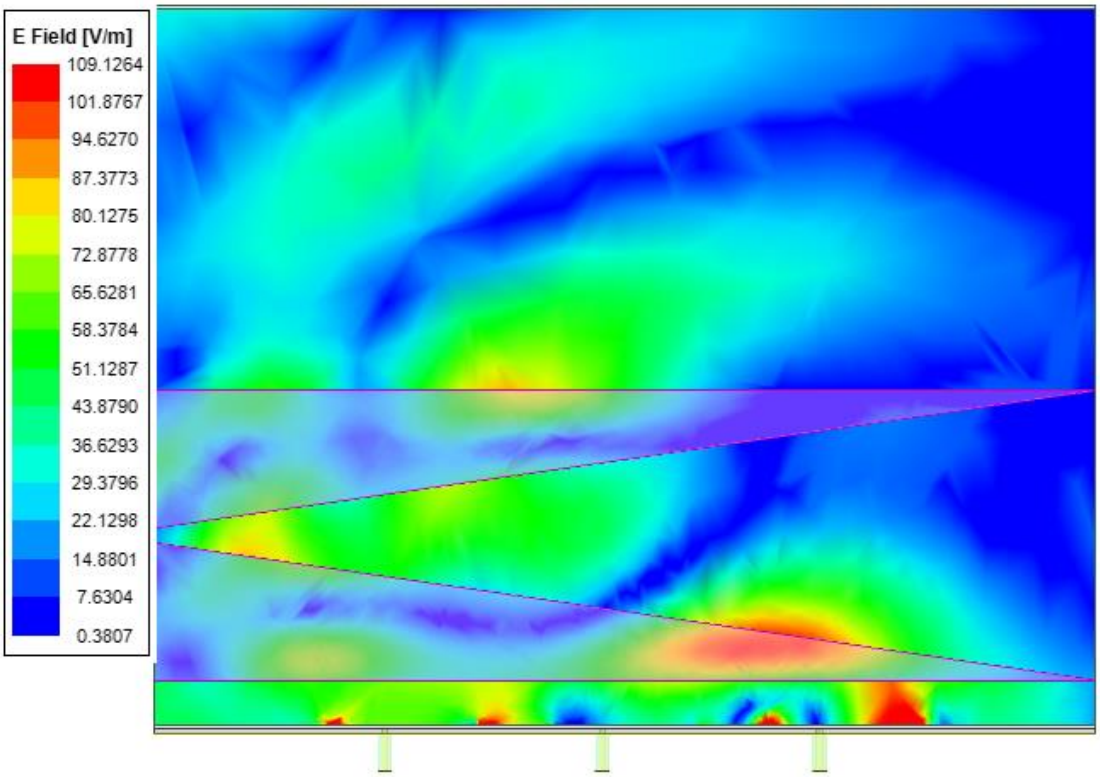

Figure 4.7 Radiation E Field plot of horizontal wedge

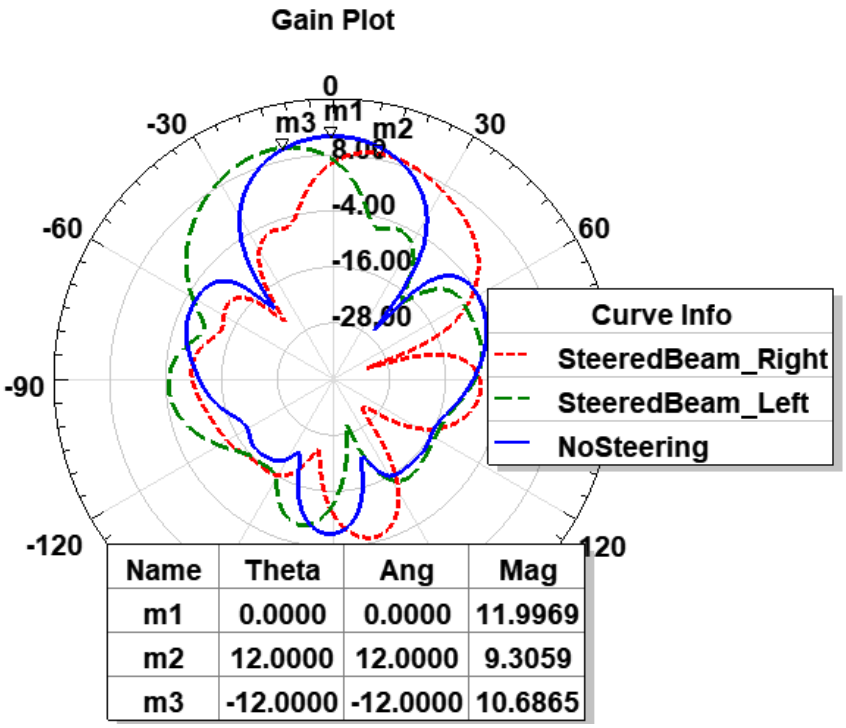

Figure 4.8 Gain plot comparing beamsteering angle of horizontal wedge

Figure 4.7 shows the electric fields flowing through the wedge, here the dielectric constant of the wedge is taken to be 5.5 and the thickness is 18 mm. The gain plots for E principal plane in figure 4.8 shows the beamsteering for left, right and no steering using dielectric wedge. Consider the plane wave incident from the antenna at an arbitrary direction of (θ', ϕ') having an amplitude of $F_a = (\alpha', \beta')$. As it passes through the wedge it experiences changes in both amplitude and phase resulting in phase tilts of e^{-jgx} and e^{jhy} in x and y direction respectively and amplitude changes by the factor of τ. This plane wave gets reradiated from the face of the wedge [79].

$$F(\alpha, \beta) = \frac{\tau}{\lambda^2} F_a(\alpha', \beta') \iint_S exp(jk\ sin\theta \left(x\left(cos\phi - \frac{g}{k} sin\theta\right) + y\left(sin\phi - \frac{h}{k} sin\theta\right)\right) dx\ dy$$

$$\text{Let} \quad cos\phi - \frac{g}{k} sin\theta = \rho cos\phi"$$

$$sin\phi - \frac{h}{k} sin\theta = \rho sin\phi"$$

$$\rho sin\theta = sin\theta"$$

And s = surface defined by the aperture

Substituting these values in above equation

$$F(\alpha, \beta) = \frac{\tau}{\lambda^2} F_a(\alpha', \beta') \iint_S exp\left(jk.\rho.sin\theta(xcos\phi"+ysin\phi")\right) dx\ dy$$

$$F(\alpha, \beta) = \frac{\tau}{\lambda^2} F_a(\alpha', \beta') \iint_S exp\left(jksin\phi"(xcos\phi"+ysin\phi")\right) dx\ dy$$

$$F(\alpha, \beta) = \frac{\tau}{\lambda^2} F_a\left(\alpha", \beta"\right).F_W(\alpha", \beta")$$

Where $\alpha = \sin\theta" cos\phi"$ and $\beta = sin\theta" cos\phi"$

This equation represents the contribution of plane wave $F_a(\alpha', \beta')$ from the antenna to the overall radiation pattern. $F_W(\alpha^{"}, \beta^{"})$ corresponds to the steered pattern from the wedge aperture illuminated from the plane wave.

4.4.1 Beamsteering using the PRS Layers.

As discussed by Attia in [65], displacement of superstrate can cause beam deflection. Since the microstrip patch antenna radiates along two slots, the displacement of superstrate can be done along E principal plane and H principal plane such that it will cover only one slot which will create phase delay in the antenna. To get an intuitive understanding, consider that the beams radiated from the uncovered slot will reach the far field faster than the ones from covered slot. This will create phase shift between the beams resulting in beam deflection in other words beam steering. The phase delay from the covered slot depends on the thickness and refractive index of the superstate. The higher the thickness and dielectric constant, the more the beam steering and vice versa.

Figure. 4.9 shows the patch antenna along with the PRS displaced in E principal plane, noting the slot along the microstrip transmission line is covered by using a partial superstrate; this will create phase delay between the beams emitted from the two slots thereby creating phase imbalance. To get the clear understanding figure 4.10 shows the isometric view of the patch antenna and PRS layer place at distance d from the patch antenna. This type of placement acts as 2x1 phase array antenna placed side by side as seen in figure 4.15. This is discussed in more details in section 4.4.2. The beam steering can be controlled by adjusting the thickness and refractive index of the partially reflective surfaces. Here the patch antenna as well as the BCSRR are modeled on Rogers 5880 with dielectric constant of 2.2 and the height of 0.8 mm to operate at 5 GHz. The size of the ground plane is taken as 99 mm which is approximately $1.5 * \lambda$ The PRS layer is placed at 39 mm above the ground plane.

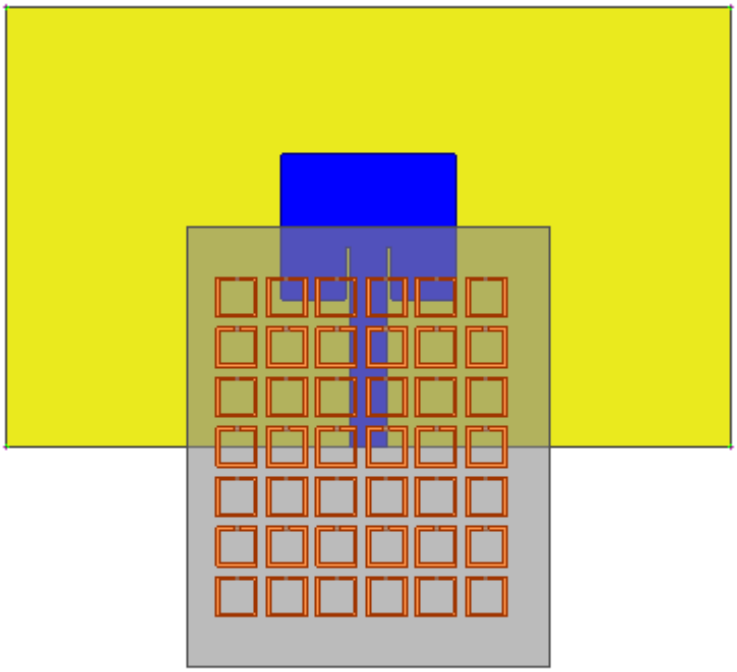

Figure 4.9 Antenna structure with PRS for E plane positive angle steering

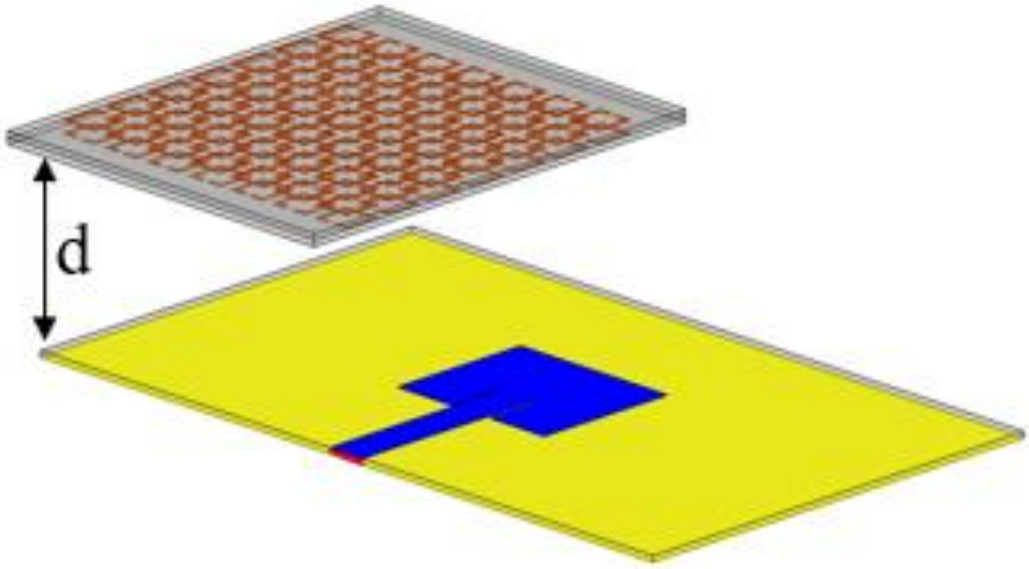

Figure 4.10 3D Arrangement of BCSRR and patch antenna showing 3D view

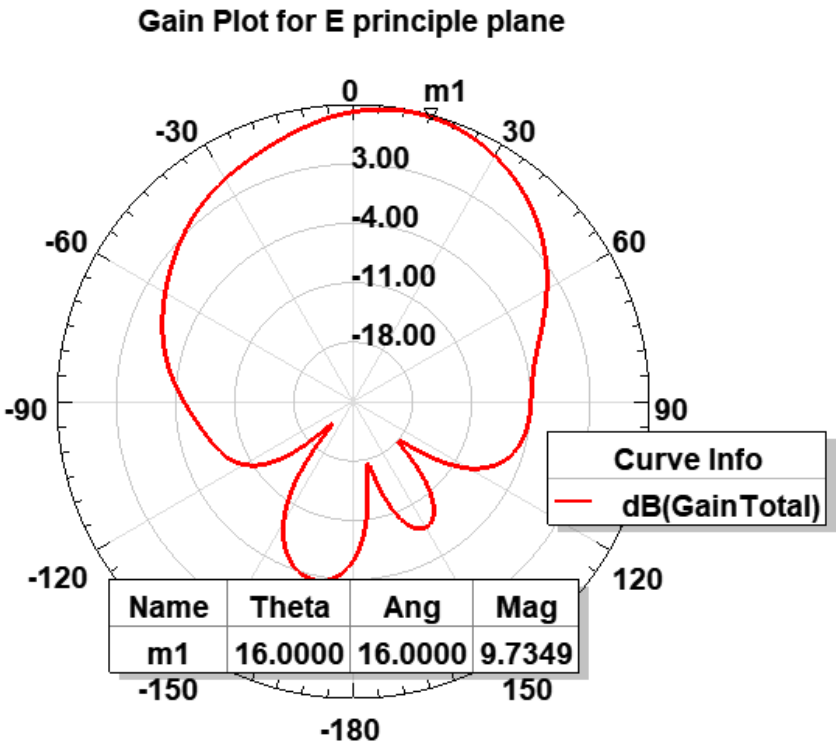

Figure 4.11 Gain plots positive angle steering for antenna structure with PRS for E principal plane

Figure 4.11 show the gain plots for positive beam steering of 16 degrees in E principal plane. It can be observed that the steering happens in the E principal plane since the PRS layer is placed in E plane. The gain of the patch antenna remains unchanged whenever the placement of the PRS is done for beamsteering. If the steering needs to happen at the negative angles, then the placement of the PRS should be done on the opposite side of the antenna.

This process can be realized for H principal plane. Figure 4.12 shows the arrangement of patch antenna along with the PRS for H principal plane. Figures 4.13 show the radiation pattern plots for positive beam steering for 14 degrees. It can be observed that the steering happens in the H principal plane since the PRS layer is placed in H plane. The gain is not affected whenever the PRS is used for beamsteering. If the steering needs to happen at the negative angles, then the placement of the PRS should be done on the opposite side of the antenna.

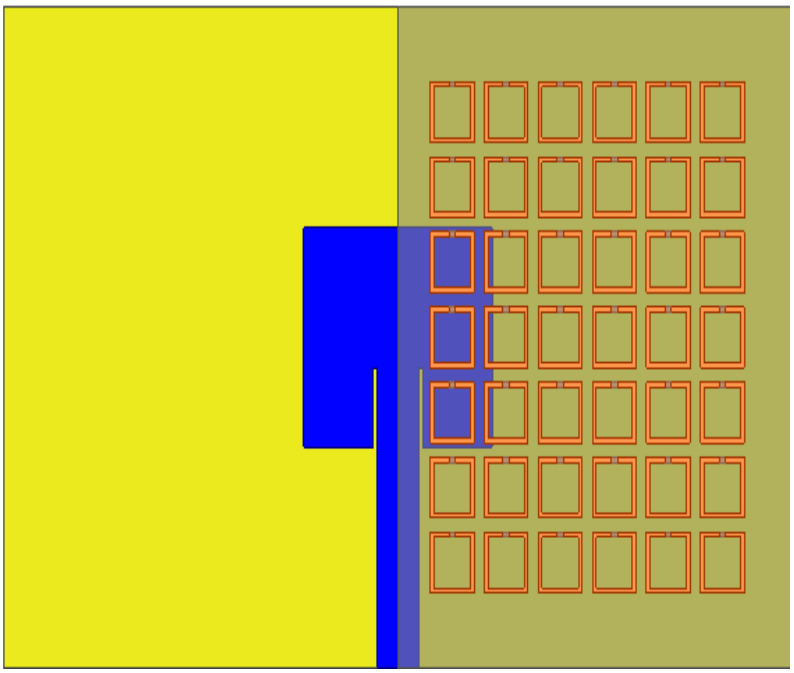

Figure 4.12 Antenna structure with PRS for H plane positive angle steering

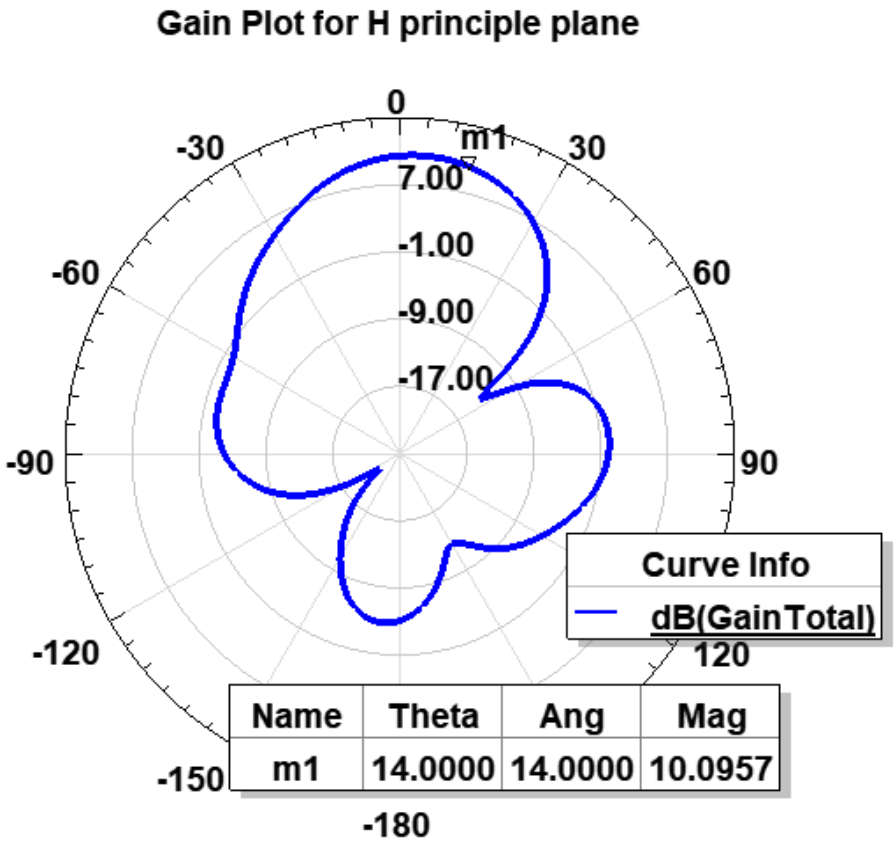

Figure 4.13 Gain plots positive angle steering for antenna structure with PRS for H plane

Figure 4.14 shows the S parameters for no PRS layer, H plane steering and E plane steering, as seen from the figure when partially reflective surfaces are placed on top of the patch antenna the impedance matching is not much affected. Depending on the steering angle needed the placement of the PRS can be adjusted accordingly. The principle will work for both E and H principal plane. This type of structures takes more computational memory and time. In order to steer the beam more efficiently and reduce the computational complexity and time a new method with vertical BCSRR is proposed in section 4.5.

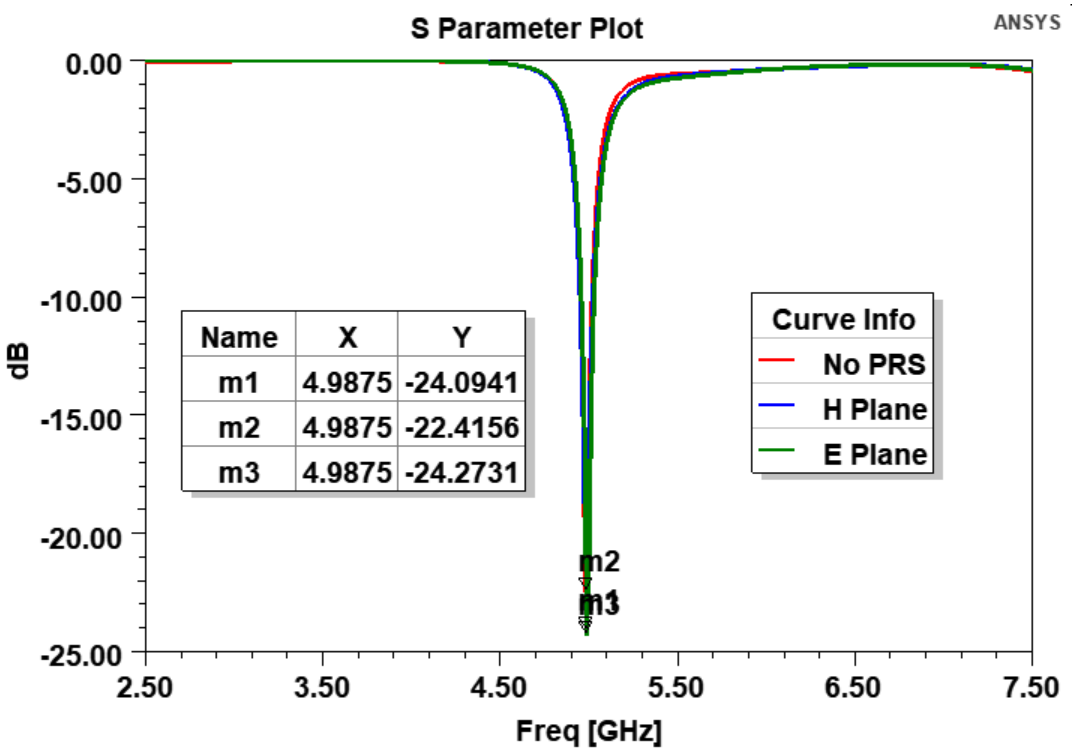

Figure 4.14 S parameter plot comparison for No PRS, H principal plane and for E principal plane

4.4.2 Beamsteering with multiple antennas using PRS layers.

Beamsteering takes place in phased array antennas by adding proper phase difference between the adjacent elements. The phase delay can be added using the PRS which will steer the beam.

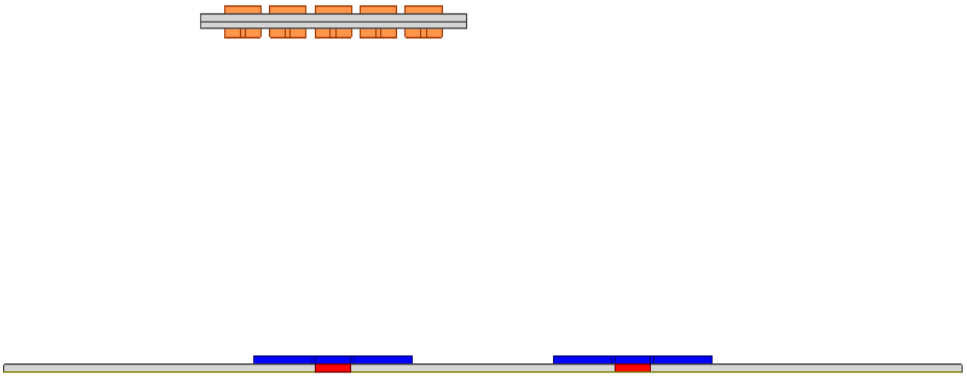

Figure 4.15 Single layer 2 element 2D view of phase delay by PRS

Figure 4.15 shows the arrangement of 2-element antenna with PRS in H principal plane. The BCSRR and the patch antennas were designed on Rogers 5880 with dielectric constant 2.2 and the substrate thickness of 0.8mm. Figure 4.16 shows the gain plots for negative angle steering. The steering of $-6°$ can be seen H principal plane.

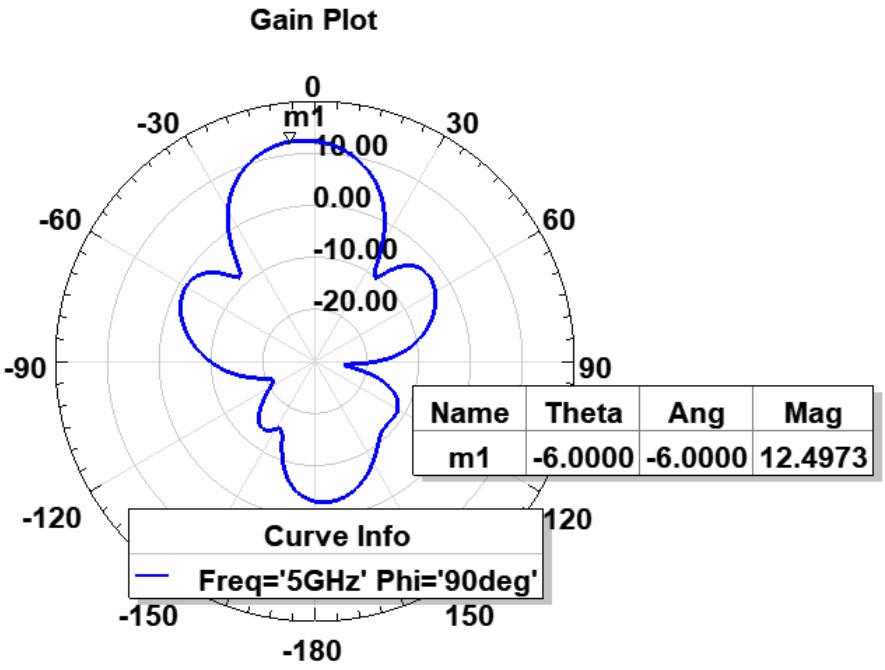

Figure 4.16 Gain plots negative angle steering for Single layer 2 element 2D view of phase delay by PRS

Figure 4.17 shows the arrangement of 2-element antenna with double layer PRS in H principal plane. The steering of $-10°$ can be seen H principal plane from figure 4.18. As can be seen the gain did not vary much for single layer and double layer PRS antennas. The steering angle can be varied by changing the dielectric constant, thickness of the PRS and by adding number of layers. The principle will work for both E and H principal planes.

Figure 4.17 Double layer 2D view of phase delay by PRS

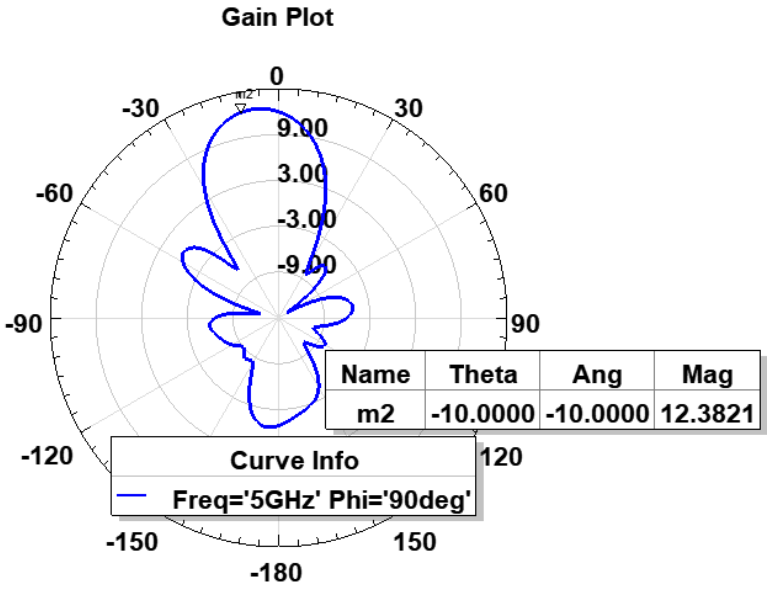

Figure 4.18 Gain plots negative angle steering for double layer 2D view of phase delay by PRS

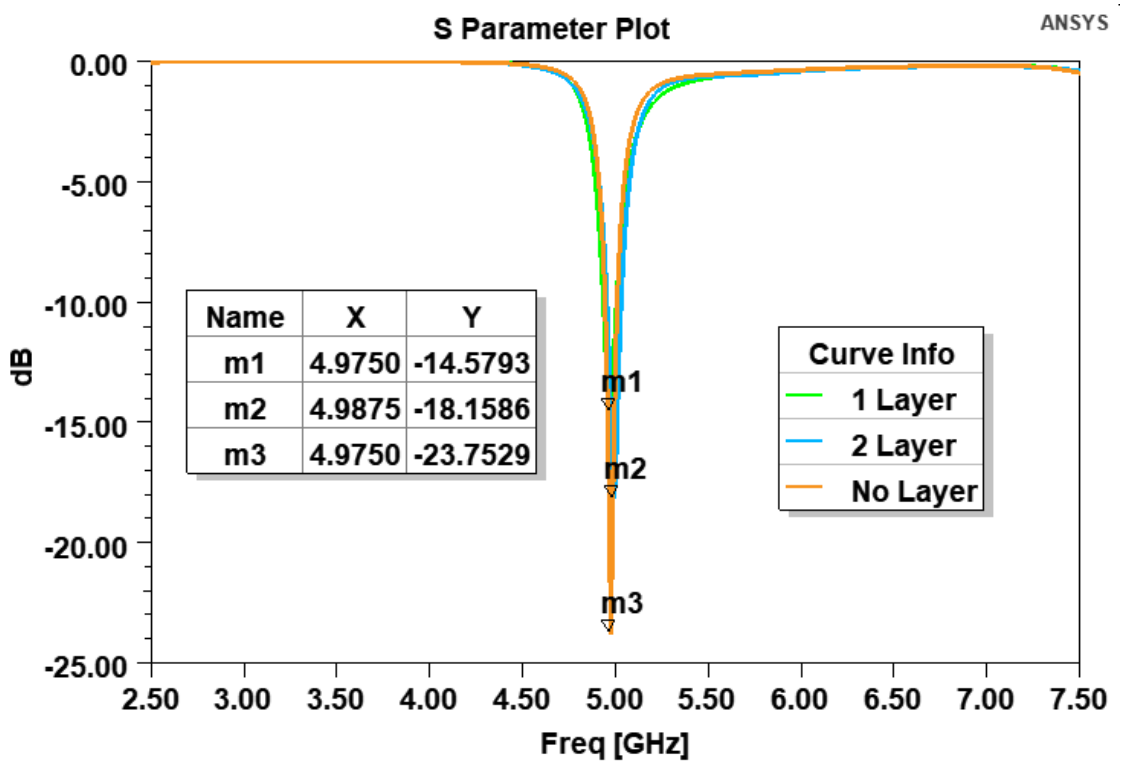

Figure 4.19 S parameter plots for 2x1 antenna array with no PRS layer, single layer and double layer

Figure 4.19 S parameter plots for 2x1 antenna array with no PRS layer, single layer and double layer, as seen from the figure when partially reflective surfaces are placed on top of the patch antenna the impedance matching is gets affected. The additional complexity and computational cost are not justified in this case as the steering angle does not vary much as the number of layers increase.

4.5 Beamsteering using Vertical Metamaterials (BCSRR)

In chapter 2 the design and implementation of metamaterials has been explained. Metamaterials have shown great promise for antenna applications, these structures have been used for size reduction of antennas and beamshaping as well as beamsteering. Although beam steering has been traditionally implemented in antenna arrays, the methods for beamsteering discussed here are potentially lower the cost and less complex to implement than the partially covered the patch configuration. For this case a high refractive index superstrate or electrically equivalent metamaterials substrates is placed in close

vicinity of the antenna. The proposed structure uses vertical split ring resonators and near field coupling. Full-wave simulations are employed to show beam deflections in the presence of high refractive index materials.

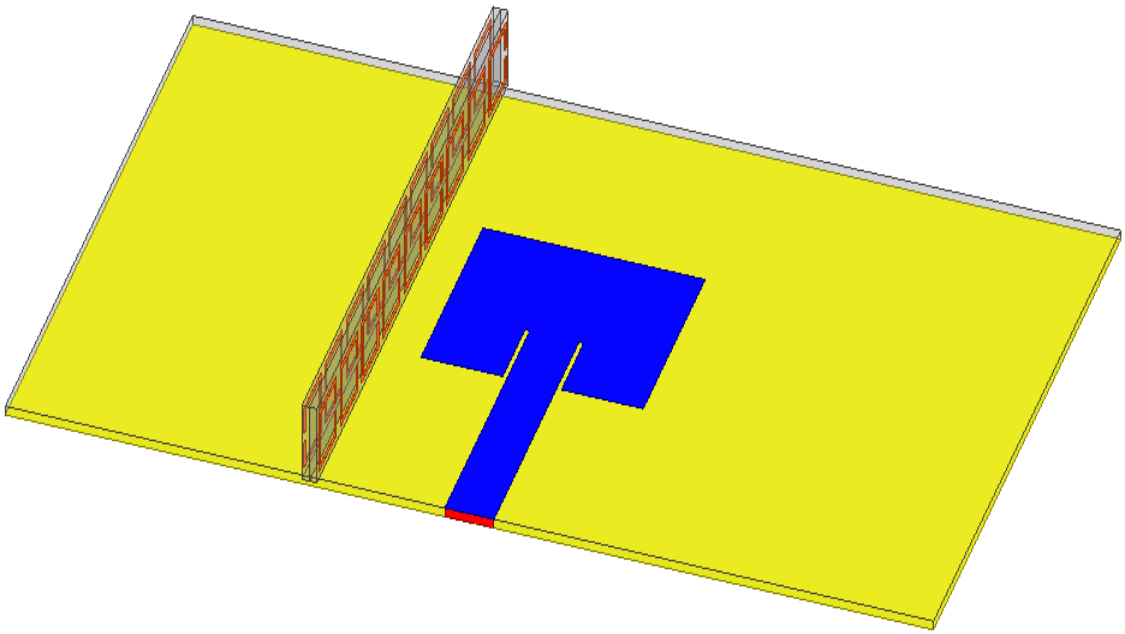

Figure 4.20 Antenna structure with vertical BCSRR for H plane negative angle steering

Figure 4.20 shows the arrangement of the microstrip patch antenna and BC-SRR for H principal plane with single layer. The antenna and BCSRR are designed on Rogers 5880 Duroid substrate with dielectric constant of 2.2 and the height of 0.8 mm to operate at 5 GHz. The design parameters can be referred to table 2 and table 3 for BCSRR and patch antenna respectively. The arrangement of the BCSRR is done in such a way that, if the required steering needs to happen toward positive angles then the arrangement of BCSRR should be on the right side of the patch and if the steering needs to happen on negative angles then the same arrangement of BCSRR are placed on the left side of the patch, respectively. In this section only negative beamsteering is shown with single layer. If the steering angle needs to be increased, then more layers need to be added. The spacing between the BCSRR layers is properly arranged so that the steering is more prominent. Note that the BCSRR

layers are placed on the sides of the patch antenna not directly on the patch antenna. If these layers are placed directly on top of the patch than, it will affect the radiation pattern as well as the return loss.

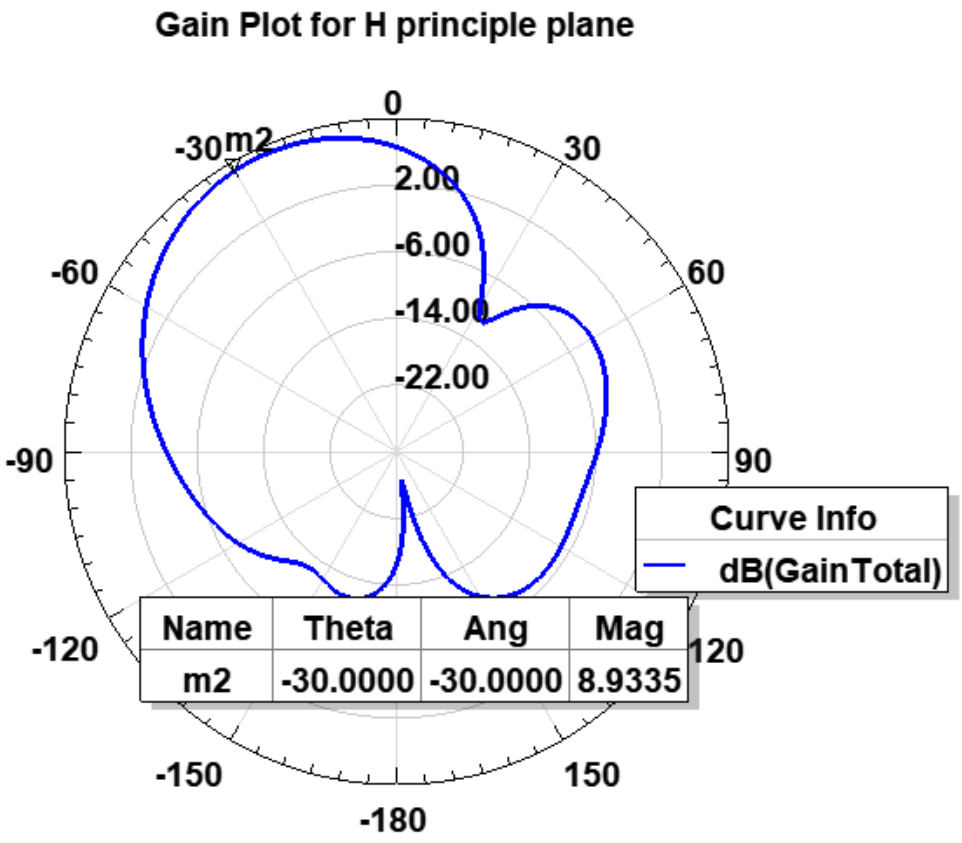

Figure 4.21 Gain plots positive angle steering with vertical BCSRR

Figures 4.21 show the radiation pattern plots for negative beam steering for -30 degrees. It can be observed that the steering happens in the H principal plane; this is because the placement of the BCSRR layers are in the H principal plane. The coupling happens in split rings and the radiated fields which induces time varying magnetic fields. Even though the split rings are placed in the close proximity of antenna the gain as well as the S parameters does not get affected. To avoid back radiations from the antenna it is ideal to increase the ground plane for better impedance matching. Ideally it is preferred to keep the ground plane $1.5 * \lambda$.

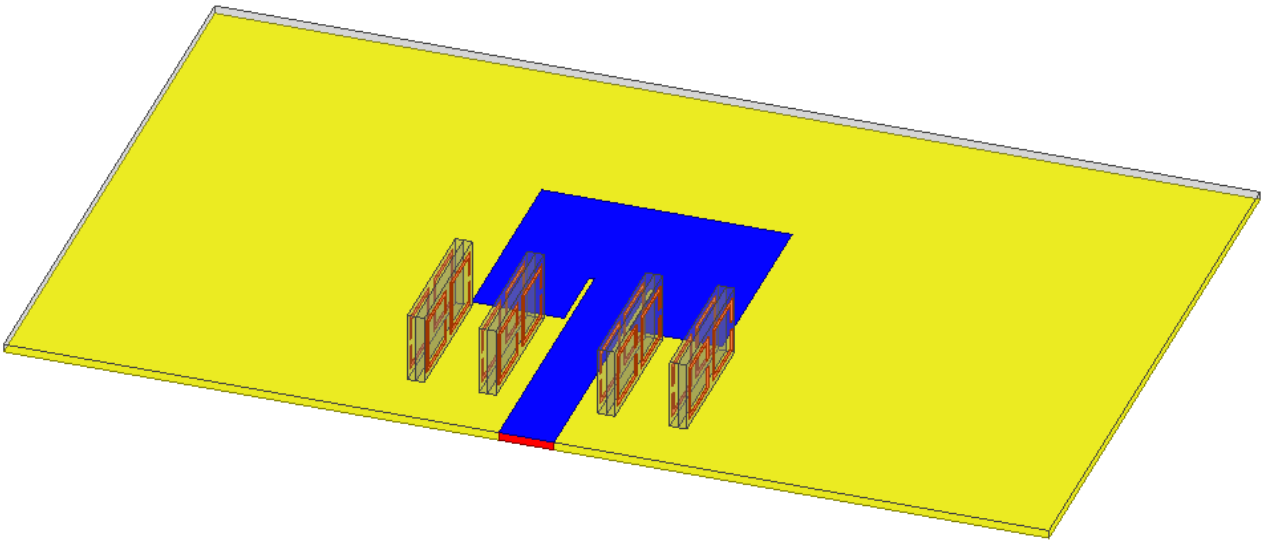

Figure 4.22 Antenna structure with vertical BCSRR for E plane positive angle steering

Figure 4.22 shows the arrangement of the microstrip patch antenna and BC-SRR for E principal plane with single layer. The antenna and BCSRR are designed on Rogers 5880 Duroid substrate with dielectric constant of 2.2 and the height of 0.8 mm to operate at 5 GHz. The design parameters can be referred to table 2 and table 3 for BCSRR and patch antenna respectively. The arrangement of the BCSRR is done in such a way that, if the required steering needs to happen toward positive angles then the arrangement of BCSRR should be near the microstrip line of the patch and if the steering needs to happen on negative angles then the same arrangement of BCSRR are placed on the other side of the patch.

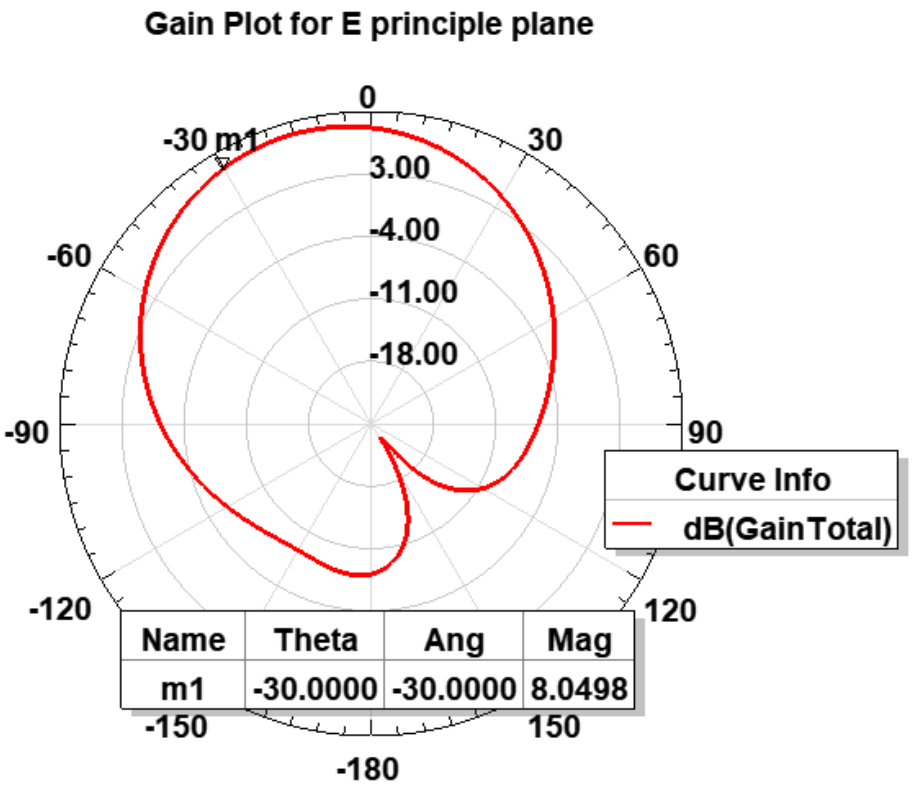

Figure 4.23 Gain plots positive angle steering with vertical BCSRR

Figures 4.23 show the radiation pattern plots for negative beam steering for -30 degrees. It can be observed that the steering happens in the E principal plane; this is because the placement of the BCSRR layers are in the E principal plane. The coupling happens in split rings and the radiated fields which induces time varying magnetic fields. Figure 4.24 shows the S parameters for no steering, H plane steering and E plane steering, as seen from the figure when metamaterials are placed in the closed vicinity of the patch antenna the impedance matching not much is affected. The advantages of this type of structure is the low simulation time and structural simplicity. Similarly, if the steering angle has to be negative then the displacement of the BCSRR should be on the other side of the antenna. Depending on the steering angle needed the layers of the BCSRR can be adjusted accordingly. The principle will work for both E and H principal plane.

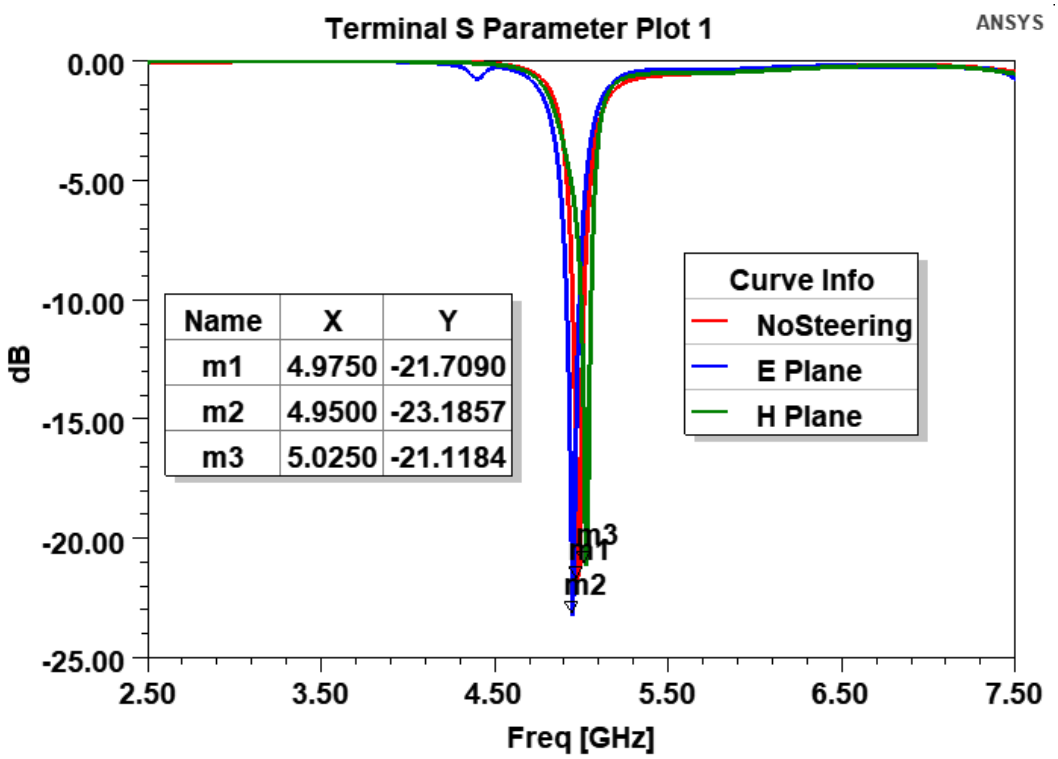

Figure 4.24 S parameter plots for antenna structure with vertical BCSRR comparing H plane steering, No steering and E plane steering

STRUCTURE TYPE	SIMULATION TIME	MEMORY REQUIRED
Horizontal Wedges	4 mins	1.8 GB
PRS	30 mins	19 GB
Vertical BCSRR	6 mins	2.8 GB

Table 4.1: Simulation time and memory requirements for different beamsteering techniques

CHAPTER 5

STUDIES IN QUASI-OPTICAL BEAMFORMING

5.1. Introduction

Beamforming is one of the important implementations capable of enabling high data rate wireless trafficking of multiple users/sensors devices simultaneously, and it greatly increases capacity for wireless sensing of multiple objects/features, e.g., including aircraft, weather events, atmospheric particulates, and pollutants. Extensive research is being carried out in the field of 5G communications. Beamforming is a technique that directs and shapes multiple signal beams in specified directions, rather than having the signals spread in all directions. This ability is very important for millimeter wave frequency applications such as small cell backhaul links where high path loss, attenuation from obstacles, and misalignment due to wind sway and accidents are prevalent. Beamforming controls the directionality and improves signal to noise ratio of the transmission and reception of the desired signals and mitigates the interference on an antenna array. Most effective beamforming implementations adapts to the signal environment. In other words, it can be explained as shaping multiple simultaneous beams and associated nulls. Optimal beamforming techniques dynamically adjust the array pattern to optimize some characteristic of the transmitted and received signals.

This chapter explores different types of quasi-optical beamformers with 3 element phased array antenna.

5.2 Importance of Matching Layer

Since the wedge faces are placed close to the antenna, the reflection can be very high from these wedges depending on the dielectric constant of the wedge as well as the angle of incidence. An

impedance matching layer helps reduce the reflection considerably, with one or more matching layers between the two interacting surfaces. Different types of matching techniques have been introduced over the years including a single quarter wave transformer impedance matching layer, single/ double transmission line sections to match the complex load and so on. [79]. The characteristic impedance of a dielectric medium is proportional to the inverse of the square root of the dielectric constant. Hence, we shall take normalized impedance Z of any medium as $\sqrt{\frac{1}{\varepsilon_r}}$.

Figure 5.1 shows the diagram with gap matching layer, where Rogers 5880 is used as the substrate with dielectric constant of 2.2 and loss tangent of 0.0009. The superstrate/ wedge is taken to be Rogers 6810 with dielectric constant of 10.2 and loss tangent of 0.0009. Assuming the dielectric constant of substrate is ε_{r1} and the dielectric constant of the superstrate is ε_{r2}, the dielectric constant of the matching layer ε_m can be calculated as

$$\varepsilon_m = \sqrt{\varepsilon_{r1} \cdot \varepsilon_{r2}}$$

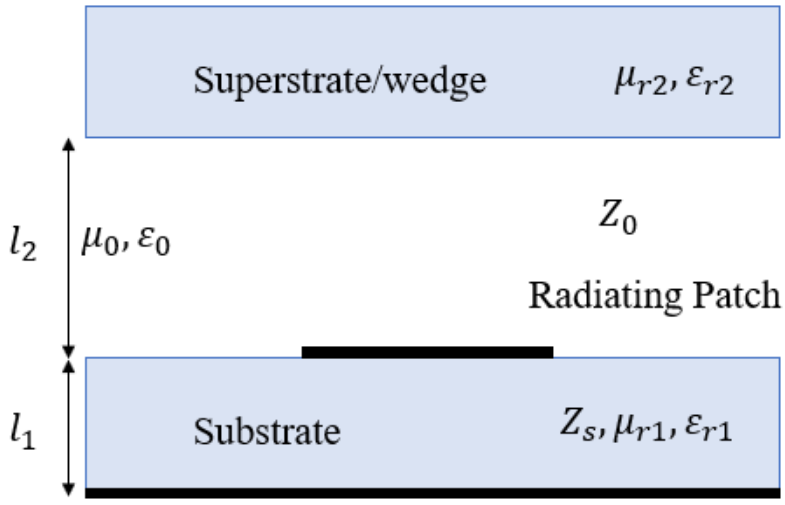

Figure 5.1 Transmission line analogy of placement of superstrate/wedge on top of antenna

Let Z_1 and Z_2 be the impedances of the thin dielectric layer and air gap respectively. Also let the characteristic impedance of air and substrate be Z_0 and Z_s. And their propagation constants can be given as $\beta_1 \; and \; \beta_2$ respectively. Using transmission line relations

$$Z_1 = Z_s \frac{Z_0 \cos \beta_2 l_2 + Z_s \sin \beta_2 l_2}{Z_s \cos \beta_2 l_2 + Z_0 \sin \beta_2 l_2}$$

$$Z_2 = Z_0 \frac{Z_s \cos \beta_1 l_1 + Z_0 \sin \beta_1 l_1}{Z_0 \cos \beta_1 l_1 + Z_s \sin \beta_1 l_1}$$

For complete matching condition $Z_1 = Z_2{}'$

$$Z_s \frac{cos\theta_2 + jxsin\theta_2}{xcos\theta_2 + jsin\theta_2} = Z_0 \frac{xcos\theta_1 - jsin\theta_1}{cos\theta_1 - jsin\theta_1}$$

Where $\theta_1 = \beta_1 l_1$

$\theta_2 = \beta_2 l_2$ and $x = {}^{Z_s}/_{Z_0}$

After equating the imaginary parts and simplifying

$$\theta_1 = \theta_2$$

After equating the real parts and simplifying

$$\tan \theta_1 = \tan \theta_2 = \sqrt{{}^{x}/_{(1 + x + x^2)}}$$

These relations are valid for any type of incidence angles. For the materials with very high dielectric constants, dimensions $l_1 \; and \; l_2$ becomes very small and requires high precision in making the matching layer.

5.3 Beamforming using horizontal dielectric wedges

This is the first type of arrangement which has been designed, investigated, and demonstrated for quasi optical beamforming. This structure is designed for 3 element antennas lying in the E principal plane, the design consists of matching layers and wedges for left and right angle beamsteering. These wedges are placed in the near field of the antennas. The arrangement of wedges is carefully chosen

for left and right antenna in order to achieve distinct beams. Note that the wedges are placed on top of left and right antennas and not on the middle antenna. The structure was simulated using absorbing boundary conditions. Rogers 5880 is used as the substrate with dielectric constant of 2.2 and loss tangent of 0.0009. And the superstrate/ wedge is taken to be Rogers 6810 with dielectric constant of 10.2 and loss tangent of 0.0009. The dielectric constant and thickness of the matching layer is calculated by using the formulae in section 5.1.

Figure 5.3 shows the S parameter plot where S11 is for the middle antenna, S22 is for the left antenna and S33 is for the right antenna. As seen from this figure the impedance matching is good for the entire design, which has been improved because of the matching layer. When all the antenna elements are excited at the same time the plane wave from the outer antenna elements interacts with the matching layer first followed by the wedges. The wedges create phase delay, and the steering happens as the wave interacts with the wedges. Figure 5.2 shows the arrangement of horizontal dielectric wedges placed on top antennas.

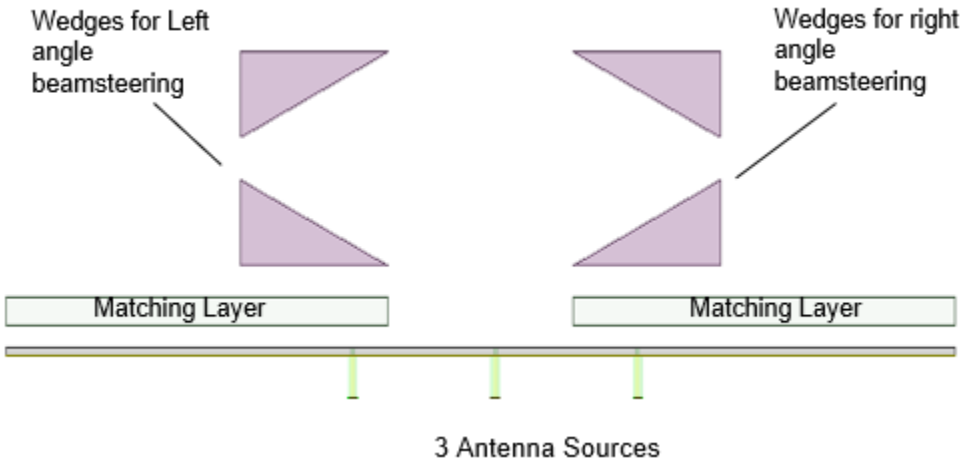

Figure 5.2 Horizontal dielectric wedges placed on top antennas

Figure 5.5 shows the electric field plot when all the antenna elements are active. It can be seen that three minimally overlapping beams are formed.

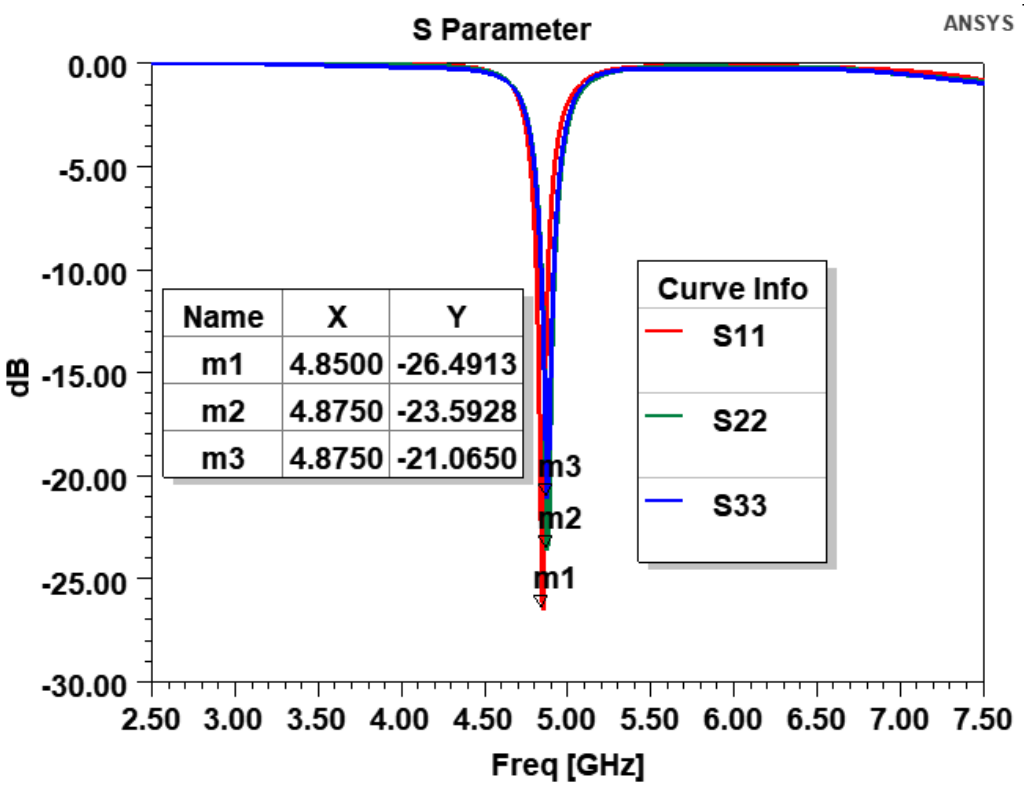

Figure 5.3 S parameter plot for horizontal dielectric wedges

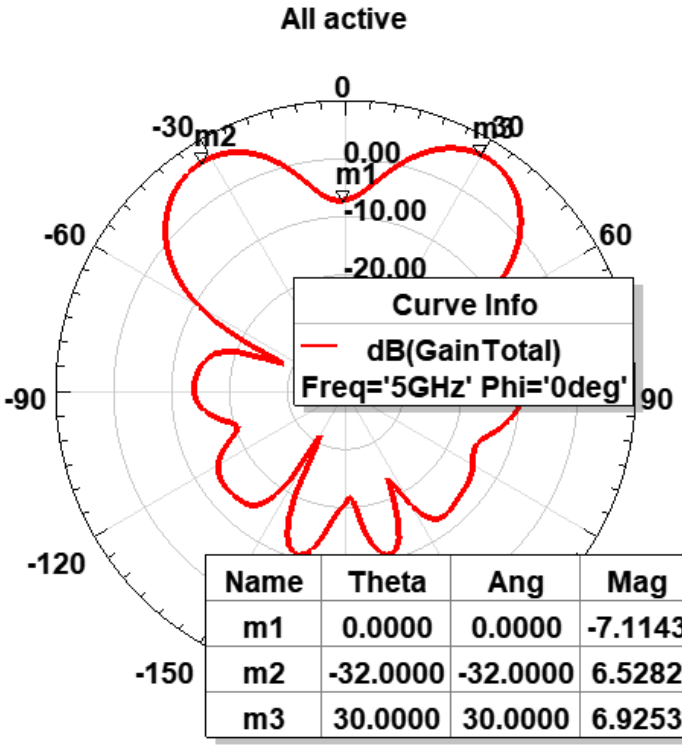

Figure 5.4 E principal plane gain plot for horizontal dielectric wedges with all elements excited

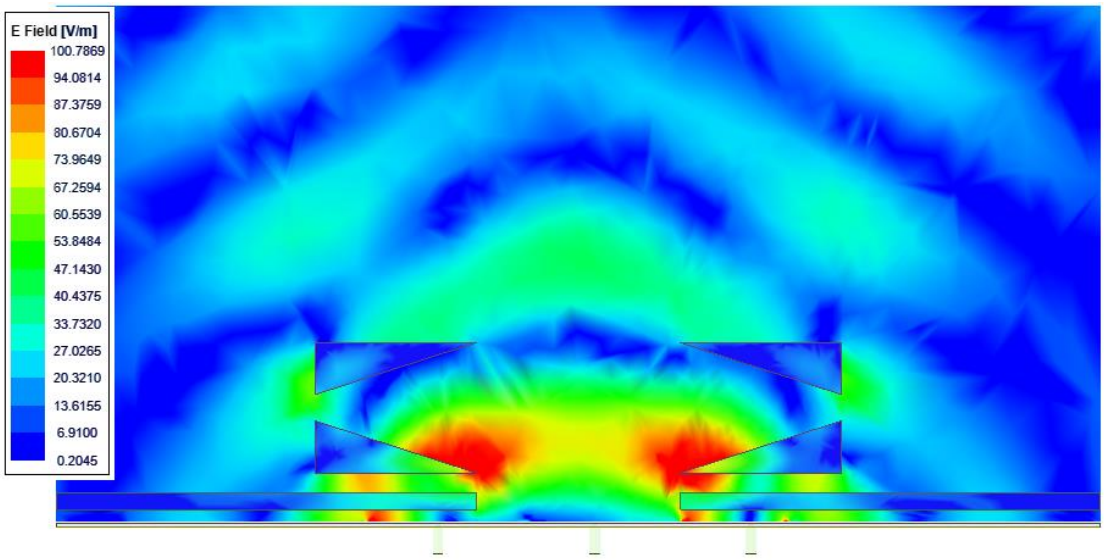

Figure 5.5 E field plot for horizontal dielectric wedges with all elements excited

Figure 5.4 shows E principal plane gain plot for horizontally oriented dielectric wedges with all elements excited. The plots the gain for individual antenna elements separately are shown in figures 5.6, 5.7 and 5.8 for E principal plane with middle element active, right element active and left element active respectively. As seen from figure 5.6 the gain of 5.1247 dB with zero beamsteering is achieved when only the middle element is excited.

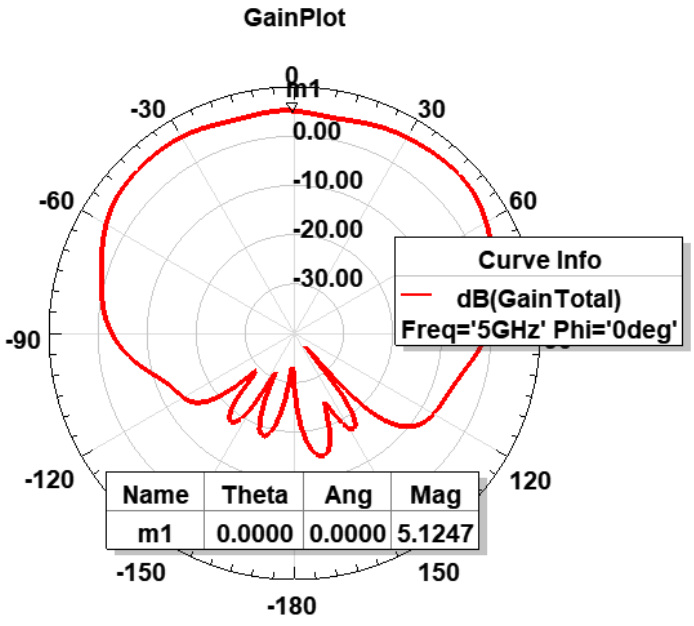

Figure 5.6 E principal plane gain plot for horizontal dielectric wedges with middle elements excited

Figure 5.7 shows the gain plot of right element and a gain of 3.9062 dB with 30 degrees beamsteering achieved when only the right element is excited. Figure 5.8 shows the gain plot of left element and a gain of 4.62 dB with -30 degrees beamsteering achieved when only the right element is excited. The steering angle can be varied by changing the dielectric constant of the wedges, thickness of the wedges as well as the flaring angle but note as the dielectric constant of the wedge is changed the properties of the matching layer will change. As seen from figures 5.6, 5.7 and 5.8 the gain of the antennas is not very high. To improve the gain a new structure with dielectric slabs is introduced in section 5.4.

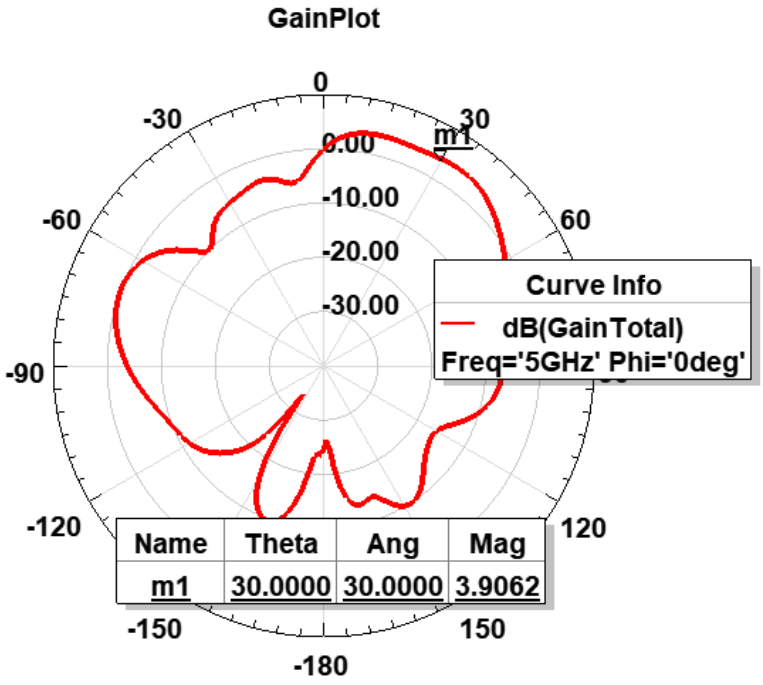

Figure 5.7 E principal plane gain plot for horizontal dielectric wedges with right elements excited

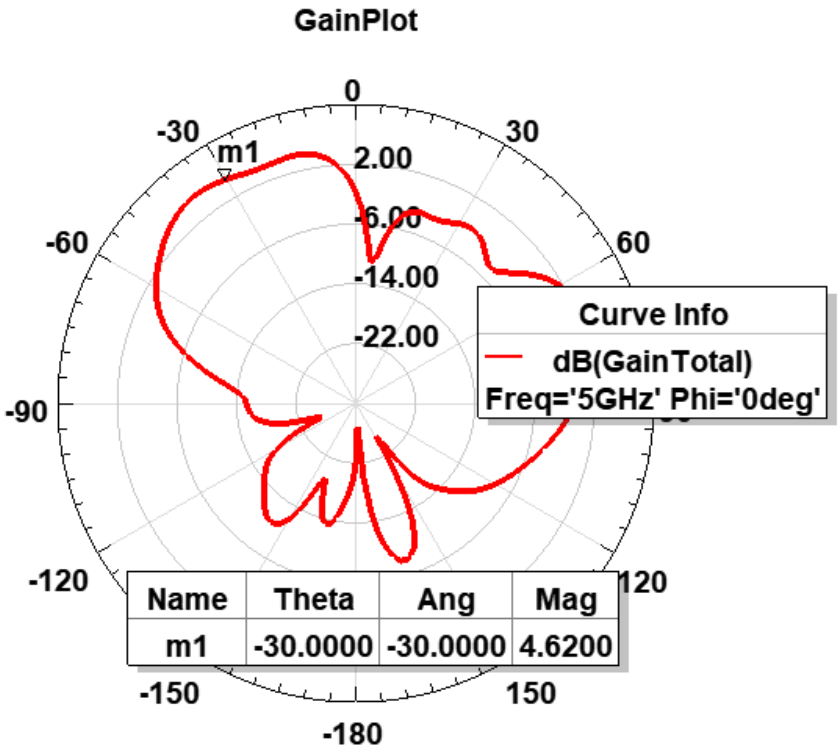

Figure 5.8 E principal plane gain plot for horizontal dielectric wedges with left elements excited

5.4 Beamforming using dielectric slabs

This is the second type of arrangement which has been designed, investigated, and demonstrated for improving the gain of the antennas in quasi optical beamforming. This structure is designed for 3-element antennas in E principal plane; the design consists of a dielectric slab in half convex lens type structure. The arrangement and angles of slabs is carefully chosen for left and right antenna in order to achieve three minimally overlapping beams. The structure was simulated using absorbing boundary conditions. Rogers 5880 is used as the substrate with dielectric constant of 2.2 and loss tangent of 0.0009. And the superstrate/ slabs is taken to be Rogers 6810 with dielectric constant of 10.2 and loss tangent of 0.0009. Figure 5.9 shows the arrangement half convex lens type dielectric slab placed on top antennas.

Figure 5.11 shows the S parameter plot where S11 is for the middle antenna, S22 is for the left antenna and S33 is for the right antenna. As seen from the figure 5.11 the impedance matching is good for the

entire design, except the middle antenna; since the middle antenna is very sensitive to the impedance matching. Different types of matching structures with different thickness, dielectric constants and shapes have been tried to improve the impedance matching of the middle antenna. Because of poor impedance matching the middle antenna does not radiate well as seen from figure 5.13.

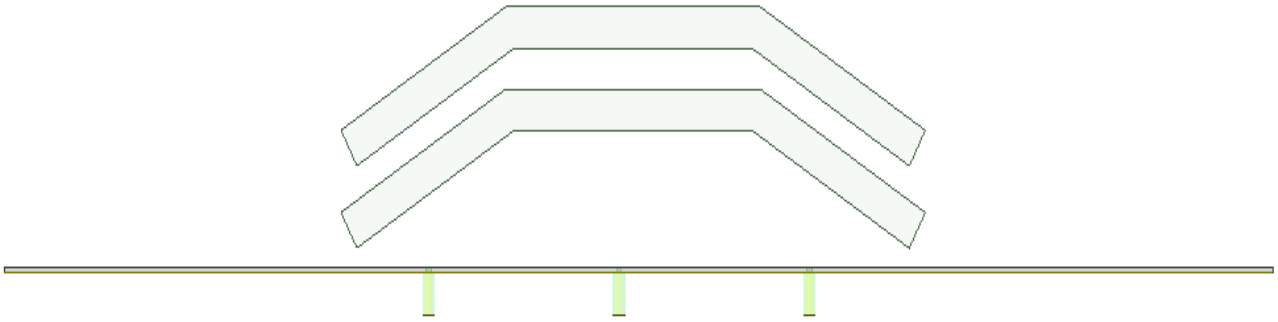

Figure 5.9 Half convex lens type dielectric slab placed on top antennas

Figure 5.10 shows the electric field plot when all the antenna elements are active. It can be seen that three minimally overlapping beams are formed.

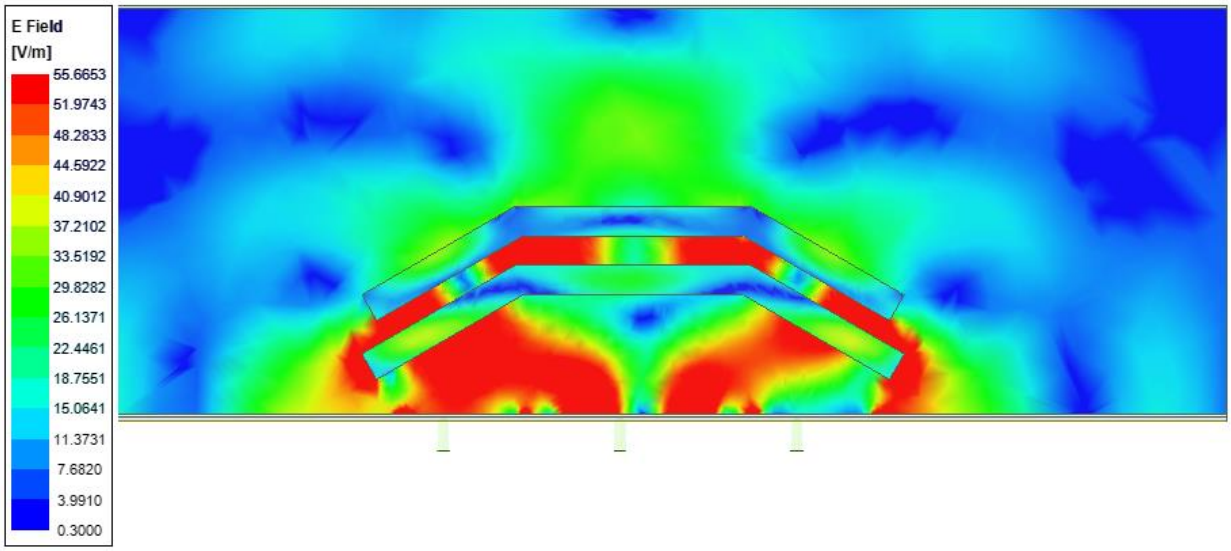

Figure 5.10 E field plot for dielectric slabs with all elements excited

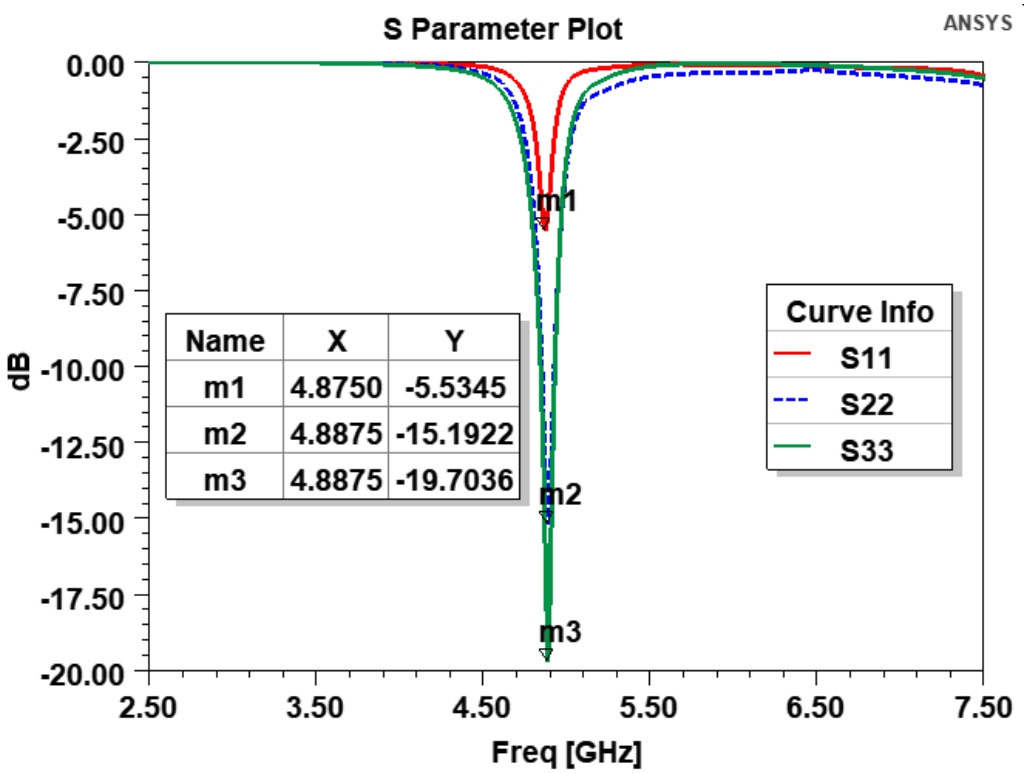

Figure 5.11 S parameter plot for dielectric slab

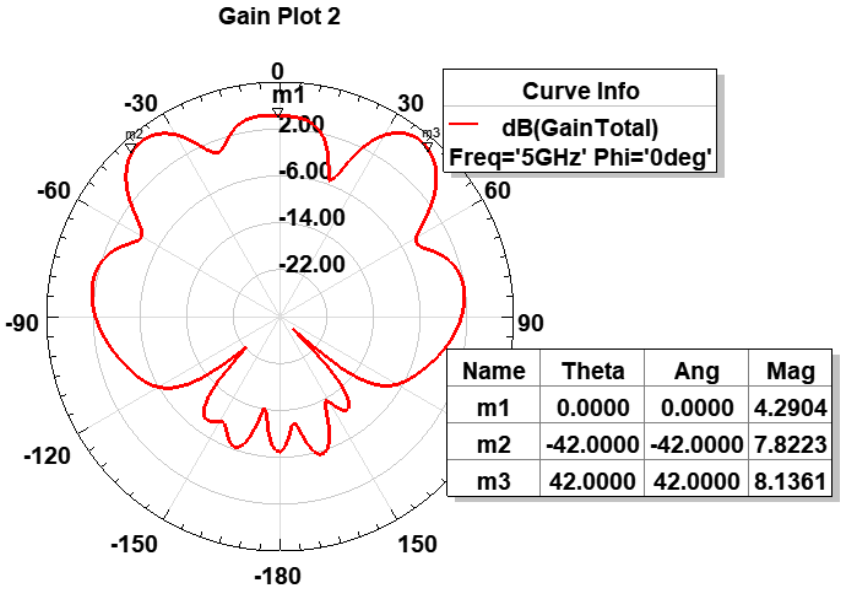

Figure 5.12 E principal plane gain plot for dielectric slab with all elements excited

Figure 5.12 shows the E principal plane gain plot for dielectric slab with all elements excited. As the

previous plots the gain for individual antenna elements activated separately are shown in figures 5.13, 5.14 and 5.15 for E principal plane with middle element excited, right element excited and left element excited respectively. As seen from figure 5.13 the gain of 5.4499 dB with zero beamsteering is achieved when only the middle element is excited. The beam is not directive, and it creates two grating lobes 33 degrees and -33 degrees. This is caused because of the reflections from the second dielectric slab and diffractions from the bends.

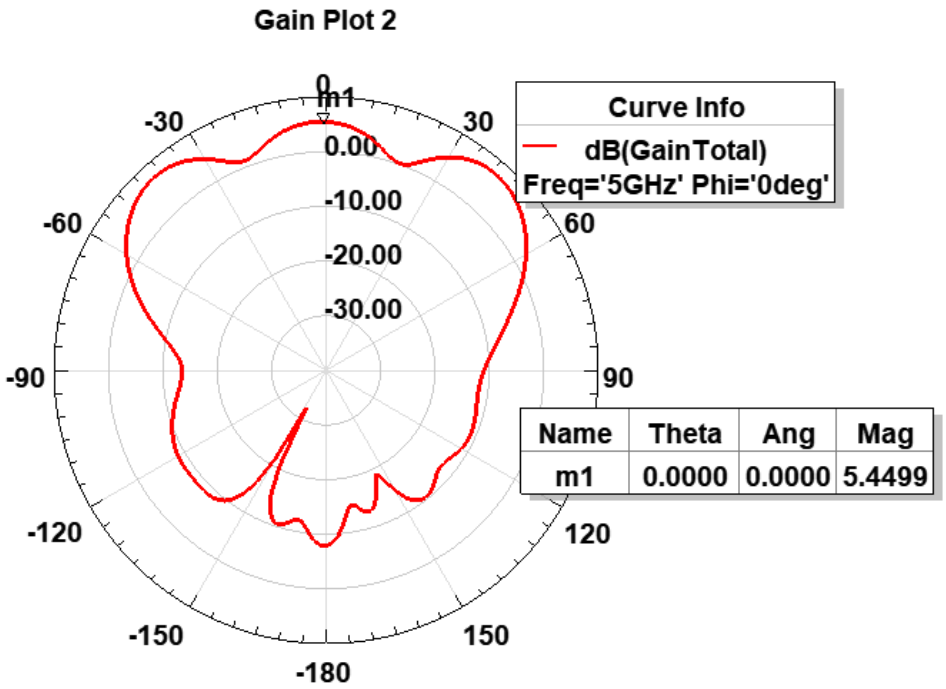

Figure 5.13 E principal plane gain plot for dielectric slab with middle elements excited

Figure 5.14 shows the gain plot of the left element and a gain of 10.7060 dB with -40 degrees beamsteering achieved when only the right element is excited. Figure 5.15 shows the gain plot of the right element and a gain of 10.6209 dB with -40 degrees beamsteering achieved when only the right element is excited. The steering angle can be varied by changing the dielectric constant of the slabs as well as the slab tilt angles for left and right elements. As seen from the above plots the impedance matching of the middle antenna is rather poor. To improve the gain and impedance matching of the

antennas a new structure with plano concave lens is introduced in section 5.5.

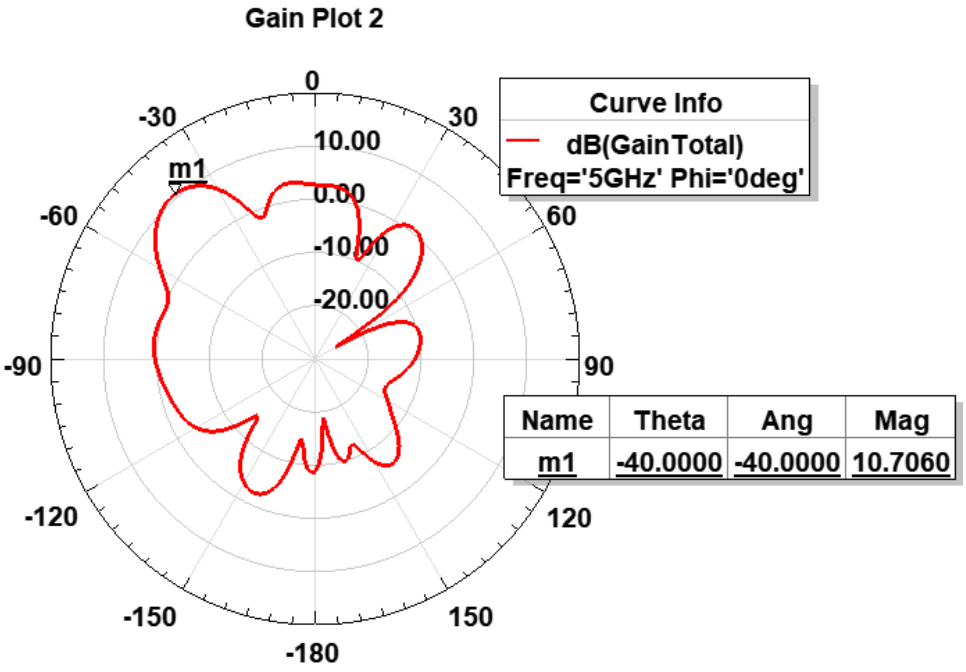

Figure 5.14 E principal plane gain plot for dielectric slab with right elements excited

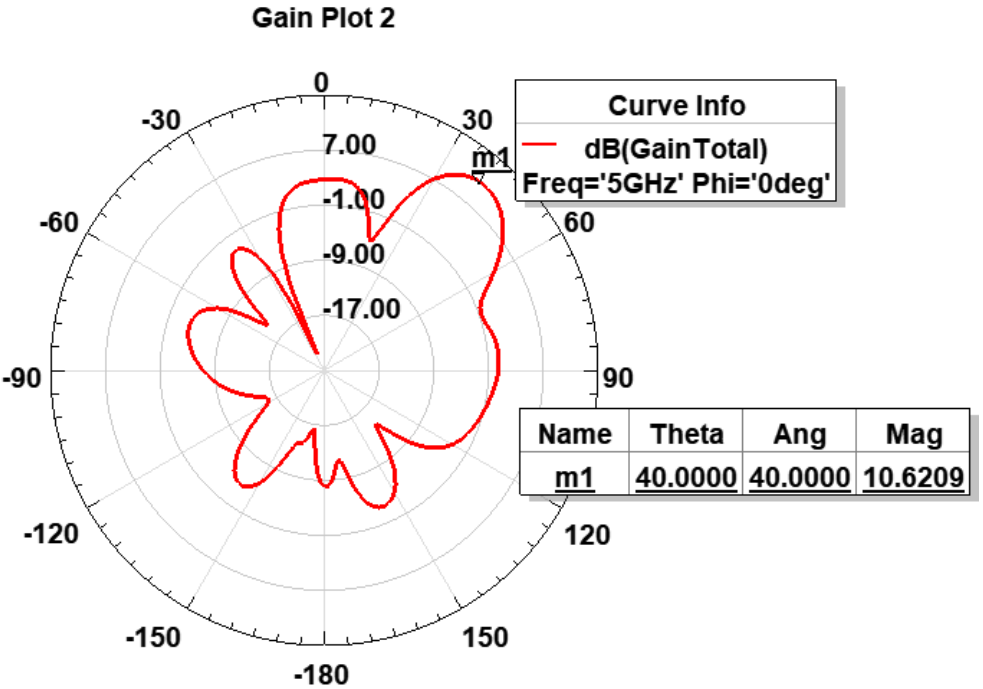

Figure 5.15 E principal plane gain plot for dielectric slab with right element excited

5.5 Beamforming using plano concave lens

This is the third type of arrangement which has been designed, investigated and demonstrated for improving the gain and impedance matching of the middle antenna in quasi optical beamforming. This structure is designed for 3-element antennas; the design includes two plano concave lenses. The plano concave lenses are placed in the near field of the antenna to avoid spillovers. The arrangement and radius of curvature of lens pair is carefully chosen for the middle, left and right antenna in order to achieve three minimally overlapping beams. The structure was simulated using absorbing boundary conditions. Rogers 5880 is used as the substrate with dielectric constant of 2.2 and loss tangent of 0.0009. Also the superstrate/ plano concave lens is taken to be Rogers 6810 with dielectric constant of 10.2 and loss tangent of 0.0009.

Figure 5.17 shows the S parameter plot where S11 is for the middle antenna, S22 is for the left antenna and S33 is for the right antenna. As seen from this figure the impedance matching has improved considerably for the entire design. S11 plot has been shifted to higher frequencies because of dielectric loading. This type of structure does not require impedance matching layer since the reflections from the lens results in constructive interference thereby improving the gain an impedance matching of the antennas. Figure 5.16 shows the arrangement of entire structure with plano concave lens placed on top of 3-element antenna.

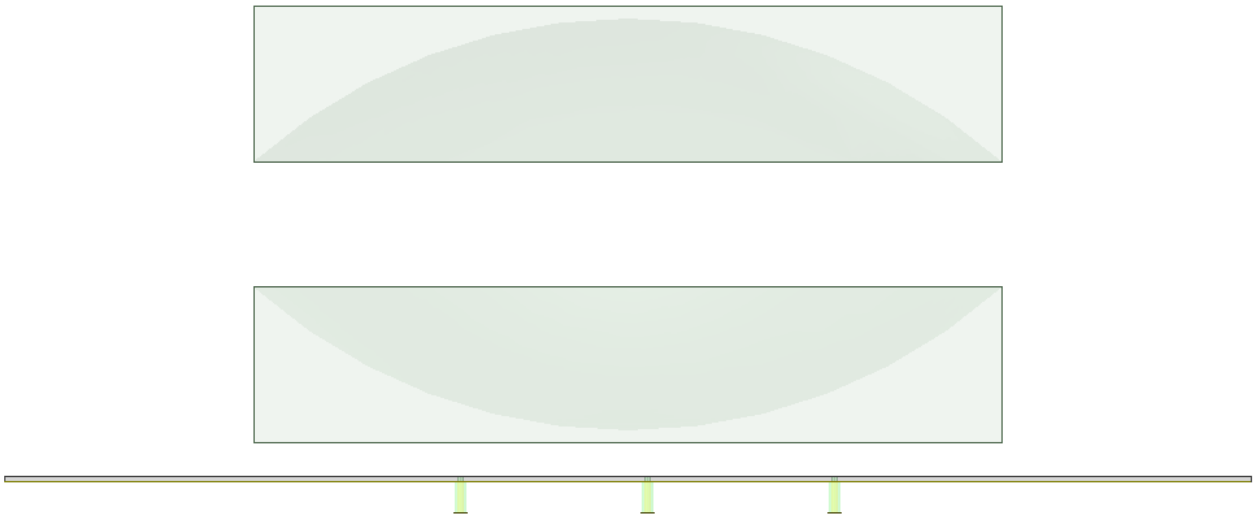

Figure 5.16 Plano concave lens placed on top antennas

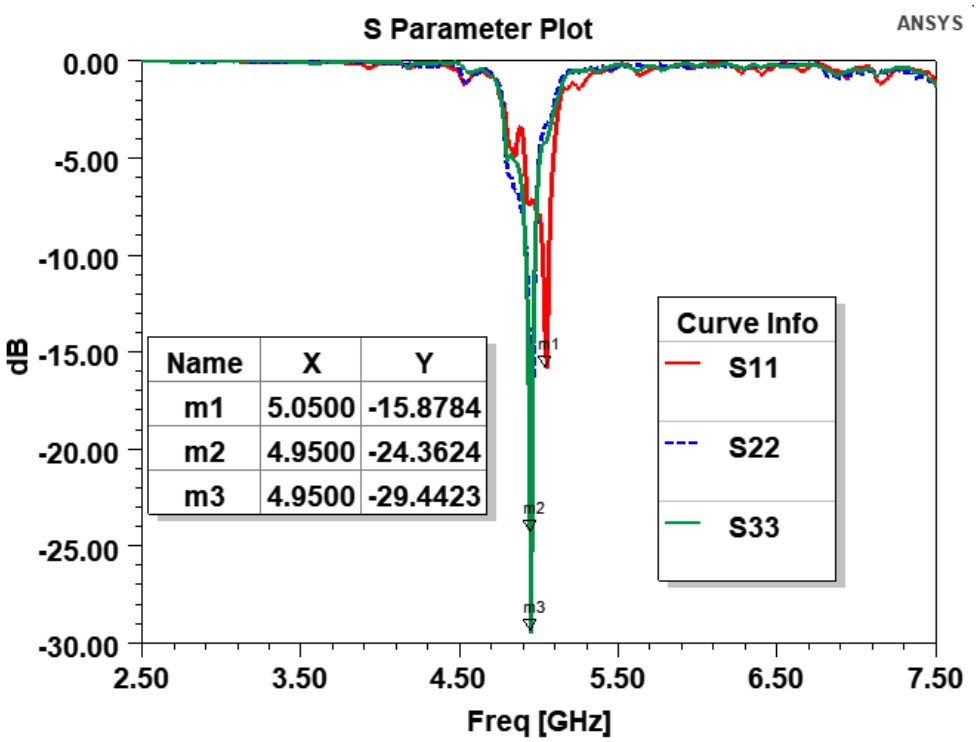

Figure 5.17 S parameter plot for plano concave lens

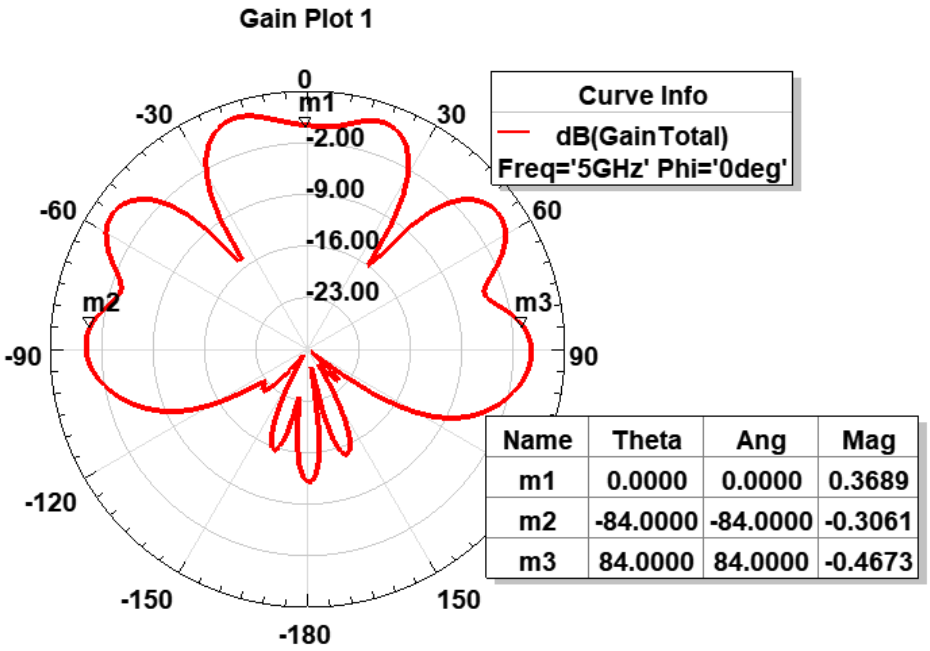

Figure 5.18 E principal plane gain plot for plano concave lens with all element excited

Figure 5.19 shows the electric field plot when all the antenna elements are active. It can be seen that three minimally overlapping beams are formed.

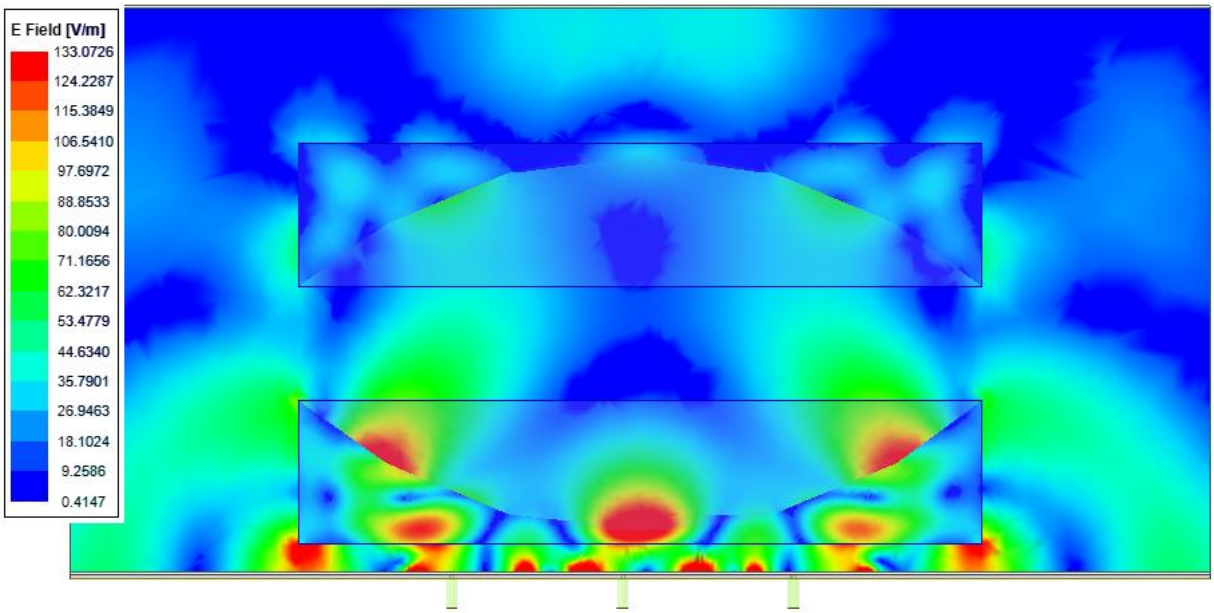

Figure 5.19 E field plot for plano concave lens with all elements excited

Figure 5.18 shows the E principal plane gain plot for plano concave lens with all element excited

Figures 5.20, 5.21 and 5.22 illustrate gain for E principal plane with middle element excited, right element excited and left element excited respectively. As seen from figure 5.20 the gain of 7.4031 dB with zero beamsteering is achieved when only the middle element is excited. The beam is still not as directive as desired and it creates two grating and a number of side lobes at different angles. This is caused due to the reflections for the middle antenna.

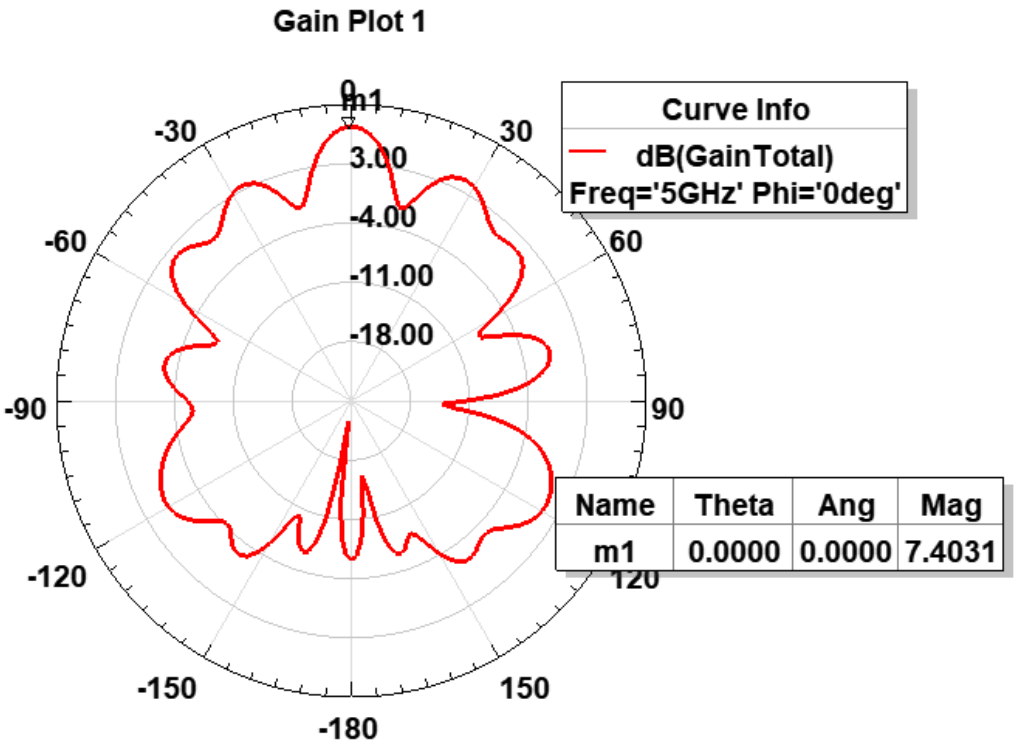

Figure 5.20 E principal plane gain plot for plano concave lens with middle element excited

Figure 5.21 shows the gain plot of the left element and a gain of 6.3505 dB with -84 degrees beamsteering achieved when only the right element is excited. Figure 5.22 shows the gain plot of the right element and a gain of 7.3084 dB with 84 degrees beamsteering achieved when only the right element is excited. The steering angle can be varied by changing the radius of curvature of the lens which is explained in section 5.6. As seen from the above plots the impedance matching and gain of the middle antennas has improved considerably as compared to the gain plots and impedance

matching of horizontal wedges and dielectric slabs. The gain of side antennas has degraded because of the reflections from the lens pair. To improve the gain and impedance matching of the antennas a new structure with vertical dielectric wedges is introduced in section 5.7.

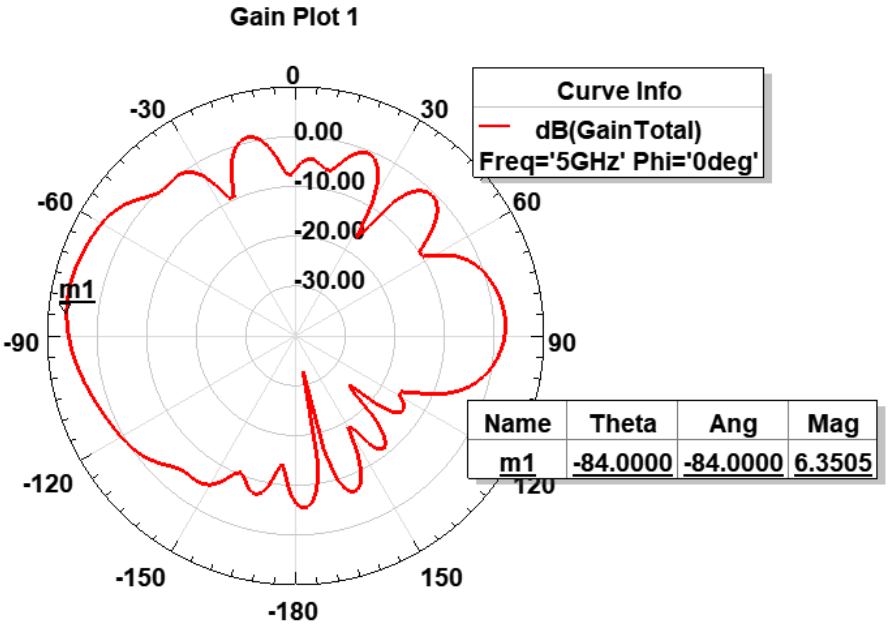

Figure 5.21 E principal plane gain plot for plano concave lens with left element excited

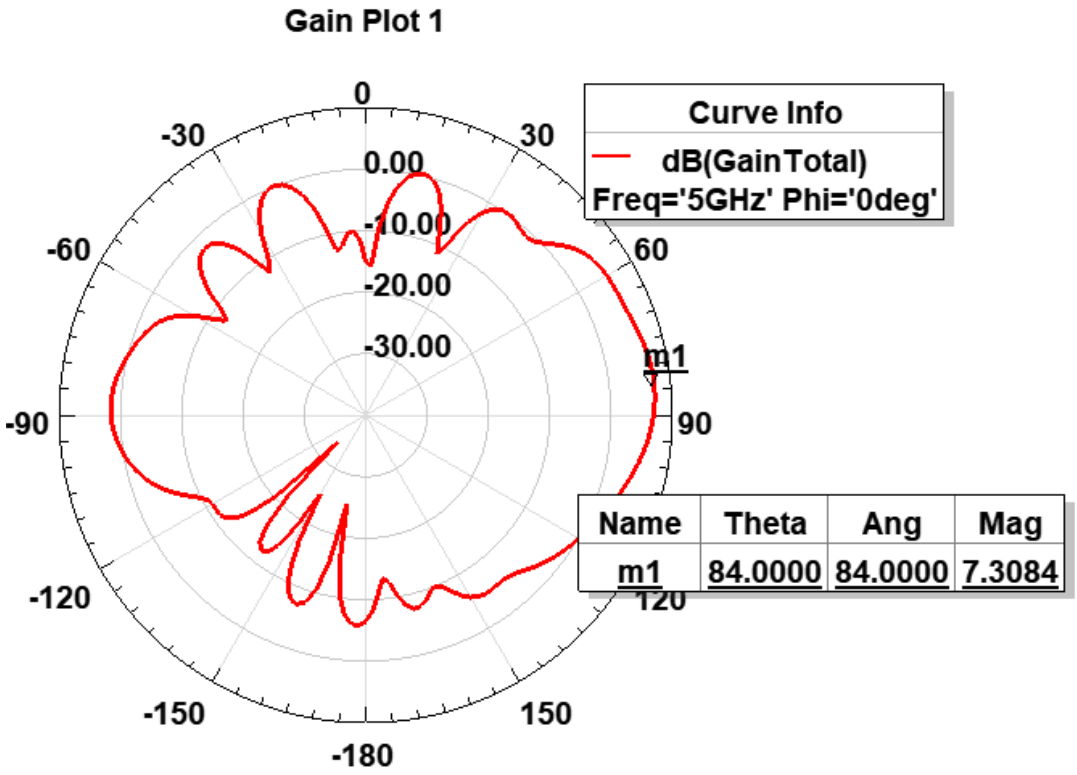

Figure 5.22 E principal plane gain plot for plano concave lens with right element excited

5.6 Beamsteering control using plano concave lens

To achieve the control of beamsteering angles, a straightforward technique has been analyzed and demonstrated. Beamsteering angles can be controlled by the varying radius of curvature of the plano concave lens. The plots for radius of curvatures of 60mm, 70mm, 80mm, and 90mm are shown in figures 5.23, 5.24 and 5.25. The results in section 5.5 are for the radius of curvature of 70 mm. The dielectric constant of the wedge is kept constant and only the radius of curvature is varied.

Figure 5.23 shows the gain plot of the middle antenna for different radius of curvatures. As seen from the plots, the gain increases and the grating lobes decreases as the radius of curvature increases. The reason behind such behavior can be explained using reflections from the concave lens. If the radius of curvature is smaller than the circumference of the lens; this results in less beam energy being steered thus increasing the reflections on the middle antenna as the total power will be directed towards the center.

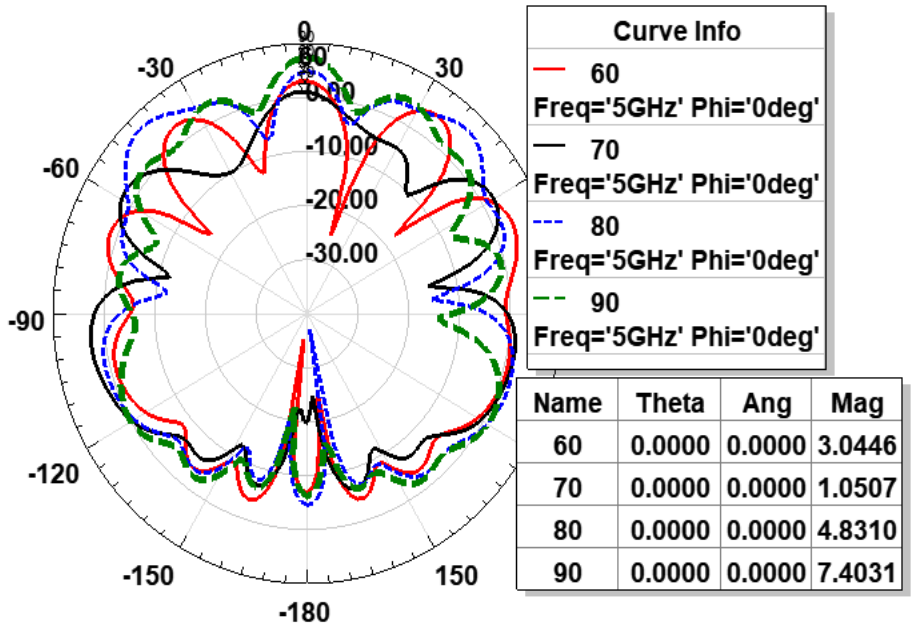

Name	Theta	Ang	Mag
60	0.0000	0.0000	3.0446
70	0.0000	0.0000	1.0507
80	0.0000	0.0000	4.8310
90	0.0000	0.0000	7.4031

Figure 5.23 E principal plane gain plots for plano concave lens with different radius of curvature when middle antenna is excited

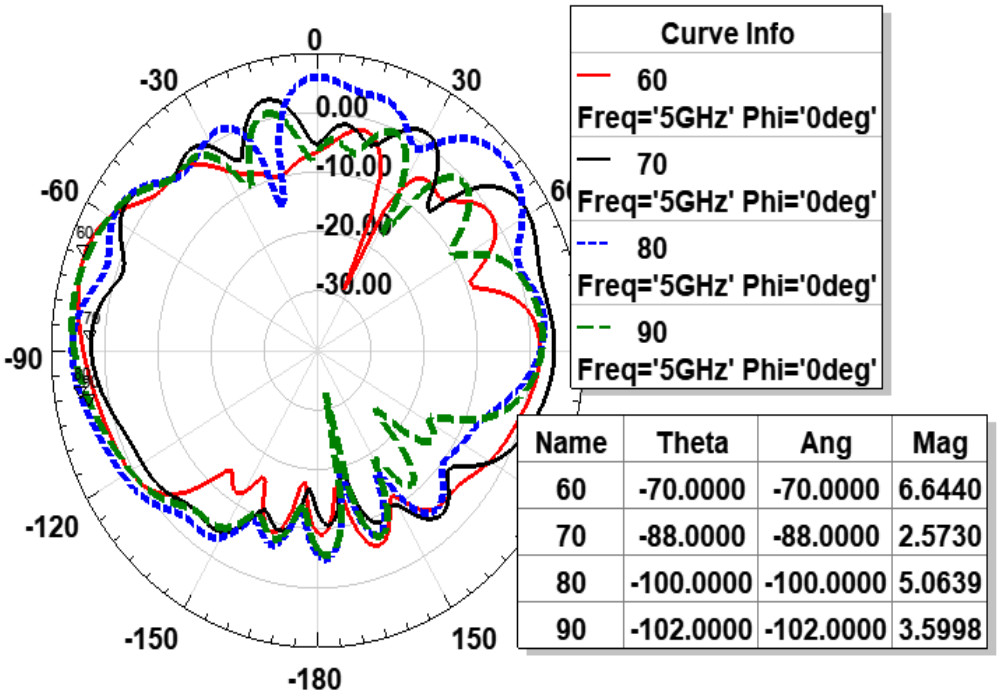

Name	Theta	Ang	Mag
60	-70.0000	-70.0000	6.6440
70	-88.0000	-88.0000	2.5730
80	-100.0000	-100.0000	5.0639
90	-102.0000	-102.0000	3.5998

Figure 5.24 E principal plane gain plots for plano concave lens with different radius of curvature when left antenna is excited

Figures 5.24 and 5.25 shows the right and left beamsteering gain plots. The plots for radius of curvatures of 60mm, 70mm, 80mm, and 90mm are shown. The dielectric constant of the lens is kept constant and only the radius of curvature is varied. As seen from the plots the beamsteering angle and the gain increases as the radius of curvature increase. Similarly, as the radius of curvature increases the beam steering angle increases.

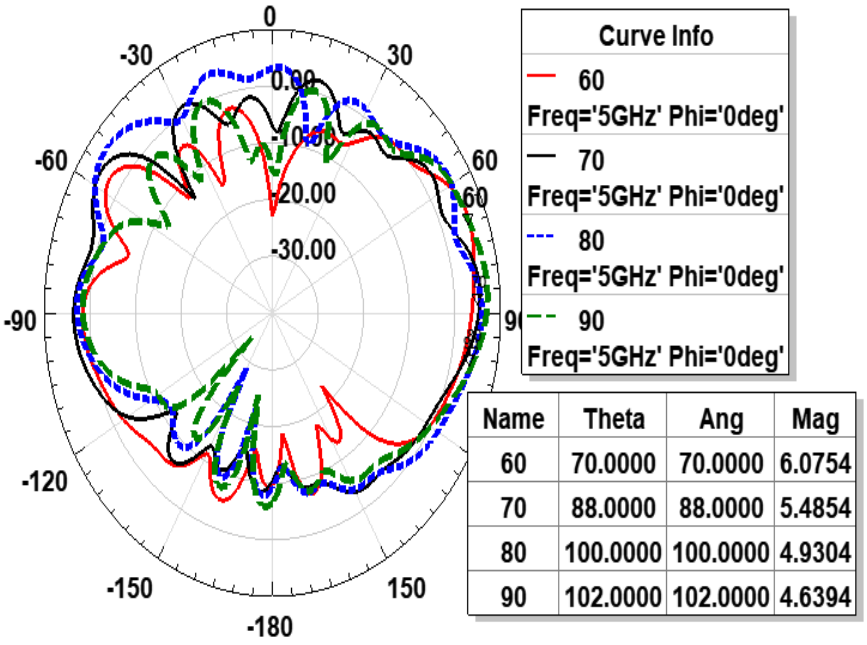

Name	Theta	Ang	Mag
60	70.0000	70.0000	6.0754
70	88.0000	88.0000	5.4854
80	100.0000	100.0000	4.9304
90	102.0000	102.0000	4.6394

Figure 5.25 E principal plane gain plots for plano concave lens with different radius of curvature when right antenna is excited

5.7 Beamforming using vertical dielectric wedges

This is the fourth type of arrangement which has been designed, investigated, and demonstrated for improving the gain and impedance matching of the antennas in quasi optical beamforming. This structure is designed for 3-element antennas; the design includes dielectric wedges placed vertically in the near field of the antenna to reduce spillovers. The arrangement and angle of vertical wedges is

carefully chosen for the middle, left and right antenna in order to achieve distinct beams. The structure was simulated using absorbing boundary conditions. Rogers 5880 is used as the substrate with dielectric constant of 2.2 and loss tangent of 0.0009. And the superstrate/ dielectric wedges are taken to be Rogers 6810 with dielectric constant of 10.2 and loss tangent of 0.0009. Figure 5.26 shows triangular dielectric wedges dielectric placed at some angles in the close vicinity of antennas.

Figure 5.29 shows the S parameter plot where S11 is for the middle antenna, S22 is for the left antenna and S33 is for the right antenna. As seen from this figure the impedance matching has improved considerably for the entire design as compared to the other configurations. This type of structure does not require an impedance matching layer since the since there are fewer reflections from these vertical dielectric wedges. The wedges are placed at 20 degrees tilt angles.

This design structure is easier to implement. Figure 5.28 shows the electric field plot when all the antenna elements are active. It can be seen that three minimally overlapping beams are formed.

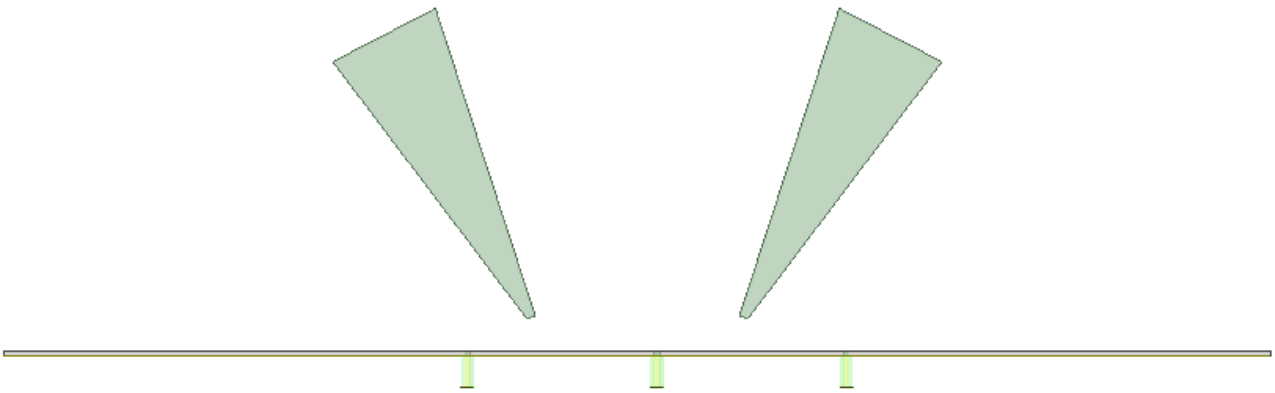

Figure 5.26 Triangular dielectric wedges dielectric placed at some angles in the close vicinity of antennas

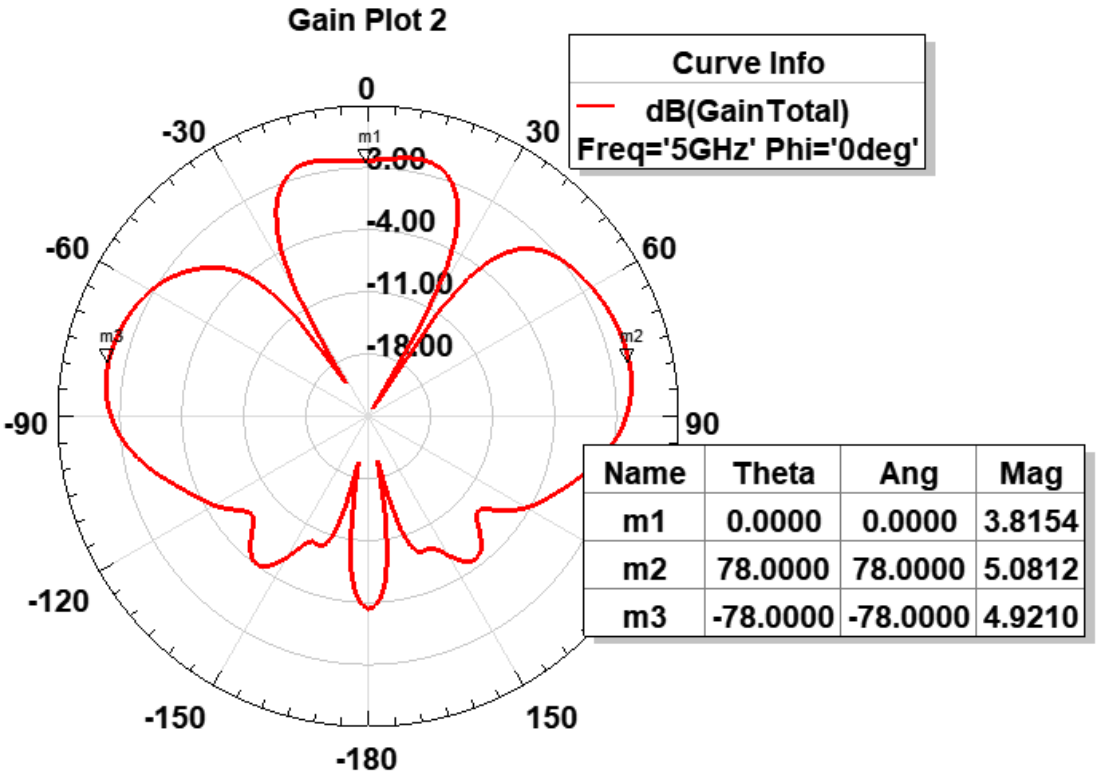

Figure 5.27 E principal plane gain plot for vertical dielectric wedges with all elements excited

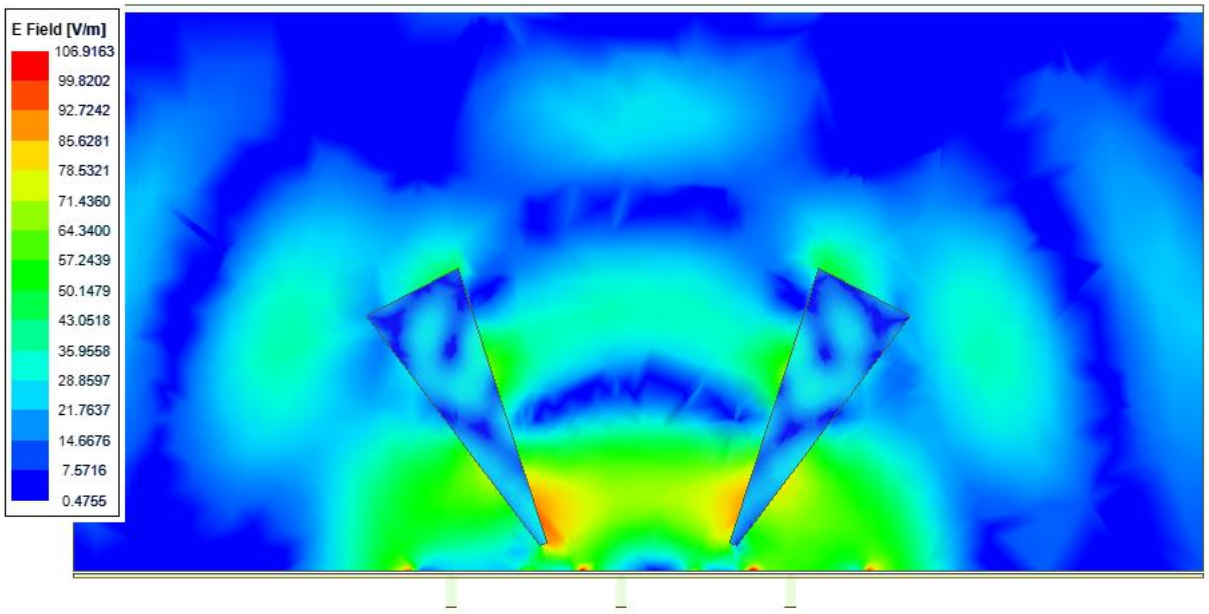

Figure 5.28 E field plot for vertical dielectric wedges with all elements excited

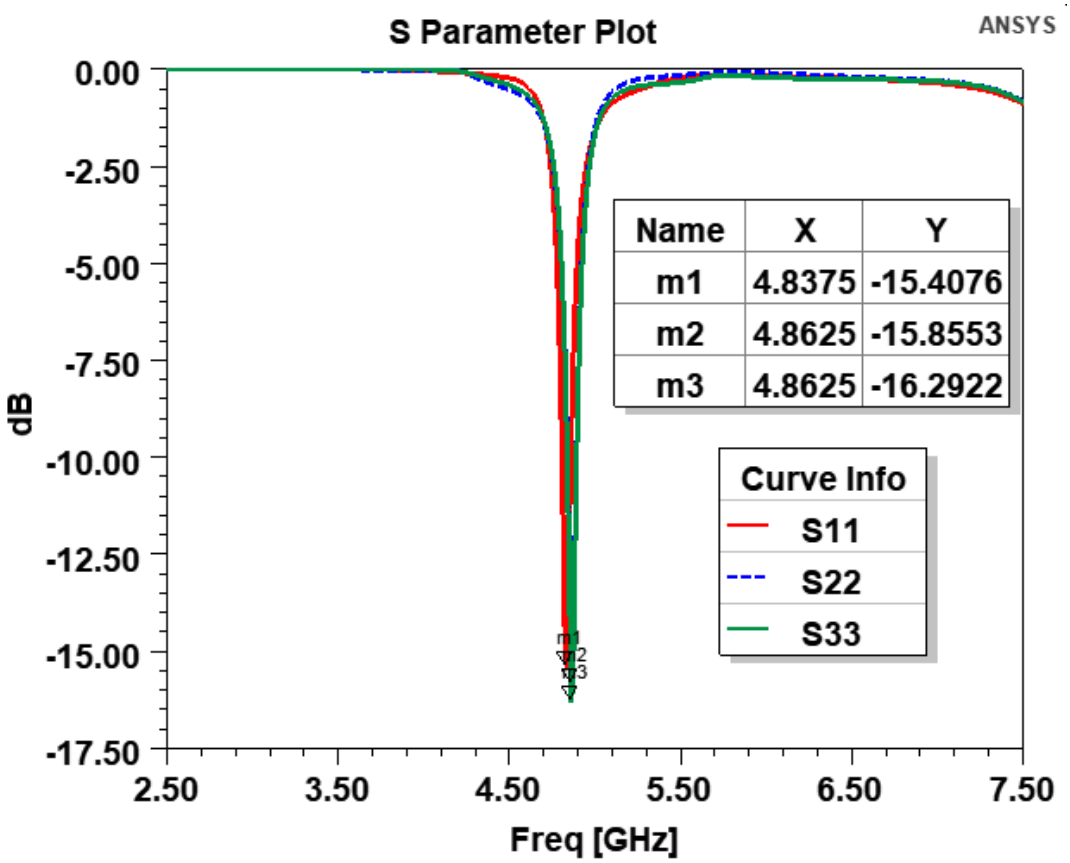

Figure 5.29 S Parameter Plot for vertical dielectric wedges

Figure 5.27 shows the E principal plane gain plot for vertical dielectric wedges with all elements excited. Figures 5.30, 5.31 and 5.32 shows the gain plots for E principal plane with middle element excited, right element excited and left element excited, respectively. As seen from figure 5.30 the gain of 11.7660 dB with zero beamsteering is achieved when only the middle element is excited. The beam is directive, but it creates two side lobes at different angles. This is caused due to the diffractions from the edges of vertical dielectric wedges.

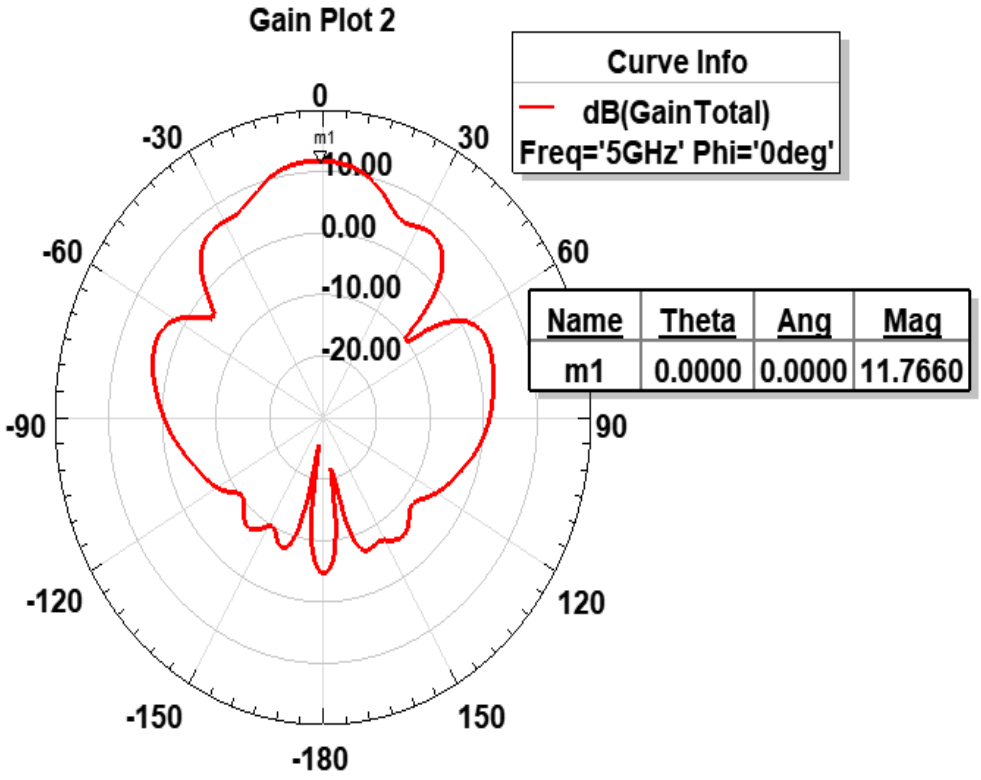

Figure 5.30 E principal plane gain plot for vertical dielectric wedges with middle element excited

Figure 5.31 shows the gain plot of the left element and a gain of 8.1273 dB with -80 degrees beamsteering achieved when only the left element is excited. Figure 5.32 shows the gain plot of the right element and a gain of 8.0286 dB with 80 degrees beamsteering achieved when only the right element is excited. The steering angle can be varied by changing the dielectric wedge tilting angles which is explained in section 5.8. As seen from the above plots the impedance matching and gain of the middle and side antennas has improved considerably compared to other configurations investigated.

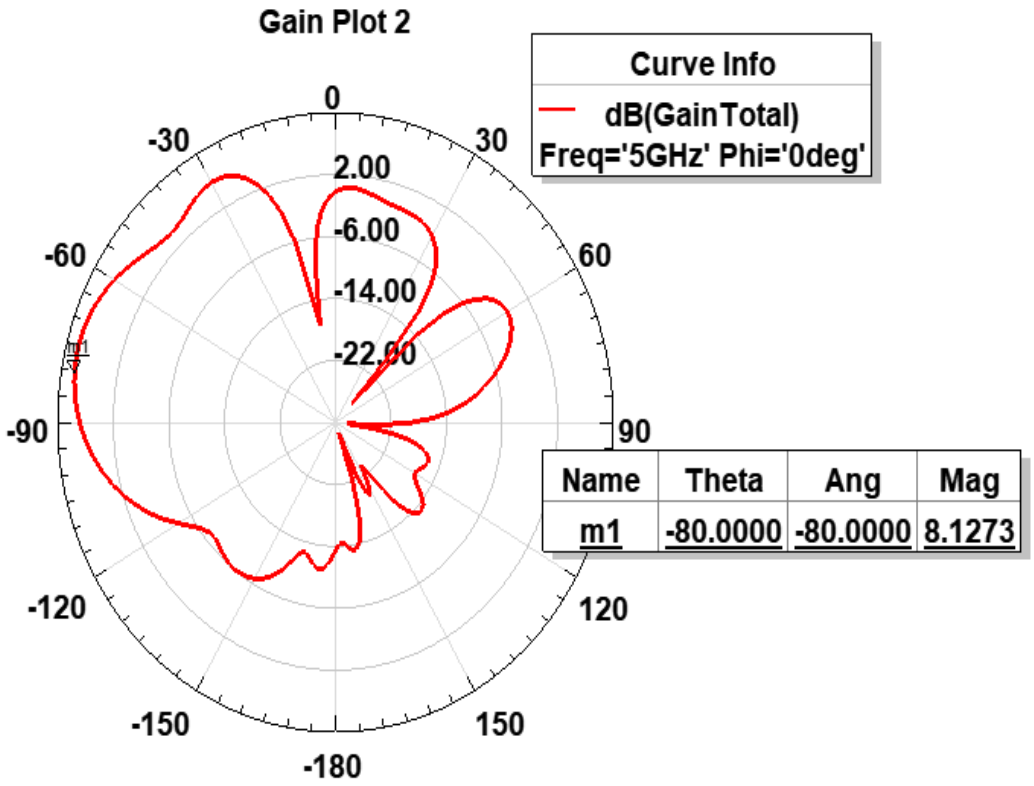

Figure 5.31 E principal plane gain plot for vertical dielectric wedges with left element excited

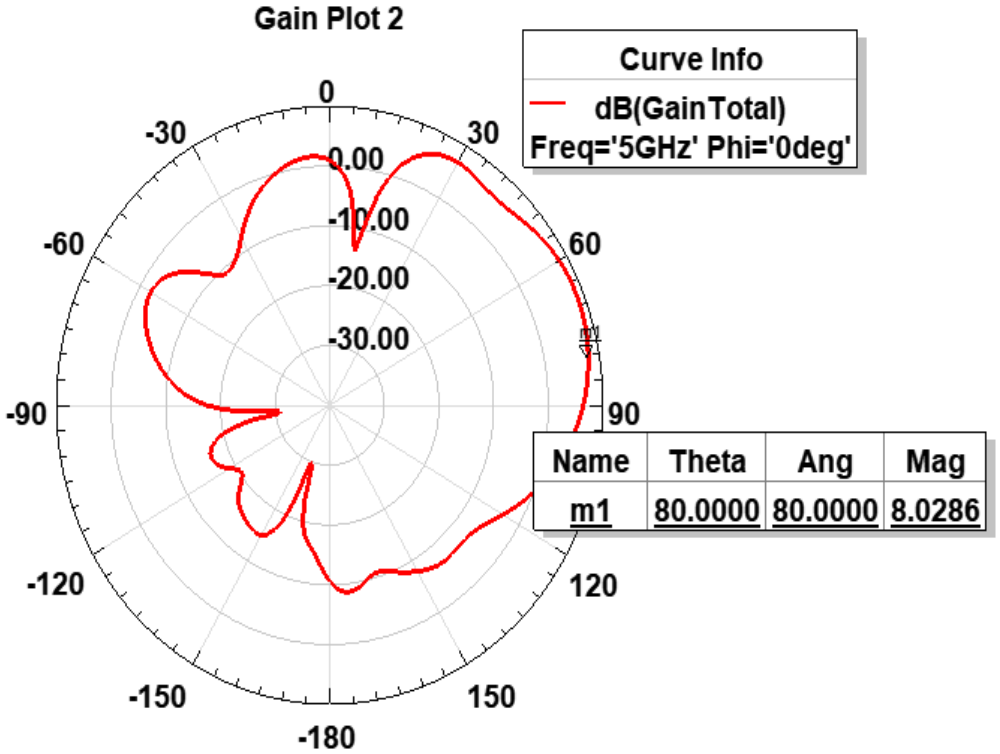

Figure 5.32 E principal plane gain plot for vertical dielectric wedges with right element excited

5.8 Beamsteering angle control using vertical dielectric wedges

Beamsteering is one of the most important performance features of the beamforming topology. To achieve the control of beamsteering angles, a straightforward has been demonstrated and analyzed. Beamsteering angles can be controlled by varying the tilt angles of the vertical dielectric wedges. The plots for tilt angles of 0 degrees, 10 degrees, 20 degrees, and 45 degree are shown. The results in section 5.7 are for 20 degrees wedge tilt angles. The dielectric constant of the wedge is kept constant and only the tilt angle is varied.

Figure 5.33 shows the E principal plane gain plots for vertical dielectric wedge with different tilt angles. As seen from the plots the gain of increases and the side lobes decrease as the tilt angles increase. The reason behind such behavior can be explained using flaring of the horn antenna as an example. Similarly, here as the flaring (tilt angles) of the wedges increases; the major part of the aperture becomes available to the middle antenna.

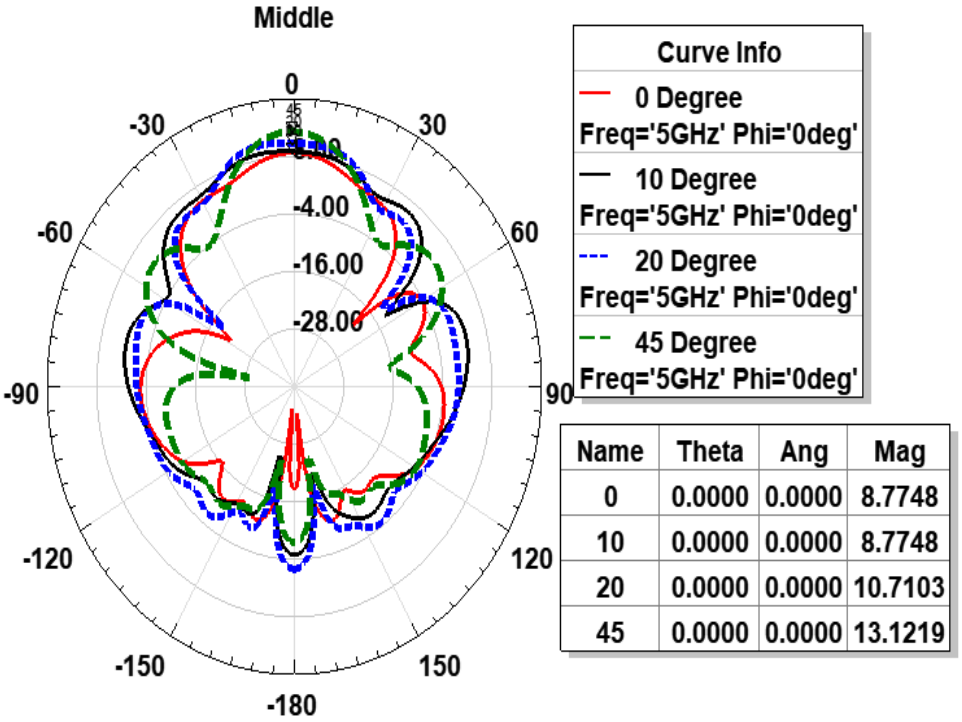

Name	Theta	Ang	Mag
0	0.0000	0.0000	8.7748
10	0.0000	0.0000	8.7748
20	0.0000	0.0000	10.7103
45	0.0000	0.0000	13.1219

Figure 5.33 E principal plane gain plots for vertical dielectric wedge with different tilt angles when middle antenna is excited

Figures 5.34 and 5.35 shows the right and left beamsteering gain plots for tilt angles of 0 degrees, 10 degrees, 20 degrees, and 45 degrees. The results in section 5.7 are for 20 degrees wedge tilt angles. The dielectric constant of the wedge is kept constant and only the tilt angle is varied. As seen from figures 5.34 and 5.35, as the tilt angles increases, the beamsteering angle increases but the gain decreases. Once again referring to the horn antenna angle example, as the flaring (tilt angles) of the wedges increases; the aperture availability for the left and right antenna decreases which in turn reduces the gain.

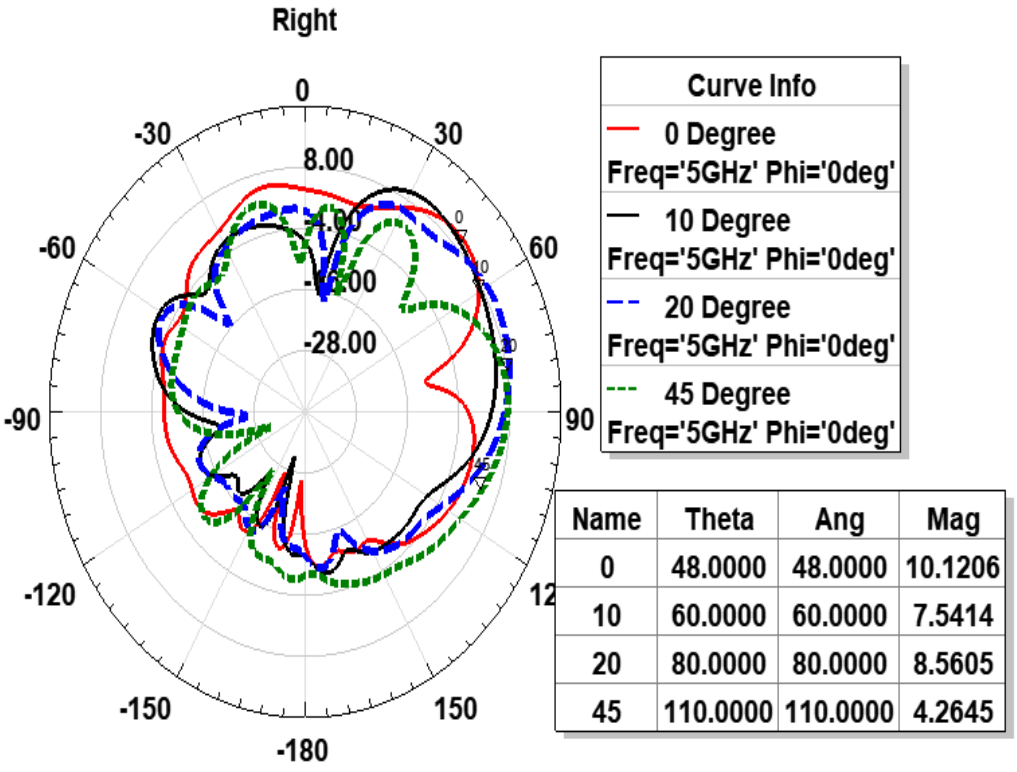

Figure 5.34 E principal plane gain plots for vertical dielectric wedge with different tilt angles when right antenna is excited

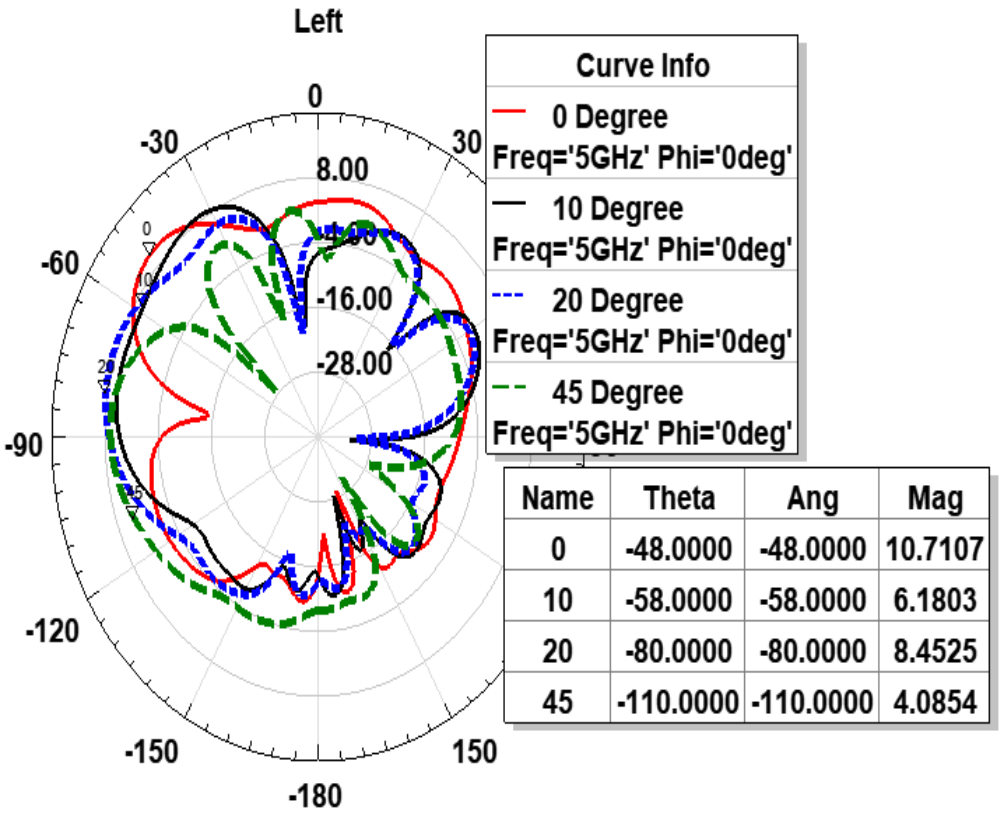

Figure 5.35 E principal plane gain plots for vertical dielectric wedge with different tilt angles when left antenna is excited

5.10 Comparison of Different Proposed Structures

TYPE	ADVANTAGES	DISADVANTAGES
Horizontal Dielectric Wedges	• Easy to implement. • Less computationally intensive	• Beamsteering angle control is complex. • Design gets complicated for larger arrays. • Every time the dielectric constant of wedge changes matching layers will be changed. • Design requires high dielectric constant material which makes the design heavy.

Dielectric Slabs	• Easy to implement for small arrays • Less computationally intensive.	• Middle antenna is very sensitive to dielectric slab properties. • Matching layers do not improve impedance matching issue. • Beamsteering angle control is complex for larger arrays. • Design gets too complicated for large arrays. • Not easily scalable
Plano Concave lens	• Beamsteering angle control is easier to achieve. • Impedance matching issues can be solved using matching layers.	• Extremely long simulation time. • The lens can get heavy and bulky. • Design gets complicated for large arrays.
Vertical Wedges	• No impedance matching layer is needed. • Easily extended for large antenna arrays. • Beamsteering angle control is easier to achieve. • Computationally less	• Wedges can get bulky as the dielectric constant increases.

	intensive.	

Table 5.1: Comparison of different proposed quasi-optical structures

STRUCTURE TYPE	SIMULATION TIME	MEMORY REQUIRED
Horizontal Wedges	8 mins	3.3 GB
Dielectric Slabs	18 mins	7.8 GB
Plano Concave Lens	8.5 hours	24.6 GB
Vertical Wedges	8 mins	3.2 GB

Table 5.2: Simulation time and memory requirements for different quasi-optical structures

5.11 Validation of Results

All of the simulations provided so far have been performed using Ansys HFSS; to validate the results CST microwave studio (CST MWS) has been used. CST uses the finite difference time domain (FDTD) technique. One of the most important reasons to use CST for validation is because of its use of a broadband signal to feed the structure. This type of technique simulates the structure just once to calculate the scattering parameters over the desired frequency range, and radiation patterns are

calculated at selected frequencies. This is in contrast to HFSS which uses a frequency domain solver to perform simulations for each frequency sample. This is a reason time domain solver are a bit slower than frequency domain solvers for a smaller number of frequency points.

5.11.1 Horizontal Wedge

This is the first design explored. Figure 5.36 shows the gain plots from HFSS and CST for the middle antenna. The data from HFSS and CST has been imported in MATLAB for comparison. The blue curve shows the plot from HFSS and the red curve shows the plot from CST. As seen from the figure results from both the simulation softwares are in good agreement. Similarly figures 5.37 and 5.38 show favorable comparisons when right and left antennas are excited, respectively.

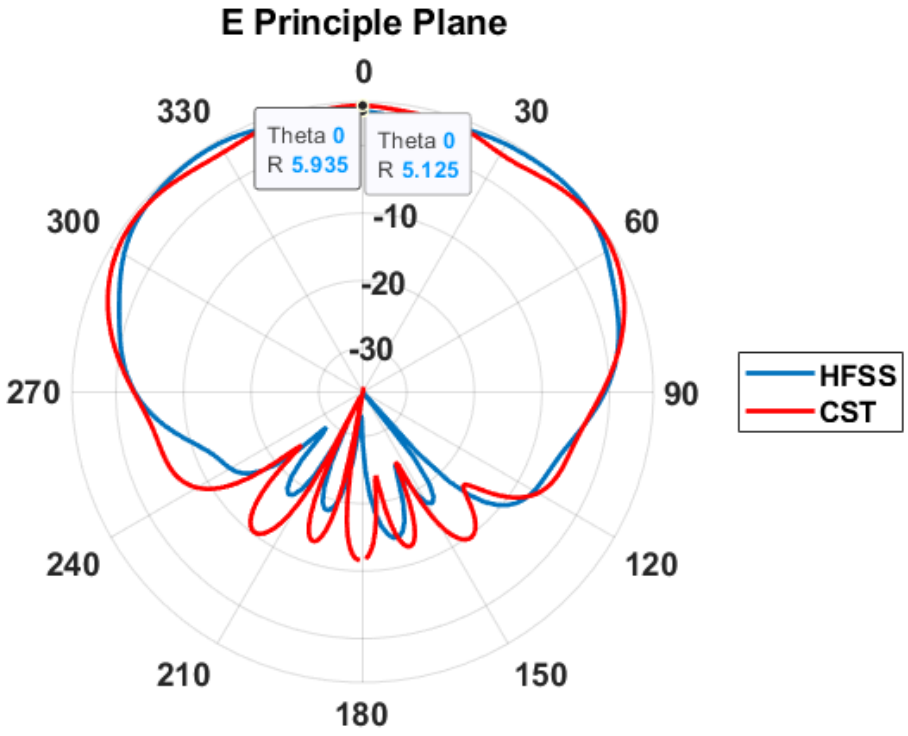

Figure 5.36 Comparison gain plot for horizontal dielectric wedge when middle antenna is excited

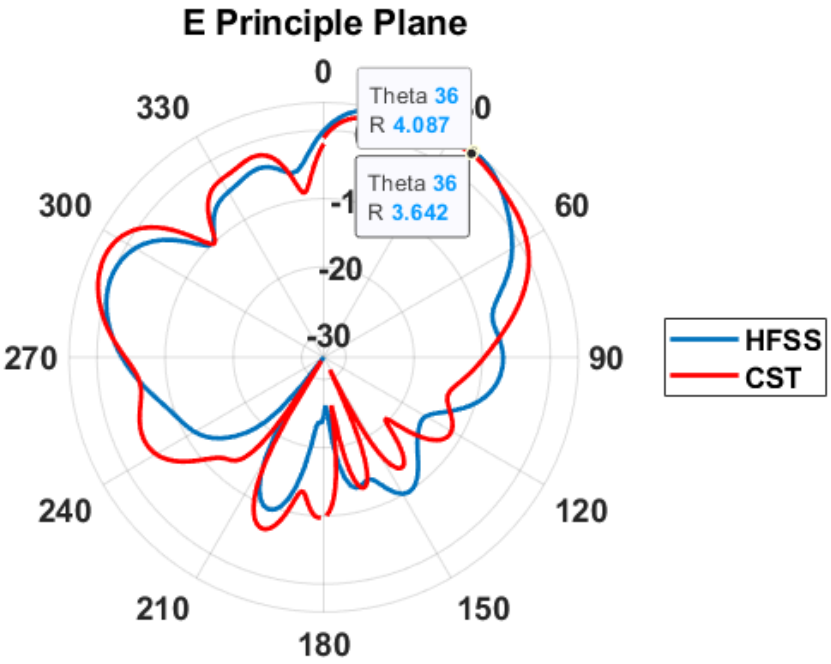

Figure 5.37 Comparison gain plot for horizontal dielectric wedge when right antenna is excited

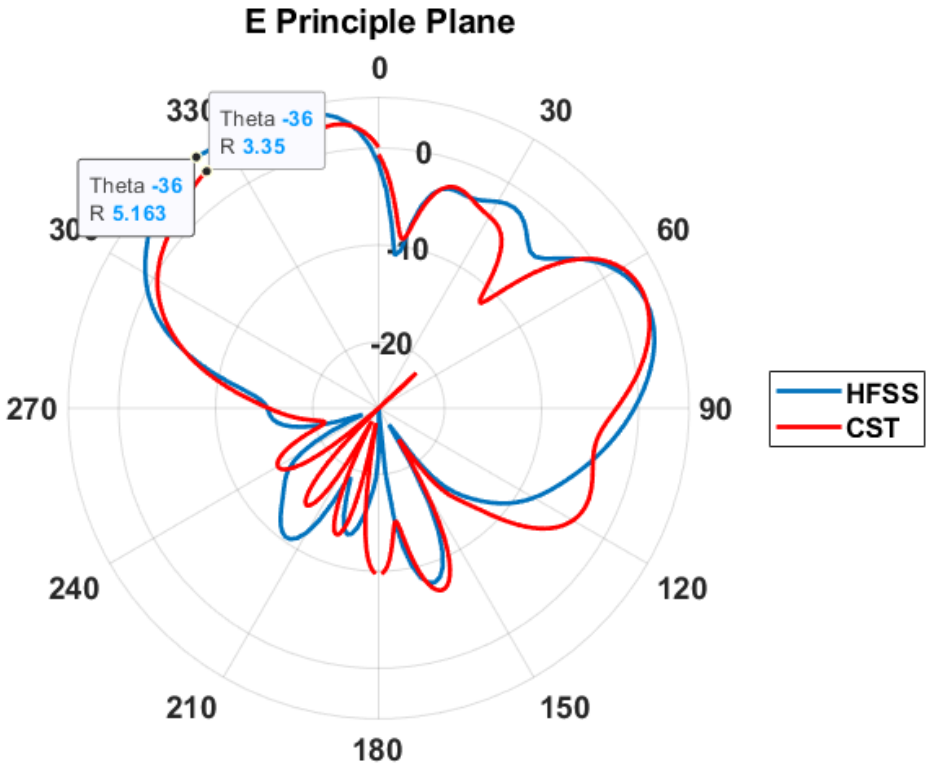

Figure 5.38 Comparison gain plot for horizontal dielectric wedge when left antenna is excited

5.11.2 Dielectric Slabs

This is the second design explored. Figure 5.39 shows the gain plots from HFSS and CST for the middle antenna. The blue curve shows the plot from HFSS and the red curve shows the plot from CST. As seen from the figure results from both simulation softwares are in good agreement. Similarly figures 5.40 and 5.41 show favorable comparison plots when right and left antennas are excited, respectively.

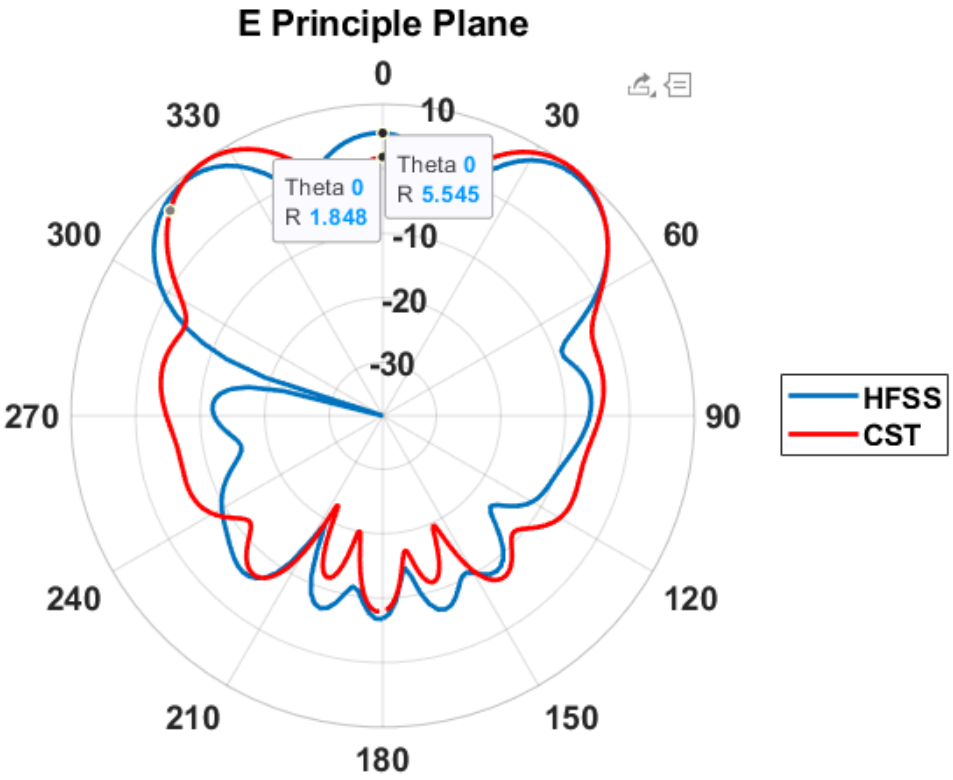

Figure 5.39 Comparison gain plot for dielectric slab when middle antenna is excited

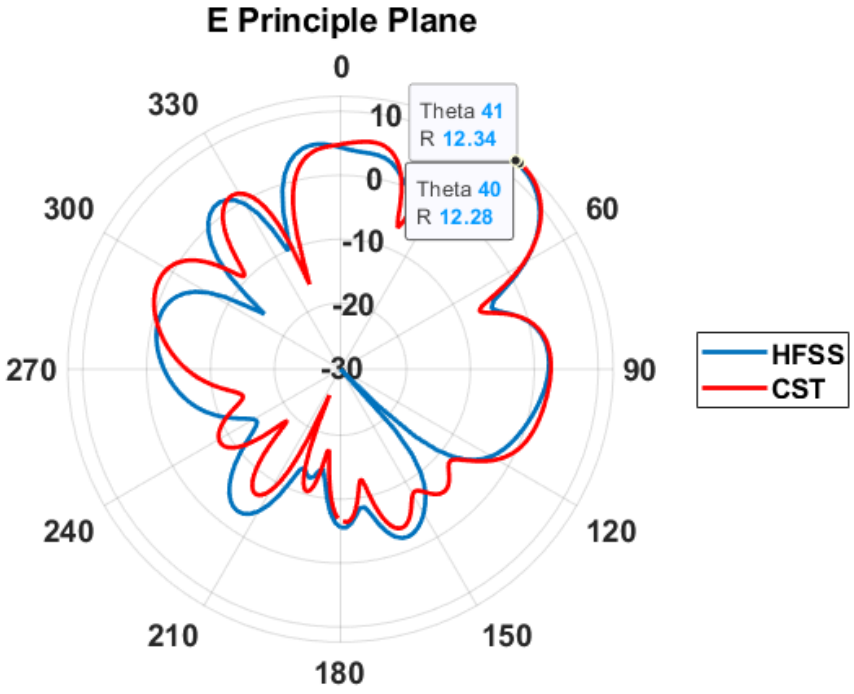

Figure 5.40 Comparison gain plot for dielectric slab when right antenna is excited

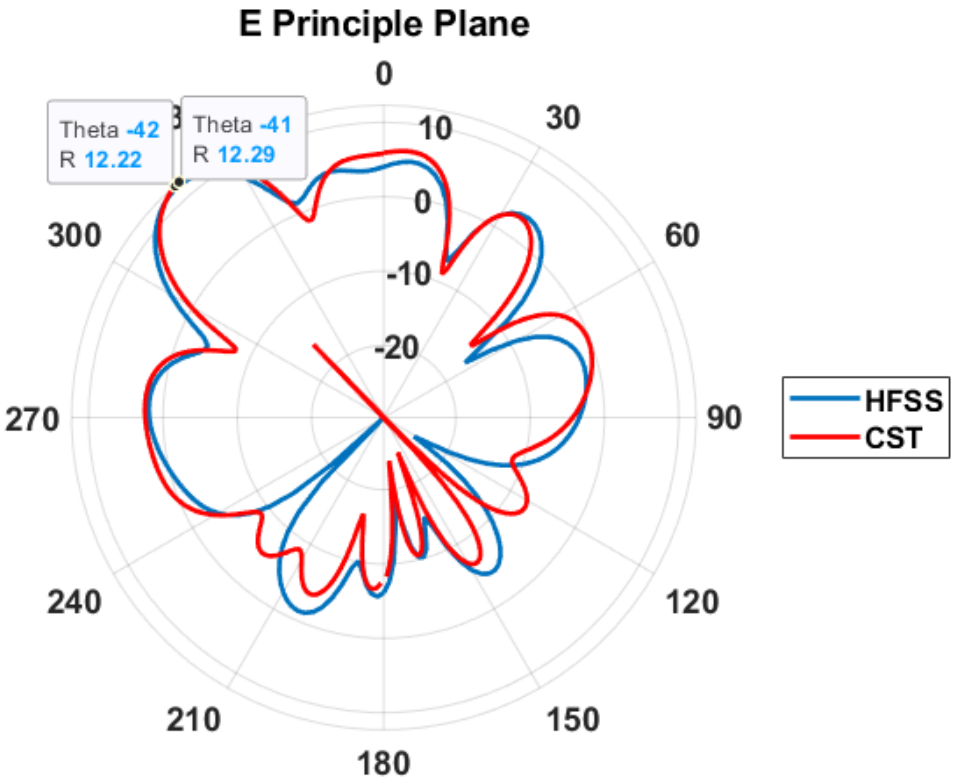

Figure 5.41 Comparison gain plot for dielectric slab when left antenna is excited

5.11.3 Plano-Concave Lens

This is the third design explored. Figure 5.42 shows the gain plots from HFSS and CST for the middle antenna. The blue curve shows the plot from HFSS and the red curve shows the plot from CST. As seen from the figure 5.42 results from both the simulation softwares are in substantial agreement, although not as close as other cases shown. Similarly figures 5.43 and 5.44 show favorable comparison plots when right and left antennas are excited respectively.

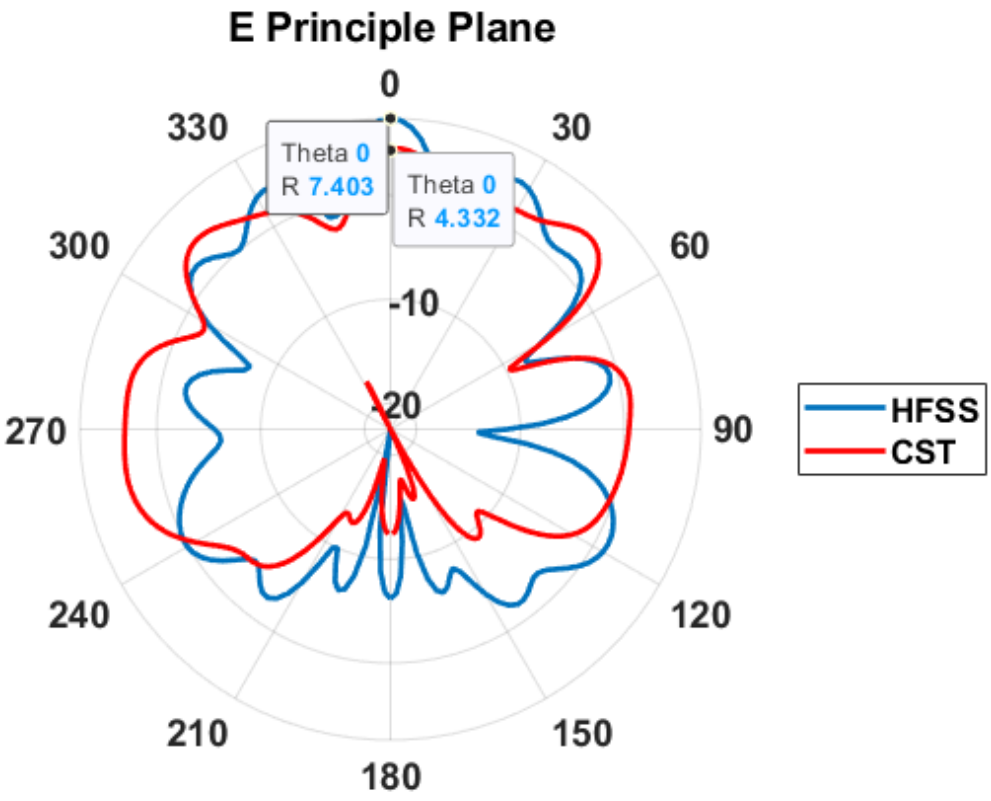

Figure 5.42 Comparison gain plot for plano-concave lens when middle antenna is excited

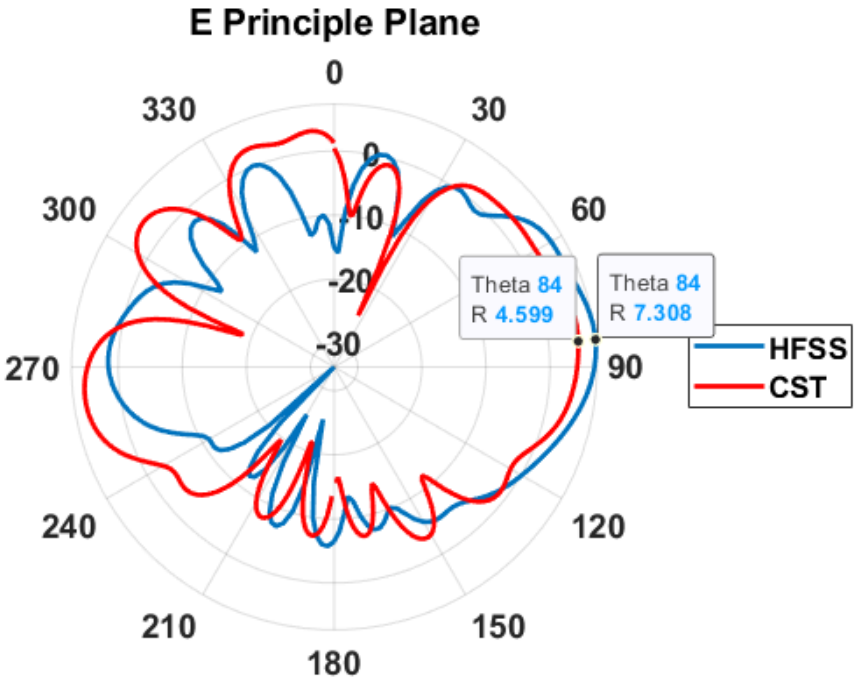

Figure 5.43 Comparison gain plot for plano-concave lens when right antenna is excited

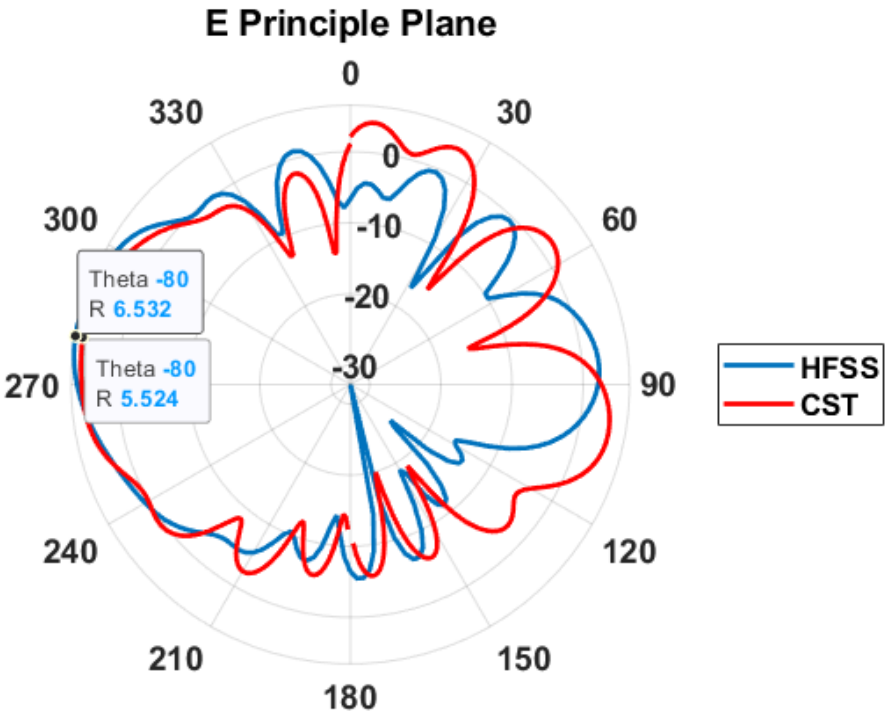

Figure 5.44 Comparison gain plot for plano-concave lens when left antenna is excited

5.11.4 Vertical Dielectric Wedge

This is the last design explored. Figure 5.45 shows the gain plots from HFSS and CST for the middle antenna. The blue curve shows the plot from HFSS and the red curve shows the plot from CST. As seen from the figure results from both the simulation softwares are in good agreement. Similarly figures 5.46 and 5.47 show favorable comparisons when right and left antennas are excited, respectively.

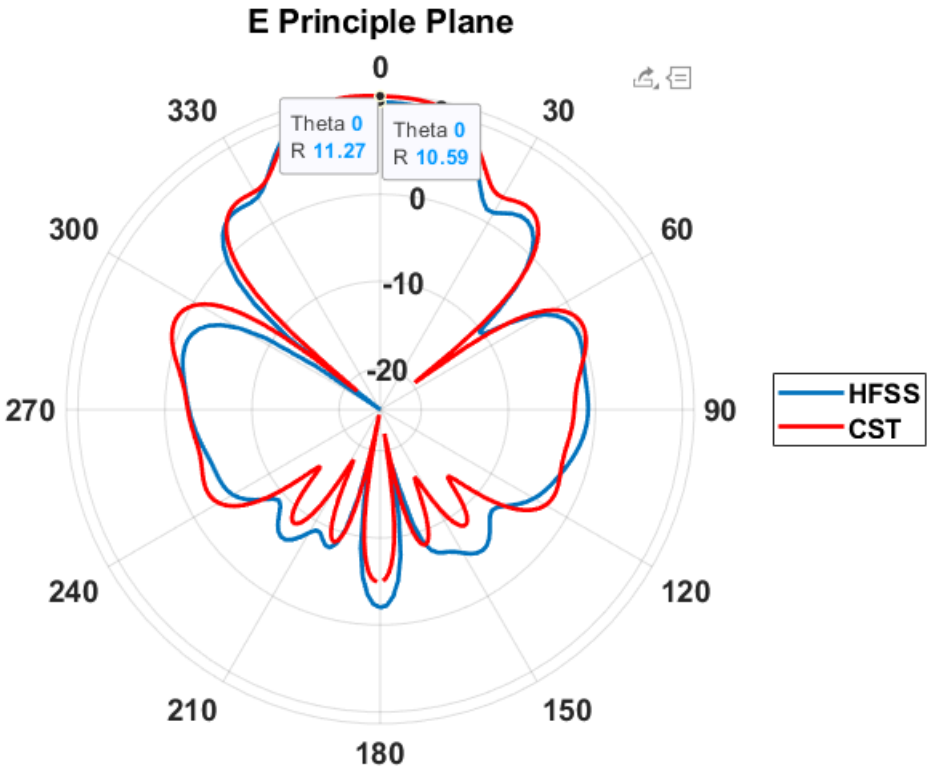

Figure 5.45 Comparison gain plot for vertical dielectric wedge when middle antenna is excited

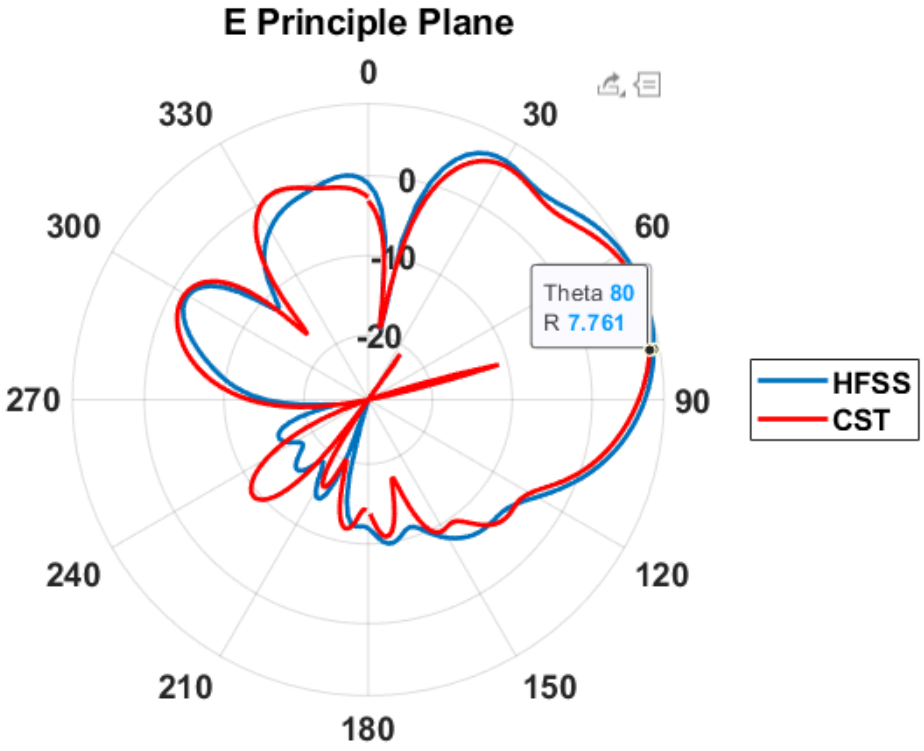

Figure 5.46 Comparison gain plot for vertical dielectric wedge when right antenna is excited

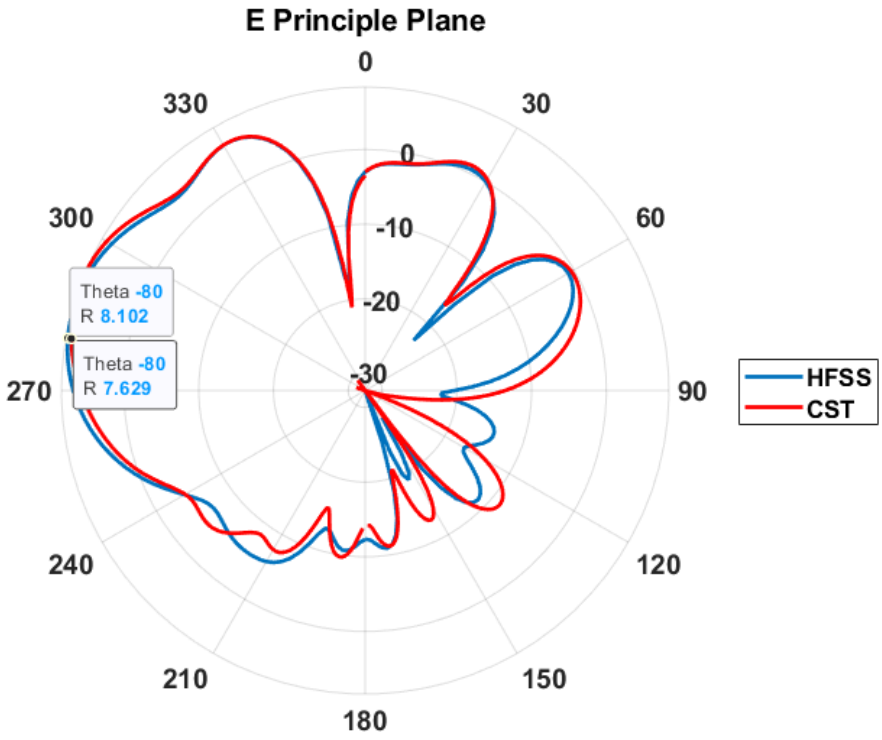

Figure 5.47 Comparison gain plot for vertical dielectric wedge when left antenna is excited

CHAPTER 6

BANDWIDTH CONSIDERATIONS AND SCALABILITY

6.1 Introduction

In chapter 5 performance of the selected candidate structures has been discussed and presented in some detail, including advantages and limitations associated with each structure. However, there are other important considerations which must be made in assessing the utility of the structures in particular related to bandwidth and scalability.

6.2 Effects on Bandwidth

Various methods have been incorporated to increase the bandwidth of the patch antenna. For example, lowering the Q-factor of the patch, by a low dielectric substrate, introducing slots in the patch or by using a thick dielectric substrate. Researchers have also used defected ground planes or partial ground planes to improve the front to back ratio and suppress surface waves resulting in bandwidth enhancement. To evaluate the effects of vertical dielectric wedges on bandwidth; a 1x3 antenna is designed on a thick and a low dielectric substrate as shown in figure 6.1. The substrate has a thickness of 1.6 mm and a dielectric constant of 1.0. As seen from the figure 6.2 S parameter plot the bandwidth of is 170 MHz which is 3.4%. In this section a study is carried out to check the effects on bandwidth by introducing the vertically oriented dielectric wedges.

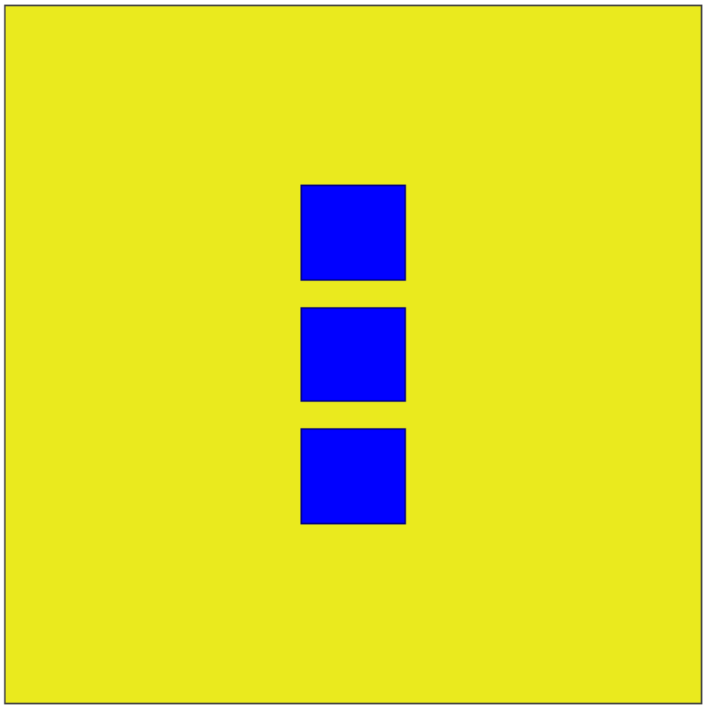

Figure 6.1 1x3 Patch Antenna on thick and low dielectric substrate

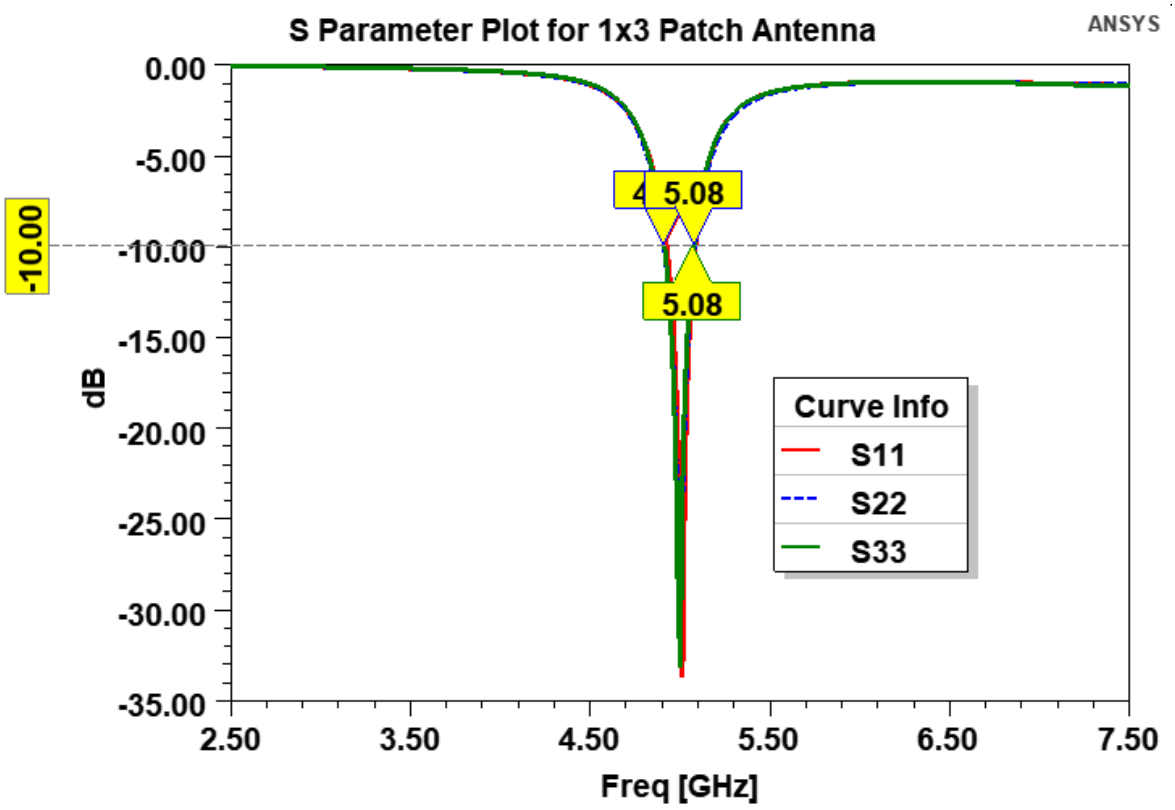

Figure 6.2 S parameter plot of 1x3 Patch Antenna on thick and low dielectric substrate

Figure 6.3 shows the dielectric wedges placed on top of the patch antenna with thick and low dielectric substrate. The structure was simulated in HFSS using absorbing boundary conditions. This figure shows the arrangement of antenna and dielectric wedges for E principal plane. The wedge tilt angle is kept at 20 degrees and Roger duroid 6810 substrate is used as the wedge. The dielectric constant is 10.2 and the loss tangent is 0.0009.

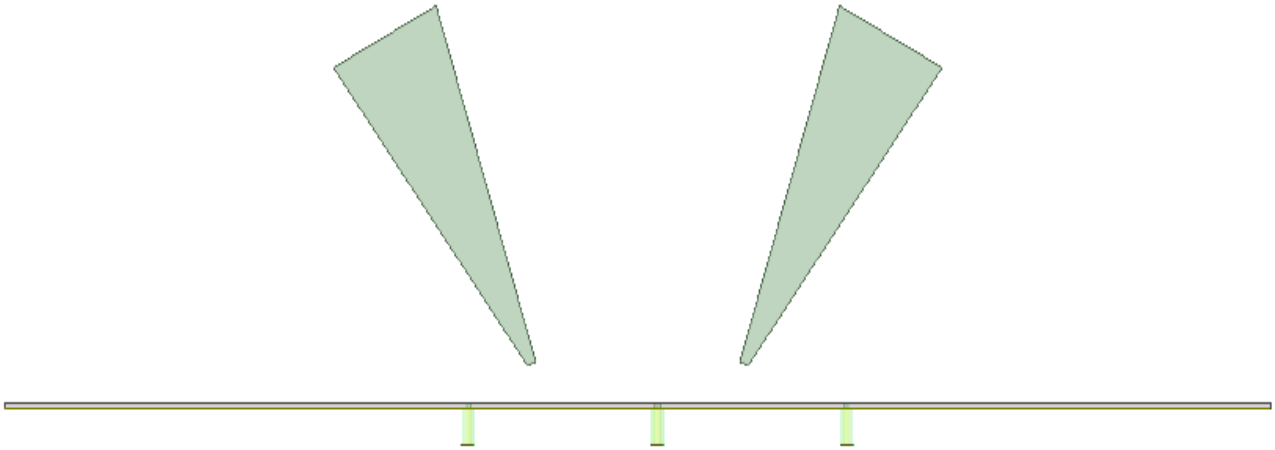

Figure 6.3 Dielectric Wedges along with patches on thick and low dielectric substrate

Figure 6.4 shows the E principal plane gain plots for thick and low dielectric substrate when all the elements are excited. Not much change is seen from the gain plot when compared to the gain plot in figure 5.27. Figure 6.5 shows the S parameter plot where S11 is for the middle antenna, S22 is for the left antenna and S33 is for the right antenna. As seen from this figure the impedance matching is good for the entire design. The S11 plot is highlighted to show the marker readings; the bandwidth can be calculated as 220 MHz, which shows a considerable improvement of 4.4% in the bandwidth. The vertical wedge structure does not exhibit behaviors that would appear to limit bandwidth for a modest bandwidth antenna, however further study would be needed for wider bandwidth antenna elements.

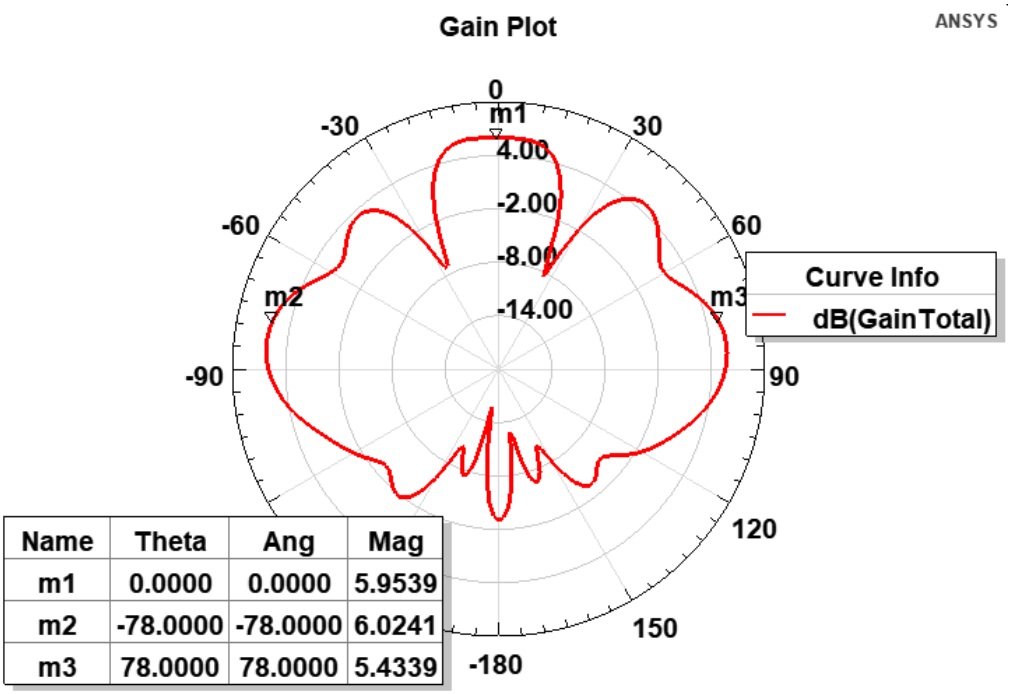

Figure 6.4 E principal plane gain plots for thick and low dielectric substrate when all the elements are excited

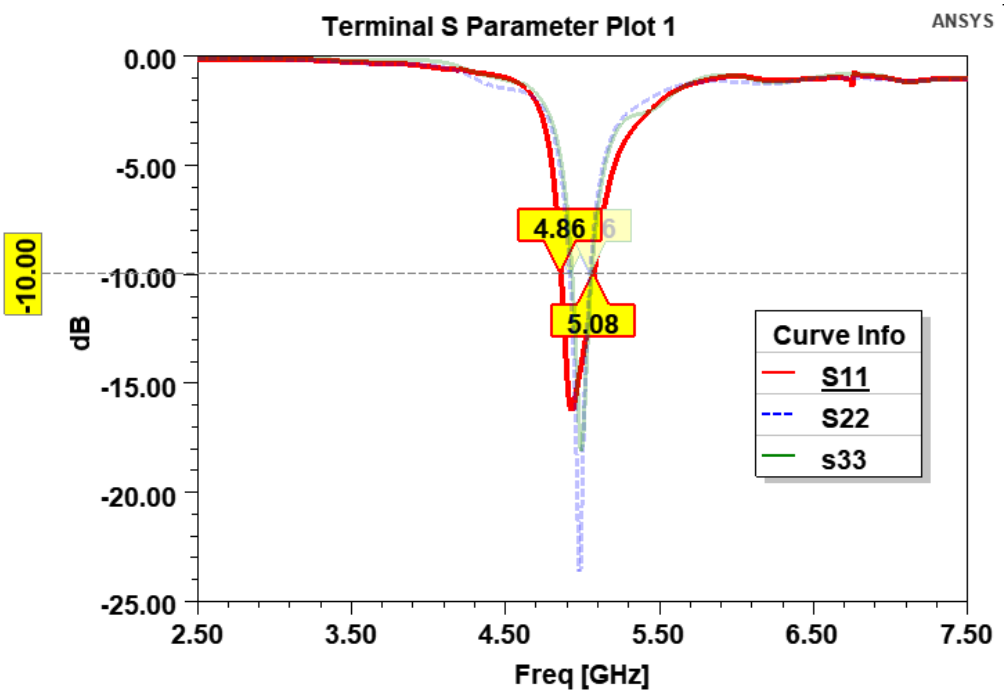

Figure 6.5 S parameter plot of 1x3 Patch Antenna with dielectric wedges on thick and low dielectric substrate

6.3 Scalability

In many communication devices adaptive beamforming antennas are used in order to improve the system performance, reliability and adaptiveness. Unlike fixed antenna systems, adaptive antennas can adjust their beam shapes and radiation patterns. Ability to satisfy application needs in terms of beam gains and adaptability in part depends on how effectively the beamformer can scale to larger 1- and 2-dimensional arrays. In this section the ability to scale to larger than 1x3 linear arrays as well as to 2-dimensional arrays is evaluated for the case of vertically oriented dielectric wedges. The ability to scale to larger linear arrays is evaluated to analyzing performance with additional antenna elements and wedges. The ability to extend to 2-dimensional case is considered by ensuring beamforming operation in H-principal plane, in addition to E-principal plane studies are discussed in earlier sections.

Figure 6.6 shows the arrangement of dielectric wedges for a 5x1 microstrip patch antenna. The structure was simulated using absorbing boundary conditions. Two different size wedges are placed on top of the antenna elements. All wedges are made of Rogers duroid 6810 with dielectric constant of 10.2 and loss tangent of 0.0009. The size of the wedges is carefully designed to obtain five distinct minimally overlapping beams. The tilt angle of the orange wedges is 15 degrees, and the tilt angle of the green wedges is 30 degrees. This is designed in such a way that the L1 (first left) antenna and R1 (first right) antenna have sufficient spatial opening to radiate the beam in the required direction. The size of the middle wedges which are denoted with orange color are made large in order to get a distinct beams from antenna elements L1 and R1. If the wedge sizes are kept same there will be reflections between two wedges which will result in loss of transmitted signal.

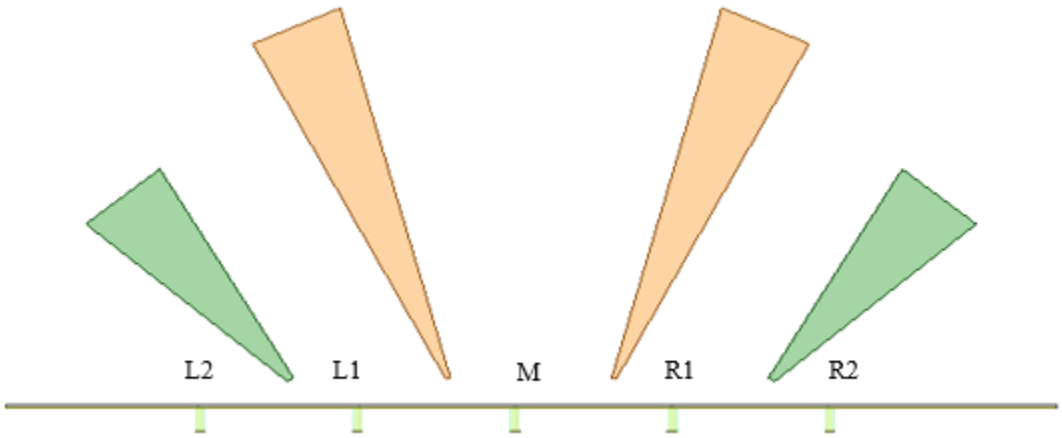

Figure 6.6 Vertical dielectric wedges placed on 5x1 antenna

Beams from each antenna can be steered according to the tilt angles of the wedges. Figure 6.7 shows the E principal plane gain plot for vertical dielectric wedges placed on a 5x1 antenna array. Five minimally overlapping beams are formed. Figure 6.8 shows the S parameter plots for all of the antennas in an array. As seen from the figure impedance matching of all the antennas is good.

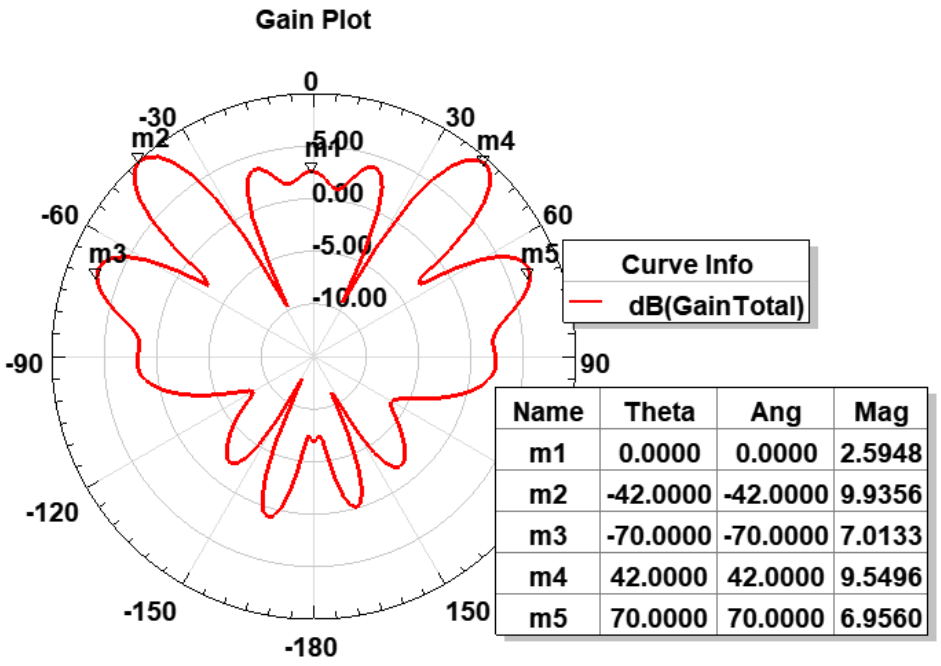

Figure 6.7 E principal plane gain plot for vertical dielectric wedges placed on 5x1 antenna

Figures 6.9 – 6.13 show gain plots for E principal plane with each element being excited individually. As seen from figure 6.9 the gain of 0.9857 dB with zero beamsteering is achieved when only the middle element is excited. The beam is directive, but it creates two grating and side lobes at different angles. This is caused due to the diffraction occuring at the edges of the middle two wedges (orange color).

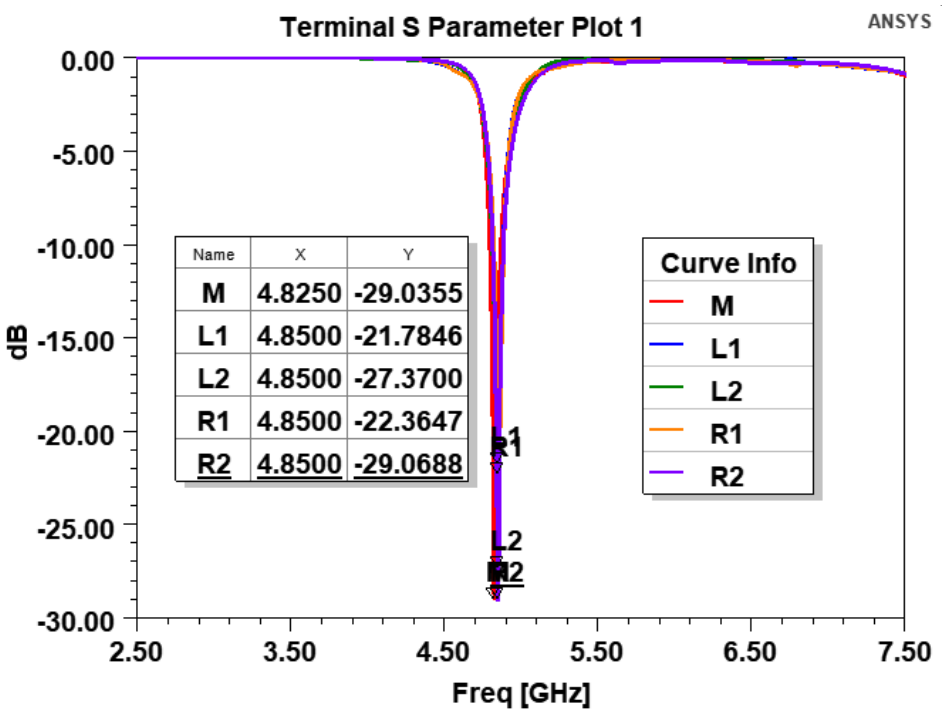

Figure 6.8 S Parameter Plot for vertical dielectric wedges placed on 5x1 antenna

Figure 6.10 shows the gain plot of the first right element and a gain of 10.4481 dB with 42 degrees beamsteering achieved when only the first right element is excited. Figure 6.11 shows the gain plot of the second right element and a gain of 10.2028 dB with 70 degrees beamsteering achieved when only the second right element is excited. Figure 6.12 shows the gain plot of the first left element and a gain of 10.2488 dB with -42 degrees beamsteering achieved when only the first left element is excited. Figure 6.13 shows the gain plot of the second left element and a gain of 10.8032 dB with -70

degrees beamsteering achieved when only the second right element is excited. The steering angle can be varied by changing the dielectric wedge tilting angles which is explained in section 5.8.

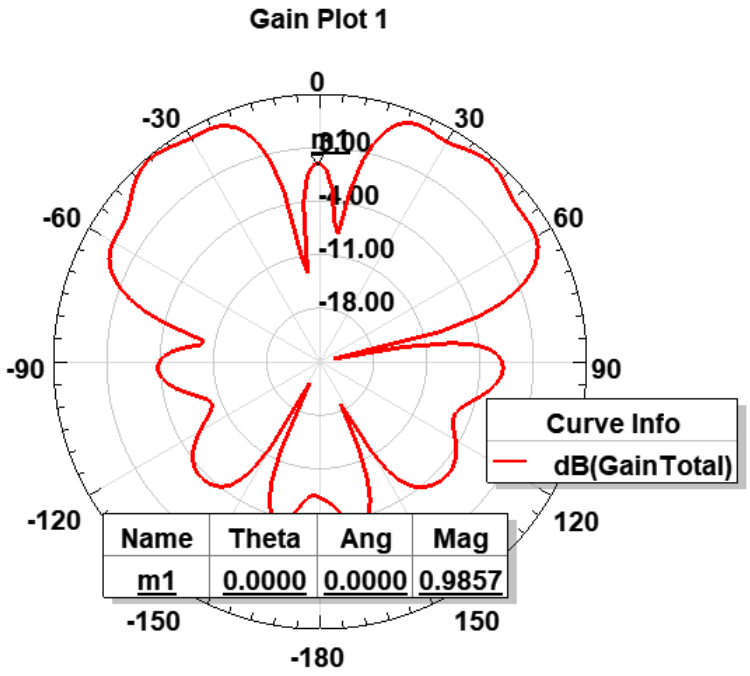

Figure 6.9 E principal plane gain plot for vertical dielectric wedges placed on 5x1 antenna when middle element is excited

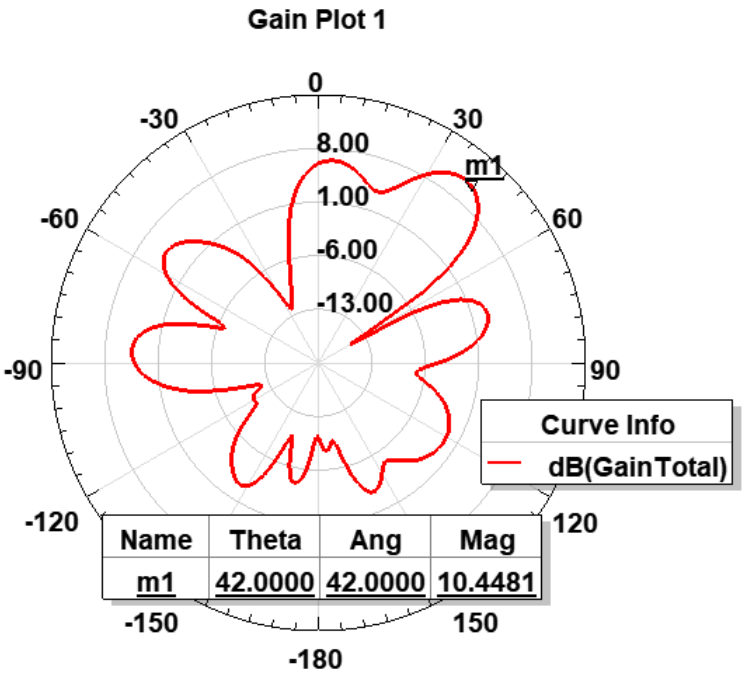

Figure 6.10 E principal plane gain plot for vertical dielectric wedges placed on 5x1 antenna when right 1 element is excited

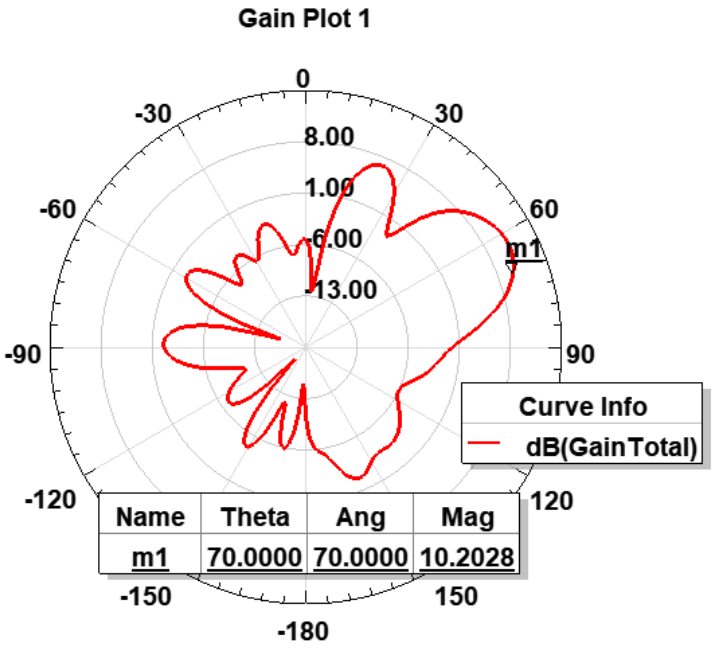

Figure 6.11 E principal plane gain plot for vertical dielectric wedges placed on 5x1 antenna when right 2 element is excited

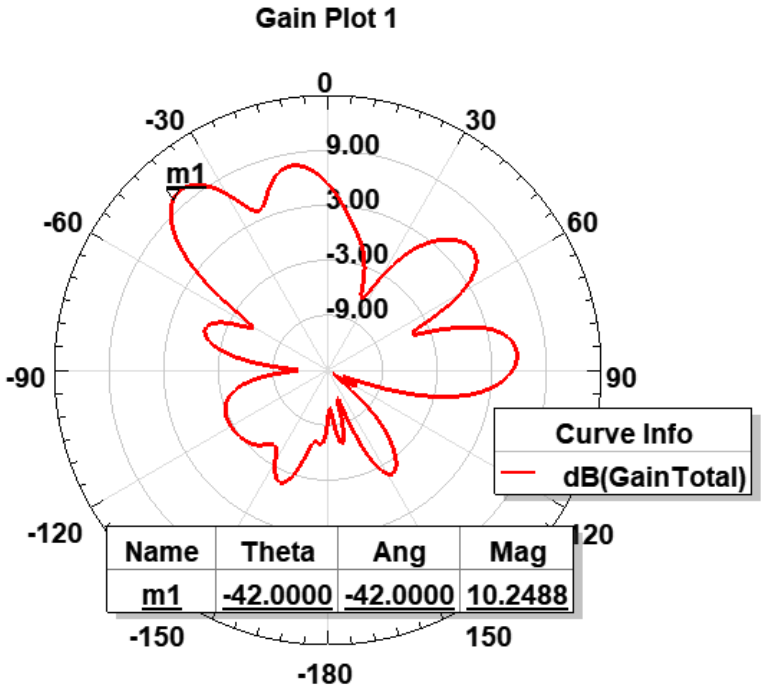

Figure 6.12 E principal plane gain plot for vertical dielectric wedges placed on 5x1 antenna when left 1 element is excited

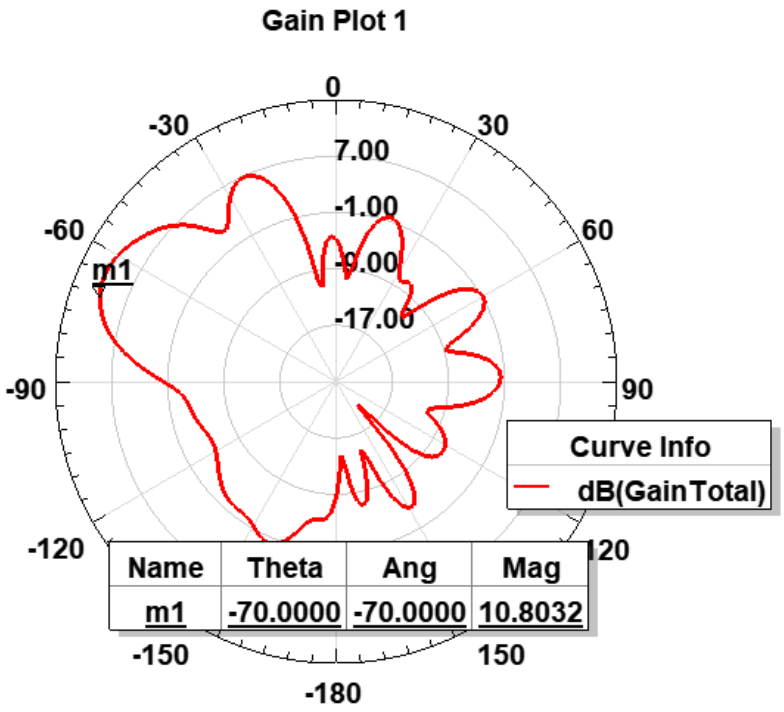

Figure 6.13 E principal plane gain plot for vertical dielectric wedges placed on 5x1 antenna when left 2 element is excited

6.4 H Principal Plane Plots

All the results till now correspond antennas that were designed for E principal plane beamforming. In this section the discussion is focused on the structure for H principal plane. This structure is designed for 3 element antennas, the design consisting of vertical dielectric wedges. The arrangement and angle of vertical wedges is carefully chosen for the middle, left and right antenna in order to achieve distinct beams. The structure was simulated using absorbing boundary conditions. Rogers 5880 is used as the substrate with dielectric constant of 2.2 and loss tangent of 0.0009. And the superstrate/ dielectric wedges is taken to be Rogers 6810 with dielectric constant of 10.2 and loss tangent of 0.0009. Figure 6.14 shows the H principal plane antenna design with vertical dielectric wedges

Figure 6.16 shows the S parameter plot where S11 is for the middle antenna, S22 is for the left antenna and S33 is for the right antenna. As seen from this figure the impedance matching is good for the entire design. This type of structure does not require impedance matching layer since the since there are few reflections from these vertical dielectric wedges. The wedges are placed at 20 degrees tilt angles.

Figure 6.15 shows the electric field plot when all the antenna elements are active. It can be clearly seen that 3 distinct beams are formed which can be confirmed from the gain plots as seen in figure 6.17.

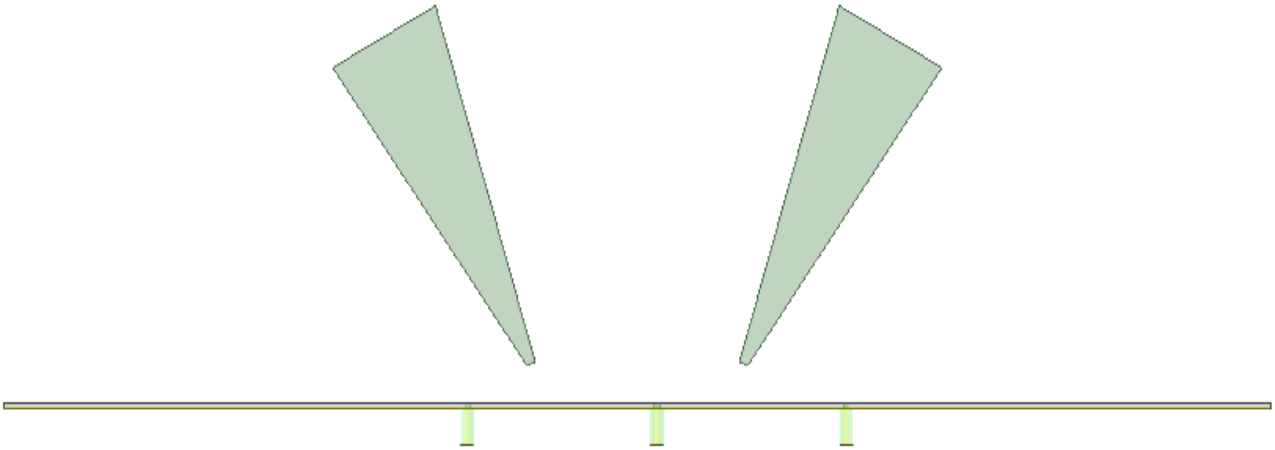

Figure 6.14 H Principal plane antenna design with vertical dielectric wedges

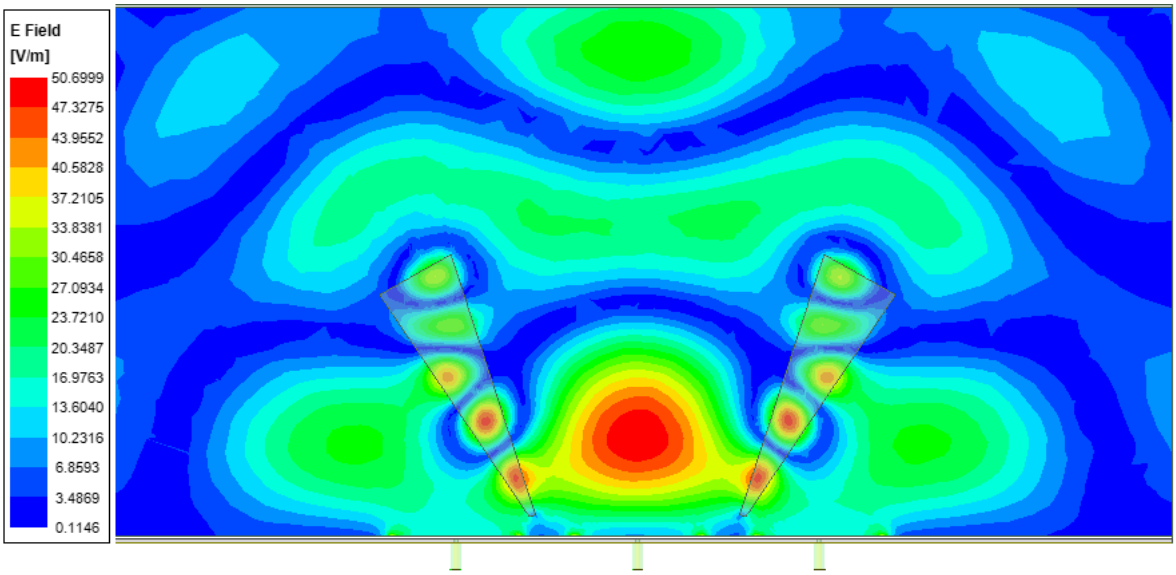

Figure 6.15 Field Plot for H Principal plane antenna design with vertical dielectric wedges

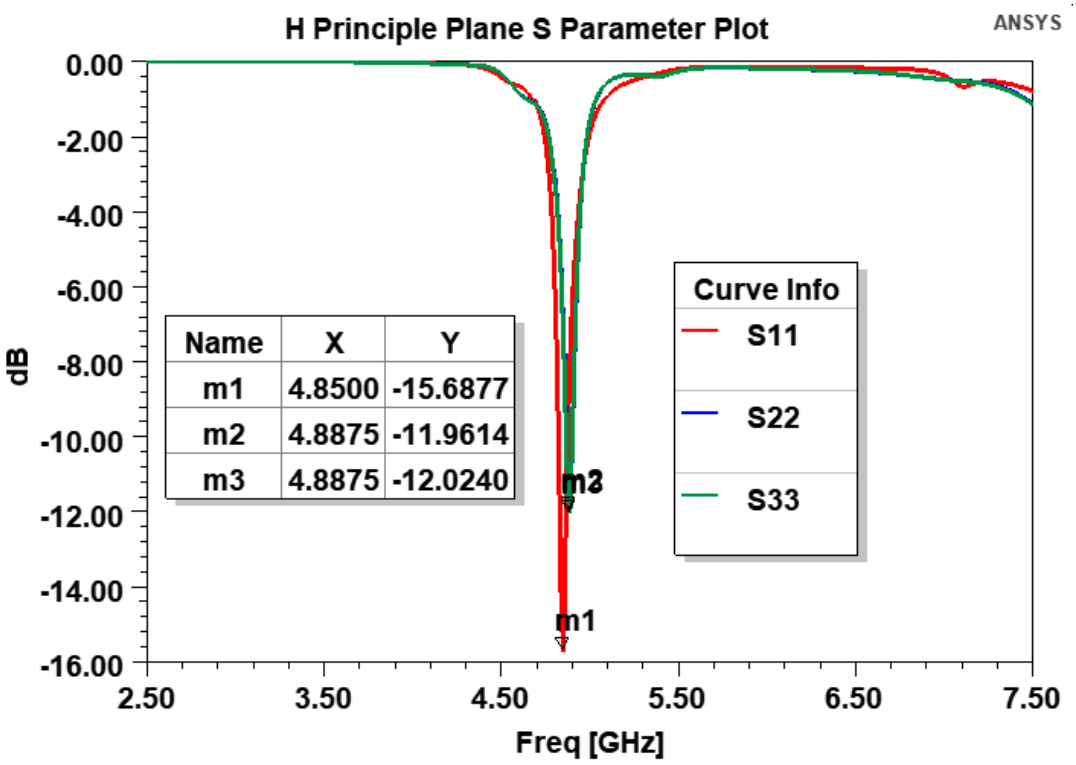

Figure 6.16 H Principal plane S parameter plot for vertical dielectric wedges

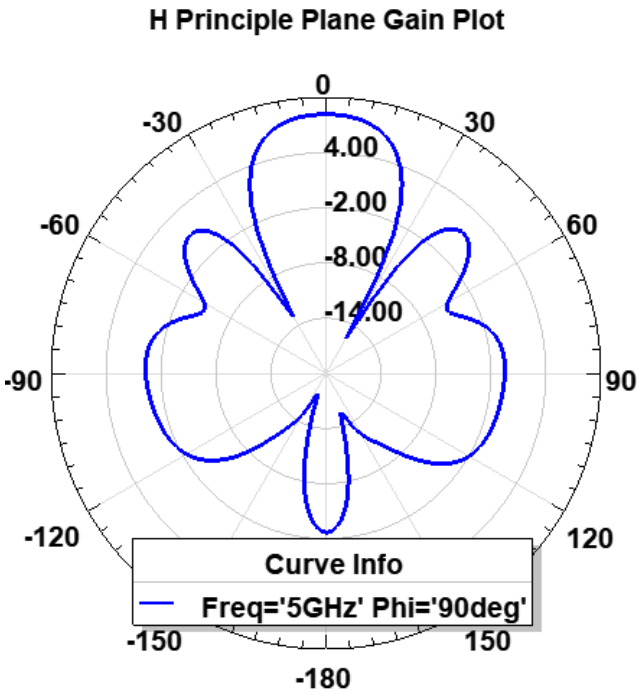

Figure 6.17 H Principal plane gain plot for vertical dielectric wedges when all the elements are excited

Figures 6.18, 6.19 and 6.20 shows the gain plots for H principal plane with middle element excited, right element excited and left element excited respectively. As seen from figure 6.18 the gain of 9.8617 dB with zero beamsteering is achieved when only the middle element is excited. The beam is directive, but it creates two grating and side lobes at different angles. This is caused due to the diffraction effects from the wedges.

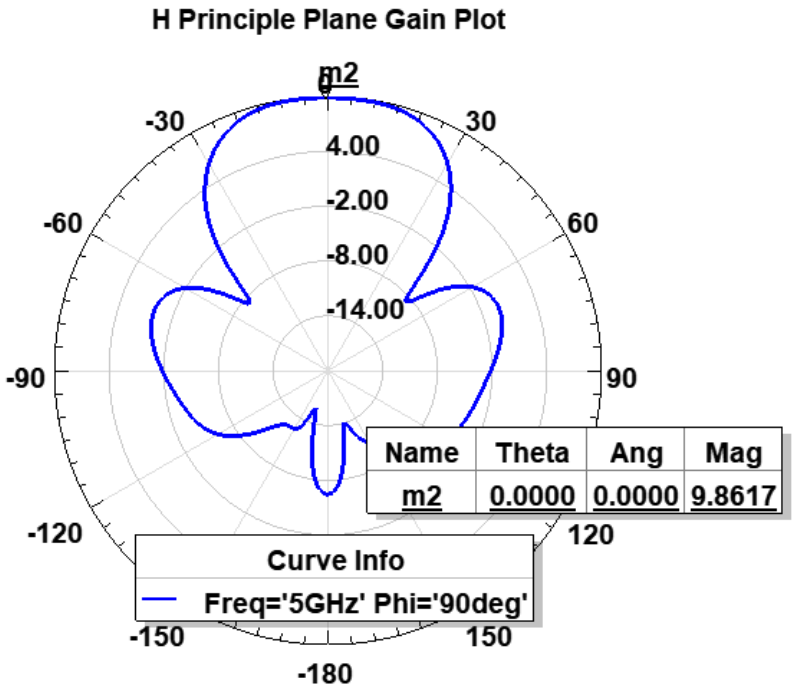

Figure 6.18 H Principal plane gain plot for vertical dielectric wedges when middle element is excited

Figure 6.19 shows the gain plot of left element and a gain of 7.2108 dB with -38 degrees beamsteering achieved when only the left element is excited. Figure 6.20 shows the gain plot of right element and a gain of 7.1766 dB with 38 degrees beamsteering achieved when only the right element is excited. The steering angle can be varied by changing the dielectric wedge tilting angles which is explained in section 5.8.

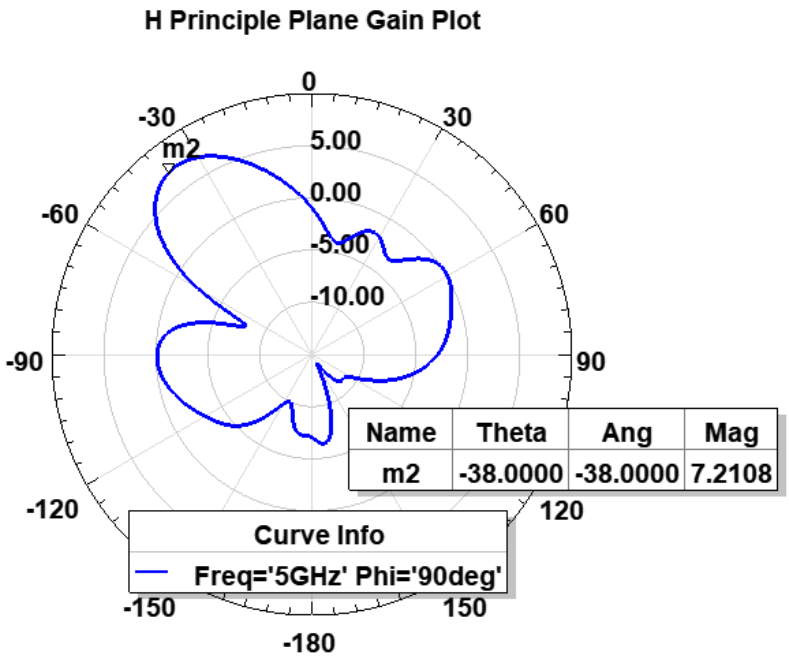

Figure 6.19 H Principal plane gain plot for vertical dielectric wedges when left element is excited

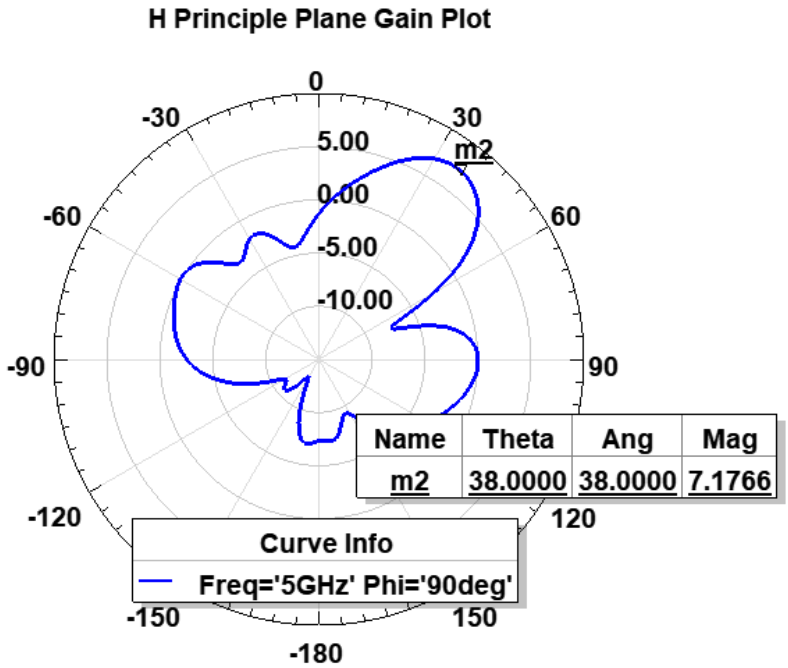

Figure 6.20 H Principal plane gain plot for vertical dielectric wedges when right element is excited

SUMMARY AND CONCLUSION

In this dissertation several techniques have been explored to advance the state of the art of quasi-optical beamforming techniques. These techniques introduce different structures using an array of microstrip patch antennas along with horizontal and vertical dielectric wedges, planoconcave lens and half convex lens like arrangements for the investigation.

To summarize the effects of each quasi-optical structure a comparison table is presented below. This table compares different performance tradeoffs estimations of digital beamforming (the most commonly used beamforming approach currently) and quasi-optical beamforming structures.

Geometries / **Properties**	**Digital Beamformer**	**Quasi Optical Beamformers (Based on studies with few element microstrip patch arrays)**			
		Horizontal Wedge	**Dielectric Slab**	**Plano Concave Lens**	**Vertical Wedge**
Gain	Array size dependent	$\sim 5\ dB$	$\sim 10\ dB$	$\sim 7\ dB$	$\sim 12\ dB$
Bandwidth	Narrow band	Wide BW	Wide BW	Wide BW	Wide BW
Operating Frequency	Low mmWave	> High mmWave	> High mmWave	> High mmWave	> High mmWave
Beamscanning Angle	140°	70°	80°	180°	180°
Scalability	Achievable with more complex digital	Tested to 1x5	Tested to 1x3	Estimated to 3x3	Estimated to 7x7

	processing				
3dB Beamwidth	Array size dependent	23.12°	18.83°	54.29°	54.43°
Sidelobe Level	Less than -10dB	Less than -5 dB	Less than -dB	Less than 2dB	Less than 2dB
Power Required	High	None	None	None	None
Cost and Complexity	Expensive and complex	Relatively inexpensive and low complexity	Relatively inexpensive and low complexity	Relatively inexpensive and low complexity	Relatively inexpensive and low complexity

Performance Tradeoffs Estimation Table

In summary, the following contributions are presented in this dissertation.

- Different types of structures along with their electrical properties and geometries have been studied to obtain the beamsteering angle control. The wedge type of superstrate is the least complex structure to implement, and it gives full control of beamsteering angles in E and H principal plane.
- Partially reflective surfaces were designed using BCSRR to obtain the beamsteering angle control for E and H principal plane. Scanning angles of 40° have been achieved.
- Vertical BCSRR were designed and implemented along with the patch antenna for E and H principal plane. With these types of structures, full control of the beamsteering angles is achieved. Scanning angles of 80° have been achieved.

- Horizontal wedges and matching layers were designed to produce minimally overlapping beams for a 1x3 array of patch antennas. Beamsteering can be controlled by adjusting the dielectric constant and thickness of the wedges.

- Dielectric slabs in the shape of half convex lens were designed; this design improved the gain by 6 dB for the side elements. Beamsteering can be controlled by adjusting the thickness of the slabs, dielectric constant and by use of additional layers.

- Half plano concave lenses were designed. With this design a considerable improvement of impedance matching for the middle antenna element was noticed. Beamsteering control can be obtained by varying the radius of curvature of the lenses.

- The arrangement of vertically oriented dielectric wedges has been placed over the array of patches and three distinct beams have been formed simultaneously. This design improved the gain by 6 dB for the middle antenna element and 4 dB for the side elements.

- The beamsteering angle was controlled by varying the tilt angle of dielectric wedges. The beamscanning angle of 180° was achieved.

- Scalability of the design with vertically oriented wedges was demonstrated for longer linear and 2D arrays.

- Simulations indicated vertically oriented wedges have little effect on bandwidth.

FUTURE WORK

Research conducted in this dissertation pointed to several possible further research directions, including:

- Implementation of tunable partially reflective surfaces to electrically control beamsteering angles.
- Extension of quasi-optical structures to large arrays.
- Implementation of wedges with tunable metamaterial structures to electrically control the beam properties.
- Implementation of quasi-optical structures for antennas with circular polarization.
- Simulating these structures using different electromagnetic simulators that provide spatial field information that can be used to post process the field information at the aperture, for more detailed structural refinement.
- Application of these methods to other distributed type structures.
- Experimentally evaluating these structures for manufacturability.

REFERENCES

[1] Veselago, Viktor G. "Electrodynamics of substances with simultaneously negative and." *Usp. Fiz. Nauk* 92 (1967): 517.

[2] Feresidis, Alexandros P., et al. "Artificial magnetic conductor surfaces and their application to low-profile high-gain planar antennas." *IEEE Transactions on Antennas and Propagation* 53.1 (2005): 209-215.

[3] Erentok, Aycan, Paul L. Luljak, and Richard W. Ziolkowski. "Characterization of a volumetric metamaterial realization of an artificial magnetic conductor for antenna applications." *IEEE Transactions on Antennas and Propagation* 53.1 (2005): 160-172.

[4] Chen, Hou-Tong, Antoinette J. Taylor, and Nanfang Yu. "A review of metasurfaces: physics and applications." *Reports on progress in physics* 79.7 (2016): 076401.

[5] Yu, Nanfang, and Federico Capasso. "Flat optics with designer metasurfaces." *Nature materials* 13.2 (2014): 139-150.

[6] Kildishev, Alexander V., Alexandra Boltasseva, and Vladimir M. Shalaev. "Planar photonics with metasurfaces." *Science* 339.6125 (2013).

[7] Sarabandi, Kamal, and Nader Behdad. "A frequency selective surface with miniaturized elements." *IEEE Transactions on Antennas and Propagation* 55.5 (2007): 1239-1245.

[8] Pendry, John B., et al. "Magnetism from conductors and enhanced nonlinear phenomena." *IEEE transactions on microwave theory and techniques* 47.11 (1999): 2075-2084.

[9] Pendry, John B., David Schurig, and David R. Smith. "Controlling electromagnetic fields." *science* 312.5781 (2006): 1780-1782.

[10] Pendry, John Brian. "Negative refraction makes a perfect lens." *Physical review letters* 85.18 (2000): 3966.

[11] Smith, David R., John B. Pendry, and Mike CK Wiltshire. "Metamaterials and negative refractive index." *Science* 305.5685 (2004): 788-792.

[12] Shelby, Richard A., David R. Smith, and Seldon Schultz. "Experimental verification of a negative index of refraction." *science* 292.5514 (2001): 77-79.

[13] Smith, D. R., et al. "Determination of effective permittivity and permeability of metamaterials from reflection and transmission coefficients." *physical review B* 65.19 (2002): 195104.

[14] Smith, David R., et al. "Composite medium with simultaneously negative permeability and permittivity." *Physical review letters* 84.18 (2000): 4184.

[15] Smith, D. R., et al. "Electromagnetic parameter retrieval from inhomogeneous metamaterials." *Physical review E* 71.3 (2005): 036617.

[16] Baena, Juan Domingo, et al. "Equivalent-circuit models for split-ring resonators and complementary split-ring resonators coupled to planar transmission lines." *IEEE transactions on microwave theory and techniques* 53.4 (2005): 1451-1461.

[17] Marqués, Ricardo, et al. "Comparative analysis of edge-and broadside-coupled split ring resonators for metamaterial design-theory and experiments." *IEEE Transactions on antennas and propagation* 51.10 (2003): 2572-2581.

[18] Marqués, Ricardo, Francisco Medina, and Rachid Rafii-El-Idrissi. "Role of bianisotropy in negative permeability and left-handed metamaterials." *Physical Review B* 65.14 (2002): 144440.

[19] Marqués, Ricardo, Ferran Martin, and Mario Sorolla. *Metamaterials with negative parameters: theory, design, and microwave applications*. Vol. 183. John Wiley & Sons, 2011.

[20] Ekmekci, Evren, et al. "Frequency tunable terahertz metamaterials using broadside coupled split-ring resonators." *Physical Review B* 83.19 (2011): 193103.

[21] Ekmekci, Evren, and Gonul Turhan-Sayan. "Comparative investigation of resonance characteristics and electrical size of the double-sided SRR, BC-SRR and conventional SRR type metamaterials for varying substrate parameters." *Progress In Electromagnetics Research* 12 (2009): 35-62.

[22] Simovski, Constantin R., Pavel A. Belov, and Sailing He. "Backward wave region and negative material parameters of a structure formed by lattices of wires and split-ring resonators." *IEEE Transactions on Antennas and Propagation* 51.10 (2003): 2582-2591.

[23] Cui, Tie-Jun, et al. "A symmetrical circuit model describing all kinds of circuit metamaterials." *Progress In Electromagnetics Research* 5 (2008): 63-76.

[24] Aydin, Koray, et al. "Investigation of magnetic resonances for different split-ring resonator parameters and designs." *New journal of physics* 7.1 (2005): 168.

[25] Aydin, K., and E. Ozbay. "Identifying magnetic response of split-ring resonators at microwave frequencies." *Opto-Electronics Review* 14.3 (2006): 193-199.

[26] Gay-Balmaz, Philippe, and Olivier JF Martin. "Electromagnetic resonances in individual and coupled split-ring resonators." *Journal of applied physics* 92.5 (2002): 2929-2936.

[27] Katsarakis, N., et al. "Electric coupling to the magnetic resonance of split ring resonators." *Applied physics letters* 84.15 (2004): 2943-2945.

[28] Ramakrishna, S. Anantha. "Physics of negative refractive index materials." *Reports on progress in physics* 68.2 (2005): 449.

[29] Numan, Ahmad B., and Mohammad S. Sharawi. "Extraction of material parameters for metamaterials using a full-wave simulator [education column]." *IEEE Antennas and Propagation Magazine* 55.5 (2013): 202-211.

[30] Wang, Jiafu, et al. "A tunable left-handed metamaterial based on modified broadside-coupled split-ring resonators." *Progress In Electromagnetics Research* 6 (2009): 35-45.

[31] Wang, Jiafu, et al. "A controllable magnetic metamaterial: split-ring resonator with rotated

inner ring." *IEEE Transactions on Antennas and Propagation* 56.7 (2008): 2018-2022.

[32] Balanis, Constantine A. *Antenna theory: analysis and design*. John wiley & sons, 2016.

[33] Hansen, Robert C. *Phased array antennas*. Vol. 213. John Wiley & Sons, 2009.

[34] Maharimi, S. F., et al. "Impact of spacing and number of elements on array factor." *Proc. of Progress in Electromagnetics ResearchSymposium* (2012): 1550-1553.

[35] Ehyaie, Danial. *Novel Approaches to the Design of Phased Array Antennas*. Diss. 2011.

[36] Ulaby, Fawwaz T., Eric Michielssen, and Umberto Ravaioli. "Fundamentals of applied electromagnetics 6e." *Boston, Massachussetts: Prentice Hall* (2010).

[37] Rotman, Walter, and R. Turner. "Wide-angle microwave lens for line source applications." *IEEE Transactions on antennas and propagation* 11.6 (1963): 623-632.

[38] Zaghloul, Amir I., and Eric D. Adler. "Compact Rotman lens using metamaterials." U.S. Patent No. 8,736,503. 27 May 2014.

[39] Vashist, Shruti, M. K. Soni, and P. K. Singhal. "A review on the development of Rotman lens antenna." *Chinese Journal of Engineering* 2014.11 (2014): 1-9.

[40] Kilic, O., and S. Weiss. "Dielectric Rotman lens design for multi-function RF antenna applications." *IEEE Antennas and Propagation Society Symposium, 2004.*. Vol. 1. IEEE, 2004.

[41] Dong, Junwei, and Amir I. Zaghloul. "Hybrid ray tracing method for microwave lens simulation." *IEEE transactions on antennas and propagation* 59.10 (2011): 3786-3796.

[42] Schulwitz, Lora, and Amir Mortazawi. "A tray based Rotman lens array with beamforming in two dimensions for millimeter-wave radar." *2010 IEEE International Symposium on Phased Array Systems and Technology*. IEEE, 2010.

[43] Hansen, R. C. "Design trades for Rotman lenses." *IEEE Transactions on antennas and propagation* 39.4 (1991): 464-472.

[44] Moody, H. "The systematic design of the Butler matrix." *IEEE Transactions on Antennas*

and Propagation 12.6 (1964): 786-788.

[45] Belkin, Mikhail E., et al. "Design of reconfigurable multiple-beam array feed network based on millimeter-wave photonics beamformers." *Advances in Array Optimization*. InTechOpen, 2019.

[46] Butler, Jesse L. "Multiple beam antenna system employing multiple directional couplers in the leadin." U.S. Patent No. 3,255,450. 7 Jun. 1966.

[47] Huong, Nguyen Thanh. "Beamforming Phased Array Antenna toward Indoor Positioning Applications." *Advanced Radio Frequency Antennas for Modern Communication and Medical Systems*. IntechOpen, 2020.

[48] Uchendu, Iyemeh, and James R. Kelly. "Survey of beam steering techniques available for millimeter wave applications." *Progress In Electromagnetics Research* 68 (2016): 35-54.

[49] https://www.nicepng.com/ourpic/u2q8u2a9u2r5i1q8_digital-beamforming-icons-png-digital-beamforming/

[50] https://en.wikipedia.org/wiki/Luneburg_lens

[51] Ruze, John. "Wide-angle metal-plate optics." *Proceedings of the IRE* 38.1 (1950): 53-59.

[52] Rahimian, Ardavan. "Steerable Antennas for Automotive Communication Systems." *arXiv preprint arXiv:1404.1286* (2014).

[53] Kalam, Snehal Vijaykumar, and Anirudh Bhagwandas Rathi. "Optimum design of 4× 4 symmetrically structured Butler matrix." *International Journal of Scientific Research Engineering* (2016): 31-34.

[54] Shaikh, F. I., and Sanjay Bansidhar Akhade. "Smart antenna system using 4× 4 Butler matrix switched beam network for 2.4 GHz ISM band." *International Journal of Application or Innovation in Engineering & Management* 4.3 (2015): 278-282.

[55] Errifi, Hayat, et al. "DESIGN AND SIMULATION OF A PLANAR TOPOLOGY BUTLER MATRIX FOR 10 GHZ SWITCHED MULTIBEAM ANTENNA."

[56] Cummings, William C. *Multiple beamforming networks*. No. TN-1978-9. MASSACHUSETTS INST OF TECH LEXINGTON LINCOLN LAB, 1978.

[57] Barry, Joel, et al. "4X4 X-band butler matrices as antenna beamformers." *Multi-Disciplinary Senior Design Conference. Project No P09343*. 2009.

[58] Kim, Jin-Hyun, et al. "Design of phased array antenna for 5G mm-wave beamforming system." *2016 IEEE 5th Asia-Pacific Conference on Antennas and Propagation (APCAP)*. IEEE, 2016.

[59] Charczenko, Walter, et al. "Integrated optical Butler matrix for beam forming in phased-array antennas." *Optoelectronic Signal Processing for Phased-Array Antennas II*. Vol. 1217. International Society for Optics and Photonics, 1990.

[60] Hock, Goh Chin, et al. "Rapid and simple design approach of micro-strip Butler matrix beam-forming network for wireless system." *IEICE Electronics Express* 9.5 (2012): 346-351.

[61] Boumediene, Guenad, Meriah Sidi Mouhamed, and Fethi Tarik Bendimerad. "Study of a Planar Topology Butler Matrix for Printed Multibeam Antenna." *International Journal of Computer Science Issues (IJCSI)* 9.6 (2012): 122.

[62] Ibrahim, Asiti Zuraidah, and Mohamad Kamal A. Rahim. "Comparison between three radiation pattern using Butler matrix for beamforming network." *Jurnal Teknologi* 54.1 (2011): 25-43.

[63] Mosca, Stefano, et al. "A novel design method for Blass matrix beam-forming networks." *IEEE Transactions on Antennas and Propagation* 50.2 (2002): 225-232.

[64] Casini, Federico, et al. "A novel design method for Blass matrix beam-forming networks." *2007 European Microwave Conference*. IEEE, 2007.

[65] Attia, Hussein. "Artificial Magnetic Materials for High Gain Planar Antennas." (2011).

[66] Konstantinidis, Konstantinos. *Multi-layer periodic surfaces and metasurfaces for high-gain antennas*. Diss. University of Birmingham, 2015.

[67] Debogović, Tomislav. "Dynamic beamwidth control in partially reflective surface antennas." *Procedings of the 33rd ESA Antenna Workshop on Challenges for Space Antenna Systems*. 2011.

[68] Ju, Jeong Ho, et al. "Antenna having metamaterial superstrate and providing gain improvement and beamforming together." U.S. Patent No. 8,350,759. 8 Jan. 2013.

[69] Jackson, David, and N. Alexopoulos. "Gain enhancement methods for printed circuit antennas." *IEEE transactions on antennas and propagation* 33.9 (1985): 976-987.

[70] James, J. R., et al. "Leaky-wave multiple dichroic beamformers." *Electronics Letters* 25.18 (1989): 1209-1211.

[71] Abdulkareem, Sapna B., and Srivatsun Gopalakrishnan. "Development of Multilayer Partially Reflective Surfaces for Highly Directive Cavity Antennas: A Study." *Wireless Communications and Mobile Computing* 2020 (2020).

[72] Feresidis, Az P., and J. C. Vardaxoglou. "High gain planar antenna using optimised partially reflective surfaces." *IEE Proceedings-Microwaves, Antennas and Propagation* 148.6 (2001): 345-350.

[73] Feresidis, A., and J. C. Vardaxoglou. "Flat plate millimetre wave antenna based on partially reflective FSS." *2001 Eleventh International Conference on Antennas and Propagation, (IEE Conf. Publ. No. 480)*. Vol. 1. IET, 2001.

[74] Arora, Chirag, Shyam Sundar Pattnaik, and Rudra Narayan Baral. "SRR superstrate for gain and bandwidth enhancement of microstrip patch antenna array." *Progress In Electromagnetics Research* 76 (2017): 73-85.

[75] Khan, Mohammad Rezwan. *A beam steering technique using dielectric wedges*. Diss. University of London, 1995.

[76] Trentini, G. Von. "Partially reflecting sheet arrays." *IRE Transactions on antennas and propagation* 4.4 (1956): 666-671.

[77] P. Ghate and J. Bredow, "Beam Deflection using Non-Planar Broadside Coupled Split Ring Resonators," 2020 IEEE Asia-Pacific Microwave Conference (APMC), Hong Kong, Hong Kong, 2020, pp. 245-247, doi: 10.1109/APMC47863.2020.9331402.

[78] Afzal, Muhammad U., et al. "Beam-Scanning Antenna Based on Near-Electric Field Phase Transformation and Refraction of Electromagnetic Wave Through Dielectric Structures." *IEEE Access* 8 (2020): 199242-199253.

[79] https://www.ansys.com/products/electronics/ansys-hfss

BIOGRAPHICAL STATEMENT

Pratik Ghate received his Bachelor of Engineering degree majoring in Electronics Engineering from Nagpur University in 2014. He then completed Master of Science degree majoring in electrical engineering with research focused on computational electromagnetics with Dr. Raymond Rumpf from The University of Texas at El Paso in 2015. He then continued to work as a Graduate Teaching Assistant at The University of Texas at Arlington, pursuing a Ph.D. in the Radio Frequency Measurements Laboratory under the supervision of Dr. Jonathan Bredow. Pratik performed two graduate internships in Fall 2019 at Ansys Inc where he worked as an R&D Electronics simulation intern and in Summer 2020 at GlobalFoundries where he was employed as an RF Design Intern. His research interests include high frequency electromagnetics, RF design and measurements, Antenna design and computational electromagnetics.